INFORMATION TO USERS

This manuscript has been reproduced from the microfilm master. UMI films the text directly from the original or copy submitted. Thus, some thesis and dissertation copies are in typewriter face, while others may be from any type of computer printer.

The quality of this reproduction is dependent upon the quality of the copy submitted. Broken or indistinct print, colored or poor quality illustrations and photographs, print bleedthrough, substandard margins, and improper alignment can adversely affect reproduction.

In the unlikely event that the author did not send UMI a complete manuscript and there are missing pages, these will be noted. Also, if unauthorized copyright material had to be removed, a note will indicate the deletion.

Oversize materials (e.g., maps, drawings, charts) are reproduced by sectioning the original, beginning at the upper left-hand corner and continuing from left to right in equal sections with small overlaps.

Photographs included in the original manuscript have been reproduced xerographically in this copy. Higher quality 6" x 9" black and white photographic prints are available for any photographs or illustrations appearing in this copy for an additional charge. Contact UMI directly to order.

Bell & Howell Information and Learning
300 North Zeeb Road, Ann Arbor, MI 48106-1346 USA
800-521-0600

A

NMR and Dynamic Light Scattering Studies of Lipid Membrane Assemblies

By

Guohua Wu

A dissertation submitted to the Graduate Faculty in Chemistry in partial fulfillment of the requirements for the degree of Doctor of Philosophy, The City University of New York.

2000

UMI Number: 9969745

Bell & Howell Information and Learning Company
300 North Zeeb Road
P.O. Box 1346
Ann Arbor, MI 48106-1346

This manuscript has been read and accepted for the Graduate Faculty in Chemistry in satisfaction of the dissertation requirement for the degree of Doctor of Philosophy.

1/26/00
Date

Ruth E. Stark
Chair of Examining Committee

1/31/2000
Date

Executive Officer

Supervisory Committee

The City University of New York

Abstract

NMR and Dynamic Light Scattering Studies of Lipid Membrane Assemblies

by

Guohua Wu

Advisor: Professor Ruth E. Stark

The combination of nuclear magnetic resonance (NMR) and quasielastic light scattering (QLS) offers a potent experimental strategy to determine three-dimensional structures of mixed micellar aggregates. It has been used in the study of C_8-based model mixtures for fat digestion and C_{18} fatty acid transport mixtures. Using high-resolution solution NMR experiments (COSY, TOCSY, and HMQC), all of the ^1H resonances have been assigned in a model mixture. Then, intermolecular NOEs derived from 2D NOESY and ROESY spectra have revealed the molecular organization in mixed aggregates, and ^1H line broadenings observed upon addition of paramagnetic Mn^{2+} ion have shown the distribution of polar groups at the aggregate surface. In a complementary fashion, QLS has been used to analyze the size, size distribution, and possible shape of the aggregates. Together, the NMR and QLS results argue for a rodlike model of the fat digestive aggregates and a (preliminary) discoid model for fatty acid transport aggregates. These models should advance a molecular-level understanding of the processes of fat digestion and fatty acid transport, respectively.

QLS methods have been applied to deduce the 2.5-9 nm hydrodynamic radii and discoid shape for mixed phospholipid bicelles with a ratio of dimyristoylphosphatidycholine (DMPC) to dihexanoylphosphatidylcholine (DHPC) of 0.167-2.0. This determination provides the first direct physical evidence indicating the retention of a bilayer structure in isotropic bicelle solutions, which have been proposed as membrane-mimetic media for structural studies of peptides and proteins.

Finally, the chain order and conformation of several phospholipid/cholesterol aqueous dispersions have been evaluated using magic angle spinning (MAS) NMR spectroscopy. A series of MAS semi-solid NMR measurements, including ^{1}H sideband intensities, ^{13}C chemical shift changes, and 2D spin-echo variable-amplitude cross polarization (SEVACP) were made in order to compare different phospholipids (DMPC, bovine sphingomyelin (BSM), and synthetic SM) and the effects of cholesterol on these membranes. Several conclusions emerge consistently from these experiments: the DMPC membrane is more rigid and ordered than SM; the addition of CHL makes each of the membranes more ordered, but DMPC is more sensitive than SM and the saturated acyl chain of BSM is more sensitive than the unsaturated acyl chain; a possible hydrogen bonding system exists in pure BSM membranes, but it may be disrupted in the presence of CHL.

This thesis is dedicated to my wife and my son; without their love and understanding this never could have happened.

Also, this thesis is dedicated to be a memory of my grandfather; I will always remember his love and courage.

Acknowledgments

I would like to thank my wonderful advisor, Dr. Ruth E. Stark, for introducing me to the research fields of NMR spectroscopy and dynamic light scattering; teaching me so many things about the studies of model aggregates for late-stage fat digestion and fatty acid transportation, bilayer membranes, and phospholipid assembly; and giving me the opportunity to work in her laboratory for my Ph. D degree. I really appreciate her kind help during the writing of this thesis. It would be impossible for me to complete this thesis without her help and advice.

I would also like to thank Dr. Yang and Dr. Rosen for being on my committee and giving me a lot of valuable advice.

I would like to thank my granduncle, Mr. S. S. Wu, for his support, which help me to realize my dream. I would also like to thank my parents for their courage.

Lastly, I would like to thank all my fellow labmates and friends: Zhenjia, Cherryl, Anup, Feng, and Bin in Dr. Stark Lab at The College of Staten Island-CUNY.

Again, thank you very much to everyone.

Table of Contents

List of Abbreviations & Symbols

Å	angstrom
A	surface area
AFM	atomic force microscopy
AQ	acquisition time
B_o	external magnetic field strength
BS	bile salt
BSM	bovine brain sphingomyelin
C	concentration
C_8	digestive samples with acyl chains having 8 carbons
CHL	cholesterol
CMC	critical micelle concentration
COSY	2D correlation spectroscopy
CP	corss polarization
CPMAS-DD	cross polarization magic angle spinng-dipolar decoupling
CSA	chemical shift anisotropy
$C(s, t_d)$	autocorrelation function
D	diffusion coefficient
d (D)	diameter
DD	dipolar decoupling
DHPC	1,2-dihexanoyl-*sn*-glycero-3-phosphocholine
DMPC	1,2-dimyristoyl-*sn*-glycero-3-phosphocholine

DPC	dodecyl phosphocholine
DQF	double-quantum filter
ΔE	energy difference
FA	fatty acid
FID	free induction decay
FT	Fourier transform
^2H	deuterium
H_{CS}	magnetic shielding by surrounding electrons giving chemical shifts
H_D	direct dipolar-dipolar interaction
HMQC	heterounclear multiple quantum coherence
HQ	quadrupolar interaction for nuclei with spin > ½ only
H_{SC}	spin-spin coupling
H_Z	zeeman interaction with external magnetic field B_o
i	instantaneous scattered intensity
I	time-averaged scattered intensity
	Spin quantum number
J	spin-spin coupling constant (Hz)
k_B	Boltzmann constant
k	calibration constant
M	micellar mass
M_2	inter-pair second moment

MAS	magic angle spinning
MG	monoglyceride
MHz	megahertz
Mn^{2+}	manganeses ion
M_Z	z-averaged molecular weight
NMR	nuclear magnetic resonance
ms	time unit, 10^{-3} s
NOE	nuclear Overhauser effect
NOESY	2D nuclear Overhauser effect spectroscopy
OA	oleic acid
P	scattering form factor
P	incident laser power
PC	phosphatidylcholine
ppm	parts per million (unit of chemical shift)
q	DMPC/DHPC molar ratio
QLS	quasielastic light scattering
R	radius of DMPC domain
r	radius of DHPC rim
RAMP	ramp cross polarization
R_g	mean radius of gyration
R_h	hydrodynamic radius
ROE	rotating-frame NOE

ROESY	2D rotating-frame NOE spectroscopy
$S_{ch,inter}$	inter-proton pair order parameter
SDS	sodium dodecyl sulfate
SEVACP	solid echo & variable amplitude cross polarization
SM	sphingomyelin
SSM	synthetic sphingomyelin
SSB	spinning sideband
t	thickness of discoid
t_1, t_2	time dimensions (evolution, acquisition) in 2D NMR
T	temperature (K or °C)
T_m	melting temoerature
T_r	reduced temperature
T_1	spin-lattice relaxation time
T_2	spin-spin relaxation time
TC	taurocholate
WISE	wideline separation spectroscopy
t_d	delay time
TEM	transmission electron microscopy
TOCSY	2D total correlated spectroscopy
VACP	variable amplitude cross polarization
μ	magnetic moment
μs	time unit, 10^{-6} s

ν	frequency
$\Delta\nu_{1/2}$	half-linewidth at half-height
h	Planck's constant
η	viscosity of solvent (cP)
γ	magnetogyric ratio
τ_m (t_m)	mixing time
σ	shielding constant
δ	chemical shift (ppm)
ω	resonance angular frequency
ξ	QLS instrumental constant

List of Figures

List of Tables

Chapter I Introduction of nuclear magnetic resonance (NMR) spectroscopy

A Introduction

Since nuclear magnetic resonance (NMR) spectroscopy was first introduced in 1945, it has rapidly developed into a powerful modern experimental tool for chemists. Several key advances in NMR spectroscopy have already been honored by Nobel prizes, including the 1952 physics prize to E. M. Purcell and F. Bloch for their classic NMR experiment and the 1991 prize in chemistry to R. R. Ernst for his pioneering contributions in Fourier transform (FT) NMR and multidimensional NMR spectroscopy (Ernst, 1992). Now, not only physicists and chemists view NMR with great fascination. As a consequence of combined developments in high field NMR instrumentation, theory and experimental methods, and computer hardware and software, NMR spectroscopy has been widely applied in biology, geology, medicine, materials science, and pharmaceutics. In the context of this dissertation, NMR spectroscopy has proven to be a highly useful tool in the study of molecular structure and conformation of lipid aggregates and biological phospholipid membranes.

The theoretical foundation of nuclear magnetic resonance spectroscopy lies in the magnetic behavior of atomic nuclei. A correct description of these magnetic properties often requires the rules of quantum mechanics. Since a rigorous mathematical treatment is very complicated, it is preferable to use simple vector models for description. Furthermore, NMR spectroscopy covers so wide a range in both theory and

experiments that it is impossible herein to comprehensively discuss all of them. This introduction will be restricted mainly to the range of NMR experiments used in the current research projects.

B Basic concepts of nuclear magnetic resonance spectroscopy

B-1 Magnetic properties of nuclei, Larmor precession, and NMR signals (Gunther, 1995; Sanders and Hunter, 1994)

All NMR-active nuclei display a magnetic moment μ when they are placed in a magnetic field B_o. The main interactions associated with nuclei that have magnetic moments come from several sources (Fyfe, 1983): the Zeeman interaction (H_Z) from the external magnetic field B_o, dipole-dipole interactions (H_D) between nuclei, magnetic shielding (H_{CS}) by surrounding electrons, spin-spin (J) couplings (H_{SC}) between nuclei, and quadrupolar interactions (H_Q). Depending on the state of the NMR sample, a certain interaction could be either dominant or negligible. For example, the critical difference between solution NMR and solid as well as semi-solid liquid crystalline NMR is that the H_D and H_Q are averaged to zero by rapid molecular motion in solution state samples, while they will have significant effects in solid and semi-solid materials.

According to quantum theory, angular momentum and nuclear magnetic moments are quantized. The total number of possible energy levels is determined by the

spin quantum number I, as 2I+1. For example, a single proton has only two energy levels in a static magnetic field, a higher energy state and another lower energy state, because its spin quantum number is 1/2. When the direction of the external magnetic field B_o is taken to coincide with the Z-axis, the energy difference for two spin states of a proton as a function of the strength of the magnetic field is defined in Eq. I-1, where the μ_Z is the magnetic moment in the Z-axis.

$$\Delta E = 2\mu_Z B_o \qquad \text{(Eq. I-1)}$$

The lower energy state is preferentially occupied, with the proton distribution between the two energy states given by the Boltzmann distribution. To stimulate an energy jump from the lower level to the higher level, a certain frequency of radiation, defined by the Bohr frequency condition $\Delta E = h\nu$, is required to match the energy gap. Once some protons are excited by a short strong radio frequency (r.f.) pulse, the balanced Boltzmann distribution is disturbed. The disturbance cannot be maintained after the r.f. pulse is turned off, and the magnetization will return back to its Boltzmann distribution through a relaxation process. The relaxation process is very important in NMR since it reflects molecular motions and usually lasts sufficiently long to be measured (0.1-1.0 second in liquid).

After the magnetic moment is turned away from the Z-axis to the Y-axis by the r.f. pulse, it will behave like a gyroscope in a gravitational field, undergoing Larmor precession in the field B_o. The frequency of the precession is defined in Eq. I-2.

$$h\nu_o = 2\mu_Z B_o = \gamma h B_o/2\pi \qquad \text{(Eq. I-2)}$$

where ν_o is the Larmor precession frequency and γ is the magnetogyric ratio. The component of the precessional magnetization in the XY-plane, i.e. the NMR signal measured by a coil of wire perpendicular to the B_o field, decays with time as spin populations return to equilibrium (See also Section B-3). A schematic of the generation and detection of NMR signals is illustrated in Figure I-1.

B-2 Electron shielding and chemical shift

When an atom is placed in an applied magnetic field B_o, its electrons undergo a circular motion surrounding the nuclei. Based on Lenz' law, a new magnetic momentμ is produced with an opposite direction from B_o. The local magnetic field at the nucleus is generally (but not always) smaller than the applied field B_o by a fraction σ, as shown in Eq. I-3. Here the σ is defined as the shielding constant.

$$B_{\text{local field}} = B_o(1-\sigma) \qquad \text{(Eq. I-3)}$$

Fig. I-1: The generation of NMR signals in FT NMR spectroscopy (Gunther, 1995)

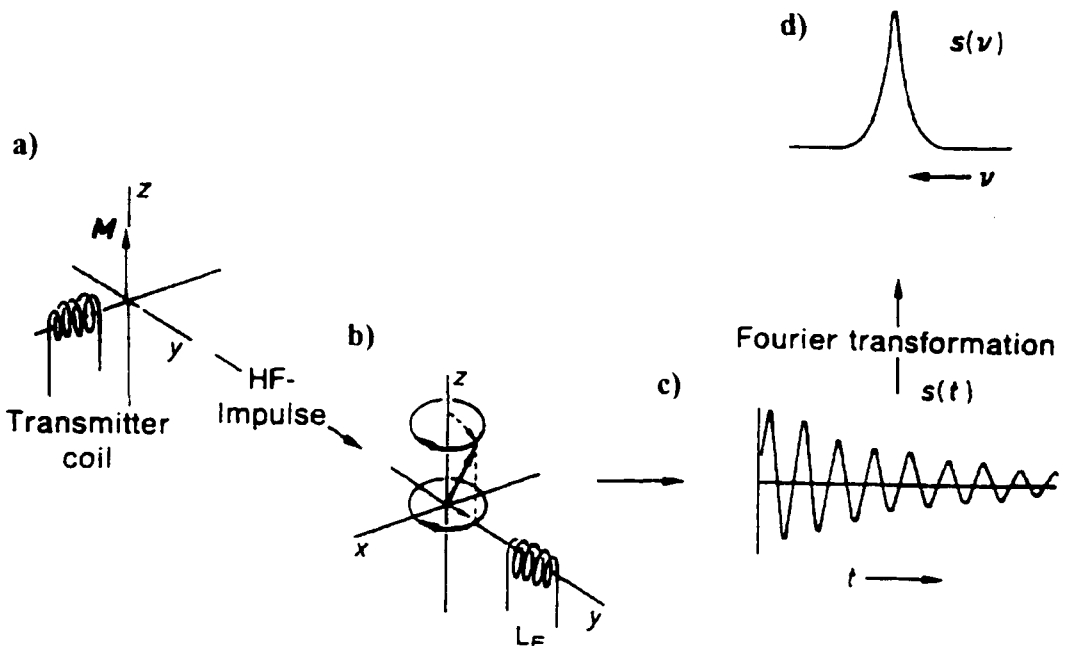

a) The vector of the macroscopic magnetization of the sample (M).

b) Individual nuclear magnetic moment μ_Z derivates during resonance from its position on the Z-axis through the combined action of the r.f. field and the magnetic field B_o.

c) The time signal in the detector coil fades away through relaxation.

d) Fourier transformation yields the frequency signal

The shielding constant σ is proportional to the electron density around the nuclei, which can be calculated for atoms by the Lamb formula (Gunther, 1995). However, the shielding constant becomes more complex for molecules because the electron density itself is a function of the distance from the nucleus and electrons circulating throughout the entire molecule.

Because the electron density around each nucleus in a molecule varies according to the types of nuclei and bonds in the molecule, the opposing induced field and therefore effective local field at each nucleus will vary, according to what is called the chemical shift phenomenon. In order to compare spectra acquired at different field strengths, the term chemical shift was developed and defined as the quotient of the difference of resonance frequency of the nucleus and a reference at the operating frequency of the spectrometer employed, in units of ppm (Eq. I-4).

$$\delta = (\nu_{substance} - \nu_{reference}) \times 10^6 / \nu_{reference} \qquad \text{(Eq. I-4)}$$

The difference in resonance frequencies is directly proportional to the strength of the external magnetic field, so that NMR spectra will typically be better resolved at higher field strengths. The range of chemical shifts varies with nuclear spin species: ~10 ppm for ^{1}H and ~250 ppm for ^{13}C.

The fact that the chemical shift comes from the effect of electron shielding also means that the chemical shift will be orientation-dependent when the electron distribution is not spherically symmetric. The difference in chemical shift associated with molecular orientation is known as chemical shift anisotropy (CSA). Although this factor averages to zero in solution NMR, it is one of main sources of line broadening in solid NMR, because molecular motion is restricted and the chemical shift is no longer averaged to its isotropic value. Differences in chemical shift may also originate from geometric isomers, as will be seen for solid and semi-solid phospholipid samples.

B-3 Free induction decay (FID) and Fourier transformation (FT)

The introduction of the Fourier transform method represented a revolutionary leap in NMR spectroscopy. It not only enhanced the sensitivity of high-resolution NMR, but it also opened the way for developing new experimental techniques, including multi-dimensional NMR. The basic behavior of nuclear precession can be illustrated in Fig. I-2.

Fig. I-2: Vector diagram of nuclear precession after an r.f. pulse (Benn and Gunther, 1983) (The X- and Y-axes rotate at the average Larmor frequency)

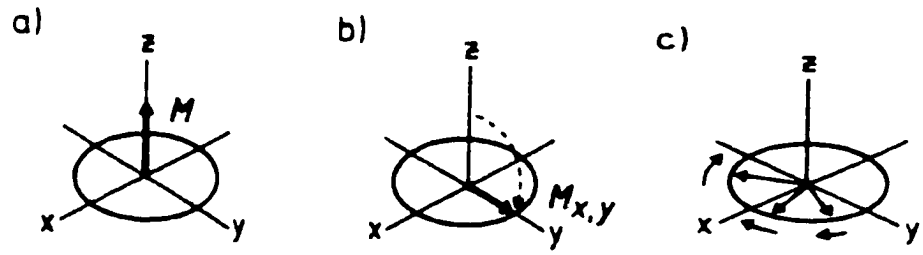

At equilibrium, nuclei with total magnetization M_o have a net orientation parallel to the field B_o (Fig. I-2a). The magnetization is flipped into the XY-plane by a radio frequency field (pulse) applied along the X-axis (Fig. I-2b). The Larmor frequencies of various nuclear moments are different due to the chemical shielding described in Section B-2 and due to B_o inhomogeneity; as a consequence, the vector M splits into various components (Fig. I-2c). The rotation of magnetic vectors produces time-dependent and detectable NMR transverse signals. Since energy is lost as a result of transverse relaxation, the signal undergoes a damped oscillation (free induction decay, FID). The transformation of the time-dependent FID into a frequency-dependent NMR spectrum is known as Fourier transformation (FT, Fig. I-1 c & d).

B-4 Spin-spin coupling (J coupling)

Spin-spin coupling (H_{SC}) refers to the magnetic interaction between individual spins through the intervening bonding electrons, so that the nuclear spins are indirectly connected. The H_{SC} interaction is field independent and is usually smaller than other forms of magnetic interactions. The magnitude of J coupling depends on the number and types of bonds through which the nuclei are coupled. Generally, geminal protons have a coupling about 12 Hz. But, the coupling between ^{13}C and protons can be as high as 150 Hz (Homans, 1992). For solid and semi-solid samples, J-couplings are much smaller than the dipole-dipole interaction. Well-resolved NMR spectra for solid and semi-solid samples can be obtained using the magic-angle spinning (MAS) technique.

An important method for detecting spin-spin coupling is the 2D homonuclear (^{1}H) chemical shift correlation spectroscopy (COSY, DQF-COSY) (Section B-6). The cross peaks in a 2D COSY spectrum correlate the chemical shifts of two protons and indicate the presence of scalar coupling between them. Because they usually have either a geminal or vicinal relationship, this experiment can lead to a direct assignment of adjacent protons in a proposed chemical structure.

B-5 Dipole-dipole coupling (Neuhaus and Williamson, 1989)

In contrast to the spin-spin coupling (H_{SC}), dipole-dipole coupling (H_D) involves magnetic interactions through space instead of through chemical bonds. Because H_D is proportional to the magnetogyric ratio and inversely proportional to the third power of the distance, it is dominant for ^{1}H, ^{19}F, and possibly ^{31}P, and it rapidly decreases in magnitude as the internuclear distance increases. Theoretical analysis shows that the dipole-dipole coupling has a dependence of $(3\cos^2\theta - 1)$ on the angle between the interunclear vector and the direction of the external field B_o.

In solution NMR, rapid Brownian motion of molecules reduces the dipole-dipole coupling to zero because the angle varies with time and the expression $(3\cos^2\theta - 1)$ vanishes. However, for solid and liquid crystalline materials, the dipole-dipole coupling between magnetic moments becomes a major interaction due to molecules being close in space and the absence of molecular motion. In fact, the dipole-dipole

interaction is not limited to isolated two-spin systems. The network of dipolar interactions becomes more complicated because any single proton has a large number of spin neighbors. In solid and semi-solid samples, these interactions can produce severe line broadening and compromise the usefulness of the resulting NMR spectra.

For solution NMR samples, spin pairs are often close to isolated, and their dipole-dipole interactions are measured through the nuclear Overhauser effect (NOE). In 2D NOESY and ROESY experiments, off-diagonal cross peaks are produced by relaxation effects through the transfer of magnetization via dipolar coupling when the distance between nuclei is less than 0.5 nm; their peak intensities contain information about the relative distances between the nuclei as long as indirect effects of other nearby spins (spin diffusion) may be neglected.

B-6 1D and 2D high-resolution NMR spectroscopy

One-dimensional (1D) pulse NMR experiments can be depicted in four time periods: preparation-evolution-optional mixing-acquisition. The receiver signal is solely a function of the detection time, which is Fourier transformed once into the 1D NMR spectrum.

If a 1D experiment is repeated many times and the evolution time is increased by a constant time Δt_1 in each measurement, the receiver signal will be a function of

both evolution time (t_1) and detection time (t_2). 2D NMR spectroscopy is always possible if using a systematic variation of the evolution results in a periodic change of a magnetic property of the spin system. Two time-dependent variables imply that data can be Fourier-transformed twice, so that two-dimensional FT-NMR spectroscopy is possible. The F1 dimension contains information according to the evolution range, while the F2 dimension contains information corresponding to the detection range. Even the simplest 2D ^1H-^1H chemical shift correlation (COSY), known as the Jeener experiment after its inventor, illustrates the revolutionary concept of 2D NMR (Figure I-3).

After the preparation period, the first 90° pulse produces transverse magnetization and the magnetization vectors precess in the XY-plane according to their characteristic Larmor frequencies and J-coupling constants. Then, the second 90° pulse produces different effects on non-coupled ($J_{ij}=0$) protons and scalar-coupled ($J_{ij}\neq0$) protons. For the former case, the second 90° pulse leads to a t_1-dependent modulation of the transverse magnetization that depends only on its own Larmor frequency, and is displayed on the diagonal line in a 2D COSY plot. For the latter case (for example, a pair of scalar-coupled protons i and j), the i magnetization depends on not only its characteristic Larmor frequency ω_i but also the characteristic Larmor frequency ω_j and vice versa, which results in off-diagonal cross peaks that indicate a scalar (J) coupling between i and j through chemical bonding. This discussion demonstrates that 2D NMR

Fig. I-3: Diagram of signal generation for 2D COSY spectrum

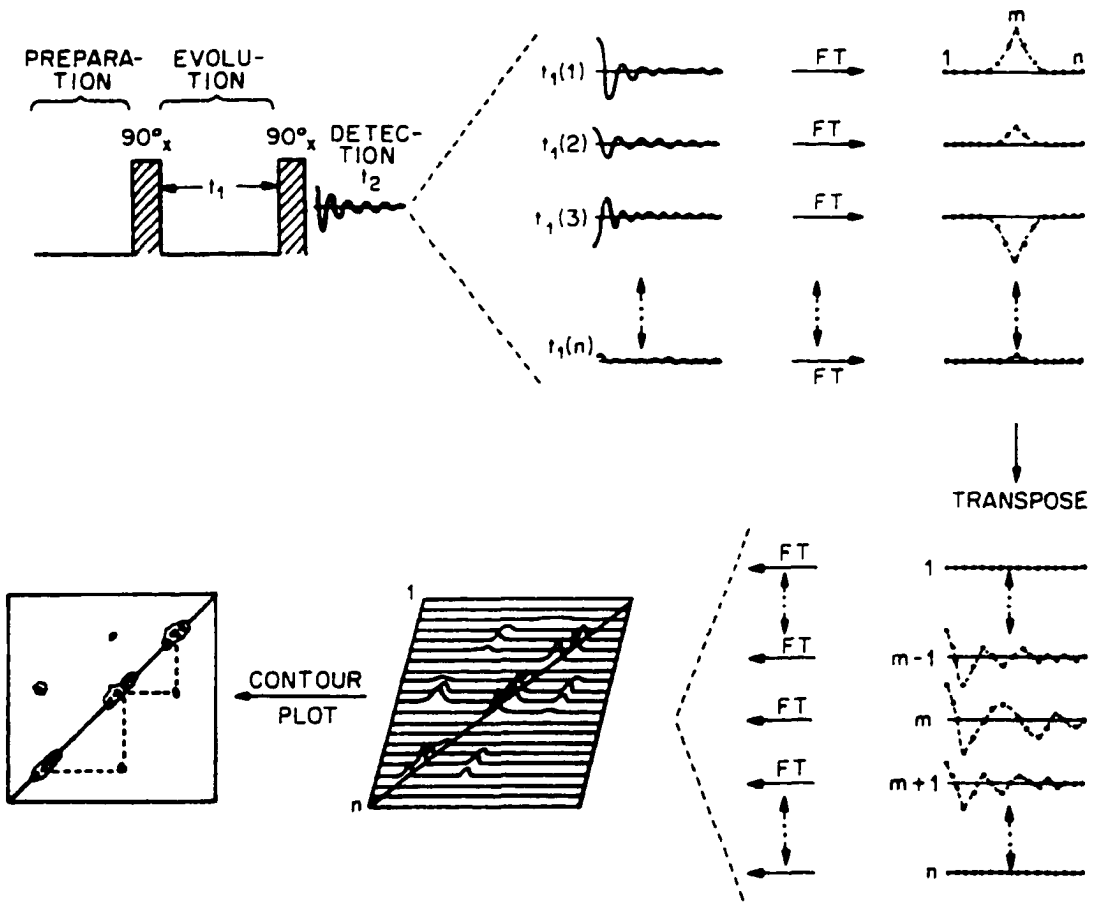

spectroscopy yields new structural information, in addition to an improvement in spectral resolution.

Principally, 2D NMR experiments can be separated to two classes: J-resolved and correlated 2D NMR experiments. The first type is characterized by one frequency (F1) for the coupling information and the other (F2) for chemical shifts (e.g. SEVACP in Section C-6). The second type is characterized by both frequencies (F1 and F2) indicating chemical shifts. The correlation between F1 and F2 is established through scalar coupling (COSY, Fig. I-3) or dipolar coupling (NOESY in Section C-2). The development of 2D NMR provides not only major improvements in spectral resolution, but it also reveals completely new properties of spin systems. There is no other development that has influenced NMR spectroscopy so profoundly in the last few decades as the idea of two-dimensional NMR.

B-7 Semi-solid NMR of lipid bilayer assemblies (Forbes and Oldfield, 1988)

Molecules are less mobile and more subject to angular restrictions in the solid and semi-solid state than in mobile liquids. Therefore, the dipole-dipole interaction (H_D) and quadrupolar interaction (H_Q) are potentially complicating factors that lead to severe line broadening in solid and semi-solid NMR spectra.

Because both dipolar coupling and chemical shift anisotropy (CSA) possess the same angular dependence in the form of $3\cos^2\theta - 1$, spinning a sample at the angle of 54.7°, called magic angle spinning (MAS), at a sufficient high rate will significantly narrow the NMR linewidth. To effectively narrow the NMR lines, the MAS spinning speed must be at least of the order of the CSA linewidth (a few kHz). However, dipolar coupling in solid and semi-solid samples often is too large to be eliminated using only MAS, so that homonuclear and heteronuclear dipolar decoupling techniques are necessary. Since the dipolar interaction may reach tens of kilohertz in solid NMR samples, the dipolar decoupling power must be as high as ~70 kHz.

Without MAS, the ^{1}H NMR spectrum of a semi-solid sample, such as a model biological membrane, is broadened by strong dipolar coupling. After application of MAS, the ^{1}H spectrum consists of narrow peaks, a resolved central band and a series of sidebands on both sides due to residual ^{1}H-^{1}H dipolar interactions (Fig. I-4). Because the intensity of the sidebands is a function of both spinning speed and proton dipolar coupling, the dependence of spinning sideband intensity on speed can be used to estimate the molecular order parameter.

Fig. I-4: Comparison of 300 MHz ^{1}H NMR spectra for semi-solid phospholipid (DMPC) without and with MAS at 25 ^{o}C

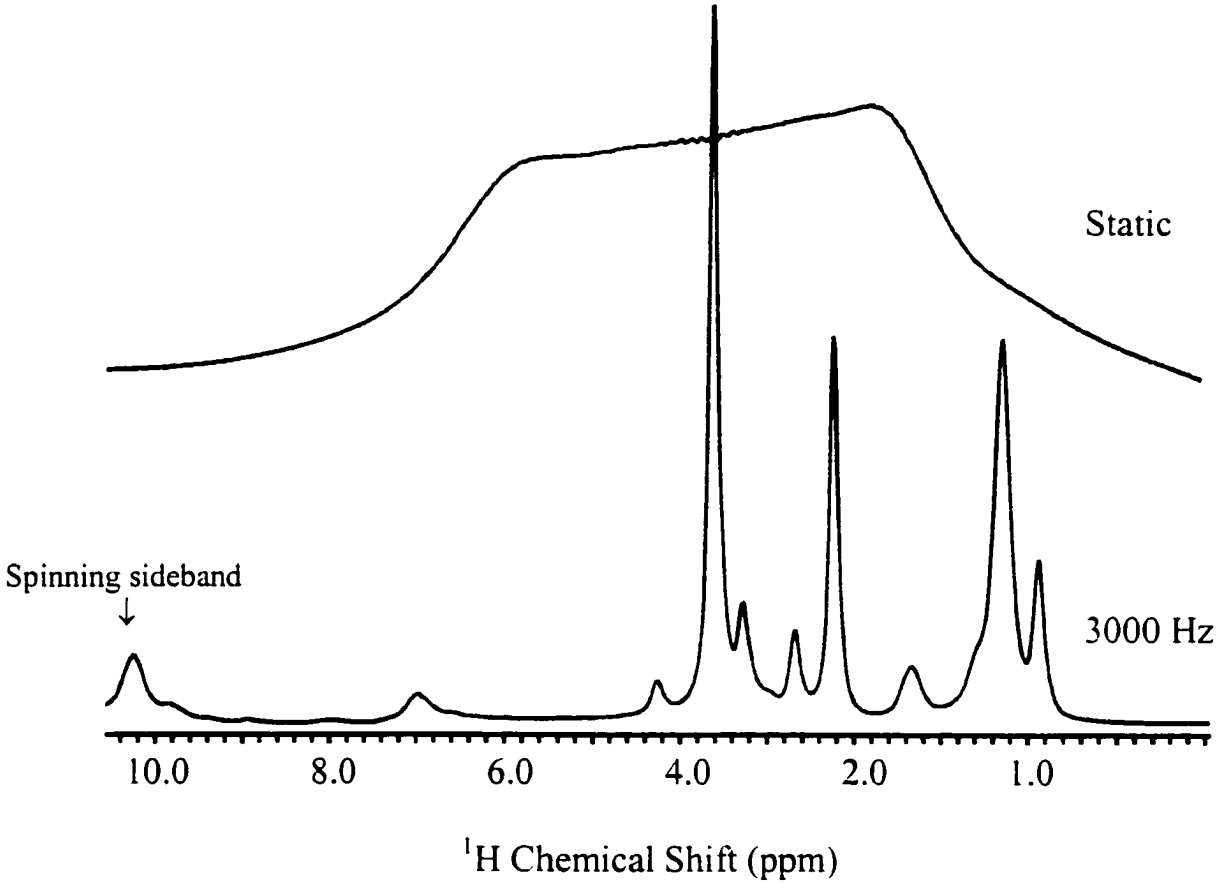

In addition to MAS and dipolar decoupling, the cross polarization technique is often required to obtain a high-resolution ^{13}C solid NMR spectrum, because both signal-to-noise ratio and natural abundance are unfavorable for ^{13}C nuclei. By using cross polarization, the magnetization of highly polarized ^{1}H nuclei can be transferred to unpolarized ^{13}C nuclei via the ^{1}H-^{13}C dipole-dipole interaction and the signal-to-noise ratio can be increased by up to a factor of four. Furthermore, the repetition rate after cross polarization is limited only by the spin-lattice relaxation time of ^{1}H, which is often much shorter than that of ^{13}C.

B-8 Spectral editing techniques: spin echoes and solid echoes

In practical NMR experiments, the inhomogeneity of the external magnetic field is an inevitable problem. After the Z-axis magnetization vector is rotated to the Y-axis by a 90° pulse, those nuclei with $B_{local} > B_o$ rotate faster and those with $B_{local} < B_o$ rotate slower than the average. As a consequence of the inhomogeneity of the field and different chemical shifts, the individual nuclear spins fan out in the XY-plane and the magnitude of the transverse magnetization decreases. If a 180° pulse is added in the middle of the evolution time at $t_1/2$, all vectors are turned around by the pulse and refocused again in a spin echo after another time $t_1/2$, as shown in Figure I-5. The resulting transverse magnetization can be detected without any effects from field inhomogeneity.

Fig. I-5: The pulse sequence and vector diagram for a spin echo

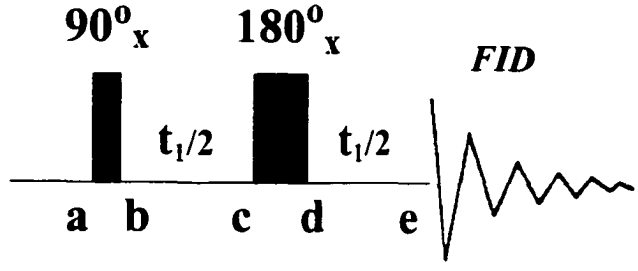

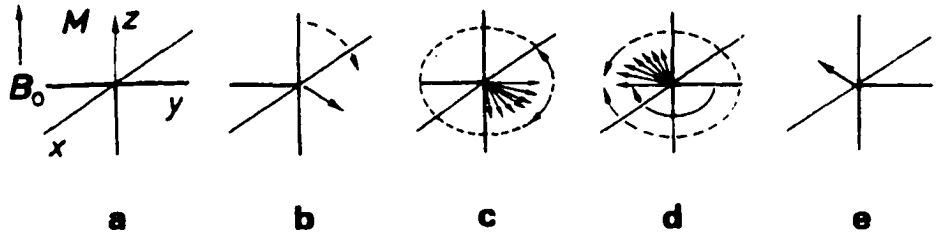

In wideline NMR, the line shape is of the utmost importance in measuring quadrupolar and dipolar interactions. To obtain an accurate representation of the line shape, most spectra are measured with an echo sequence, generally known as a solid echo or quadrupolar echo (Mansfield, 1964). The pulse sequence consists of two phase-shifted 90^{o} pulses, as diagrammed in Figure I-6. The times between the two 90^{o} pulses and from the second 90^{o} pulse to the acqusition must be short (~50 μs) and equal. Compared with the Hahn spin echo, the solid echo sequence uses a 90^{o}_{y} pulse for refocusing, since the traditional 180^{o}_{x} pulse would leave the Hamiltonian for homonuclear spin-bilinear interactions unchanged (Schmidt-Rohr and Spiess, 1994).

C NMR experiments used for structural studies of lipid multibilayer systems

C-1 2D double-quantum filtered COSY (DQF-COSY) and gradient DQF-COSY

COSY spectroscopy is perhaps the most widely used 2D NMR technique, because the cross peaks reveal scalar coupling via the spin connectivities. This property results in a direct assignment of adjacent protons and yields valuable molecular structural information. A brief introduction to 2D COSY spectroscopy was presented above (Section I B-6).

Fig. I-6: The pulse sequence for a solid echo measurement

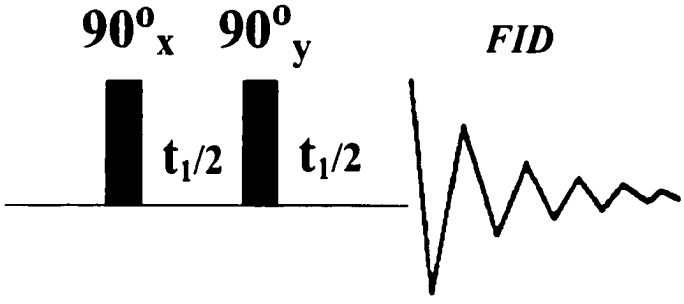

A disadvantage of the COSY experiment is that, as molecular size increases, ^1H chemical-shift correlation cross peaks become more crowded in the COSY contour diagram. Nuclei with similar chemical shifts will have cross peaks near the diagonal line and become more difficult to identify and be assigned. The double-quantum filtered COSY (DQF-COSY) experiment can be applied to deal with this situation (Figure I-7).

The introduction of the third 90^o pulse, with the help of a special phase cycle, allows the magnetization of spin-coupled nuclei to be detected, while the magnetization of singlet peaks is suppressed, because only two or more scalar coupled nuclei with different chemical shifts can undergo double quantum transitions. Although the DQF-COSY experiment has only half of the sensitivity of standard COSY, this sacrifice is often worthwhile because the spectral resolution of DQF-COSY is much better than that in the basic COSY spectrum. Another advantage of DQF-COSY is that it can suppress the water signal since water has no double quantum transitions.

A gradient field is also applied in the DQF-COSY pulse sequence for further suppression of artifactual signals and water, and to improve the signal/noise ratio (Braun et al., 1994). After a linear B_0 field gradient ΔG_z is applied along the Z-axis to the spins in the NMR tube, the Larmor frequencies of nuclei at different height vary by a small difference, similar to the consequence of field inhomogeneity. Because the gradient is quite short (~1 ms), the dephased signals can be recovered by a second field gradient with the same amplitude but opposite polarity, known as the gradient echo. The

Fig. I-7: The pulse sequence and phase table of the 2D DQF-COSY experiment

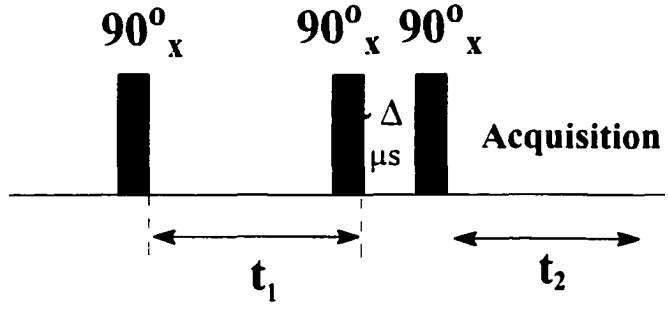

Exp.-No.	1	2	3	4	5	6	7	8
		a				b		
θ(P1)	0	1	2	3	2	3	0	1
θ(P2)	0	1	2	3	0	1	2	3
θ(P3)	0	0	0	0	0	0	0	0
θ(R)	0	2	0	2	2	0	2	0

fact makes it possible to select coherence pathways by combining r.f. pulses and pulsed field gradients in one pulse sequence, rather than the prior method of time-consuming phase cycling. Since the NMR receiver now detects only the required signals, the gain of the receiver can set much higher and the acquisition time is shortened significantly.

C-2 2D nuclear Overhauser spectroscopy: NOESY spectroscopy

As compared with the COSY experiment that relies on through-bond J coupling, the NOESY experiment takes advantage of the exchange of Z magnetization using through-space dipolar interactions as long as the nuclei are separated by less than 0.5 nm. The intensity of the cross peak reflects the relative distance between the spins that display the cross peak. Since there is an inverse sixth-power dependence of the pairwise dipolar interaction on the distance between the two coupled nuclei, the NOESY experiment has become indispensable for the conformational analysis of biomolecules. It should be noted that NOE and H_D show different distance dependences. The former is proportional to the cross-relaxation rate with an inverse sixth-power dependence on distance, and the latter arises from direct dipolar interactions with an inverse third-power dependence on distance. The pulse sequence of the 2D NOESY experiment is shown in Figure I-8.

Fig. I-8: The pulse sequence of 2D nuclear Overhause effect spectroscopy (NOESY)

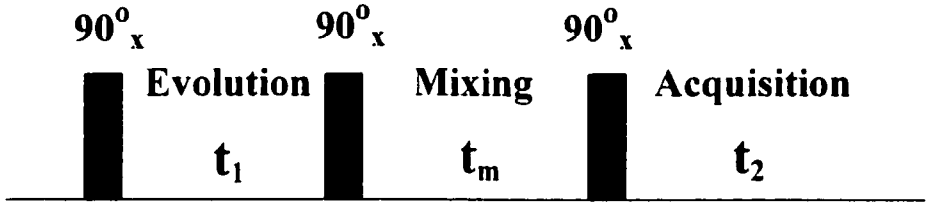

(50-500 ms)

After the preparation period, the first 90° pulse rotates the Z-magnetization of a pair coupled protons, i and j, into the XY-plane. After a particular evolution time $t_1=1/2\delta_{ij}$, where δ_{ij} is the chemical shift difference of i and j in Hz, an anti-phase magnetization accumulates between them. Then, the second 90° pulse produces a ± Z polarization. An exchange of magnetization (cross relaxation) proceeds during the mixing time period and gives rise to NOE cross peaks in the 2D spectrum. The third 90° pulse flips the Z-magnetization to the Y-axis where it can be observed and measured.

In practical applications of the NOESY experiment, several problems may complicate interpretation. Firstly, the NOE effect is a function of the product of resonance frequency and molecular correlation time. Thus, for molecular weights of a few thousand and high viscosity media, the NOE can be zero when $\omega\tau=1.12$. Secondly, spin diffusion effects may weaken the NOE signal of two dipolar-coupled spins or produce artifactual cross peaks between spins that are not close in space. Thirdly, the cross peaks due to chemical exchange will have the same sign as NOE cross peaks so they are not distinguished in the NOESY spectrum.

C-3 Hartmann-Hahn condition and spin locking: TOCSY spectroscopy

By adjusting r.f. field amplitudes (B_1) for ^1H and ^{13}C nuclei, the relationship $\gamma(^1H)B_1(^1H)=\gamma(^{13}C)B_1(^{13}C)$, called the Hartmann-Hahn condition, can be satisfied in a rotating coordinate system. Under this condition, energy can be exchanged by cross

polarization between the spin reservoirs. In practice, after the ^{1}H Z-magnetizations is flipped to the Y-axis by a 90^{o}_{x} pulse in the rotating frame, the magnetization can be locked along the Y-direction by a r.f. field, which is known as spin-locking. In heteronuclear NMR, once the Hartmann-Hahn condition is set, the ^{1}H and ^{13}C magnetizations oscillate with the same Larmor frequency and the energy transfer from the high natural abundance ^{1}H to the low natural abundance ^{13}C can be completed. The Hartmann-Hahn experiment (i.e. cross polarization, CP) has great application in solid-state NMR spectroscopy (Sanders and Hunter, 1994).

For homonuclear NMR in solution, the total correlation spectroscopy (TOCSY) experiment is a typical example in which the magnetization transfer is based on scalar spin-spin coupling. Because magnetizations are locked on the Y-axis, the transfer can proceed beyond directly coupled nuclei and pass through a more extensive scalar-coupled network of a molecular chain. The pulse sequence of the TOCSY experiment is illustrated in Figure I-9. Since TOCSY can reveal longer-range coupling than COSY, the TOCSY spectrum supplies some structural information that cannot be seen in a COSY spectrum. Moreover, the comparison of NOESY and TOCSY spectra helps to distinguish inter-molecular and intra-molecular NOE cross peaks.

Fig. I-9: The pulse sequence of 2D TOCSY spectroscopy (Gunther, 1995)

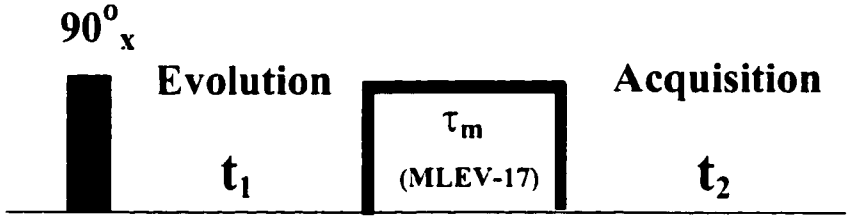

The spin-lock of magnetization along the Y-axis is obtained by using a specialized sequence such as MLEV-17. The MLEV-17 consists of the original MLEV-16 (16 pulse cycles about ± x axis), followed by a regular uncompensated 180°_{x} pulse. The final 180°_{x} pulse very efficiently removes overall imperfections that occurred in the prior MLEV-16 sequence (Bax and Davis, 1985, a). The spin-lock time is generally set to a few tens of milliseconds and the effective spin-lock strength is <10 kHz. Depending on the range of detection, the spin-lock time can be further increased (for long-range couplings) or decreased (for short-range couplings).

C-4 Rotating-frame analog of NOESY: ROESY spectroscopy

NOESY has an inherent disadvantage: the sign of the NOE changes as a function of the product of resonance frequency and correlation time, and thus medium-size molecules suffer from nulling effects. However, when the NOESY experiment is carried out in the rotating frame with a spin-lock pulse, the cross-relaxation process (ROE) involves $T_{1\rho}$ instead of T_1. The ROE will always be positive for freely tumbling molecules up to MW≈10^6 (Croasmun and Carlson, 1994). This improved technique is known as Rotating Frame Overhauser Enhancement Spectroscopy (ROESY) (Bax and Davis, 1985, b). Because the ROESY experiment always has a positive NOE, it solves the two major problems with NOESY: there is no nulling condition and chemical exchange peaks can be distinguished from NOE peaks by sign. The ROESY method is particularly suitable for the study of macromolecules near the condition $\omega\tau \approx 1$,

especially biological samples. Generally, the choice of NOESY or ROESY is based on the practical problem under study.

The pulse sequence of ROESY is basically identical to the pulse sequence of TOCSY (Fig. I-9), but a longer spin-lock duration (a few hundred milliseconds) is required to ensure that magnetization transfer proceeds via dipole-dipole interactions rather than scalar coupling. The spin-lock in ROESY can be maintained using either a constant phase or a series of nonselective pulses of small flip angle and duration spaced by short intervals (Bax, 1988). Although the first method uses a lower spin-lock field strength (<10 kHz), spurious cross peaks can occur in the experiment if the effective field strengths experienced by two coupled spins are of nearly identical magnitude (Bax and Davis, 1985, a). The second method makes it is possible to improve spectral quality by phase-combination of a series of pulses. However, since there are many short intervals (windows) in spin-lock pulses, the spin-lock field strength has to be higher (10-20 kHz) to achieve the same effectiveness as the first method.

Since a spin-lock is used in both ROESY and TOCSY experiments, a disadvantage of the ROESY is that TOCSY-like cross peaks also appear via J-coupling pathways. This problem can be greatly diminished by using a special multiple-pulse spin-lock sequence, known as T-ROESY (Hwang and Shaka, 1992).

C-5 Semi-solid NMR spectroscopy: ^{1}H MAS sideband intensities and ^{13}C CPMAS-DD spectra

As noted in Section B-7, the NMR spectrum of a solid or semi-solid sample typically consists of broad lines because of residual dipolar-dipolar coupling and chemical shift anisotropy (CSA). Since both dipolar interactions and CSA have an angular dependence with form $3\cos^2\theta_{ij} - 1$, the magic angle spinning technique may be used to obtain a high-resolution solid-state ^{1}H NMR spectrum. With MAS at 1000-3000 Hz, resonances for lipid semi-solid samples can be as narrow as 10~20 Hz, yielding a chemical shift-separated central spectrum and several small sidebands on each side, depending on the strength of the ^{1}H-^{1}H dipolar interaction and the spinning speed. The intensities of the sidebands provide a semi-quantitative description of molecular order behavior. With line narrowing produced by MAS, 2D experiments such as COSY, TOCSY, and NOESY also become feasible in lipid multibilayer systems.

For nuclei with low magnetogyric ratio and long spin-lattice relaxation times, additional cross polarization (CP) and dipolar decoupling (DD) techniques are often required (CPMAS-DD) to generate a high-resolution spectrum (Sanders and Hunter, 1994). A typical 1D ^{13}C CPMAS-DD pulse sequence is shown in Figure I-10.

Fig. I-10: The pulse sequence of a 1D ^{13}C CPMAS-DD experiment

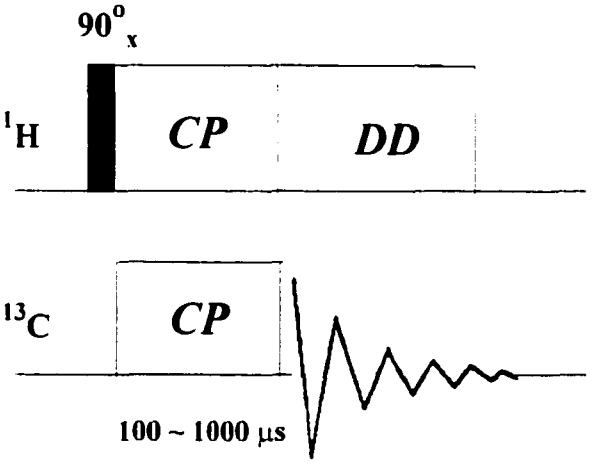

The ^{1}H-^{13}C cross polarization condition is achieved by adjusting the amplitudes of spin-lock pulses so that a Hartmann-Hahn condition ($\gamma(^{1}H)B_1(^{1}H)=\gamma(^{13}C)B_1(^{13}C)$) is produced with a CP matching width of a few tens of kHz. Since ^{1}H and ^{13}C nuclei precess at equal frequencies about their respective r.f. fields, an efficient magnetization transfer between nuclei with different Larmor frequencies becomes allowed. However, this smooth profile of frequencies will break down once the MAS spinning speed is comparable to the ^{1}H-^{1}H or ^{1}H-^{13}C dipolar interactions. The cross polarization matching changes qualitatively from a smooth curve to a saw-tooth curve, because dipolar fluctuations no longer compensate for the energy mismatches of the two spin-lock fields (Peersen and Smith, 1993). As a consequence, finding a cross polarization condition which simultaneously fits all magnetic spin environments is often extremely difficult and the CP signal becomes very sensitive to spinning speed, amplifier draft, and probe tuning. The problem becomes more serious for dilute semi-solid lipid samples, because MAS spinning attenuates the partially averaged proton dipolar couplings found in these samples. New variable-amplitude cross-polarization (VACP) (Peersen and Smith, 1993) and ramped-amplitude cross polarization (RAMP-CP) methods (Metz et al., 1994) are used to overcome the problem. They supply a more even sampling all of the magnetic spins regardless of their differences since an up-and-down variation in CP power in VACP or a linearly increasing CP power in RAMP are used for cross polarization. The VACP protocol was used in both ^{13}C MAS and the following SEVACP experiments.

C-6 ^{1}H solid echo wideline & ^{13}C VACP experiment (SEVACP)

Order parameters of lipid molecules yield important information on the organization of biological membranes, since they reflect the packing order of hydrocarbon chain segments in a multibilayer. They have been studied extensively using ^{2}H NMR spectroscopy (Smith and Oldfield, 1984). However, ^{2}H NMR requires selective deuteration of lipid molecules for isotopic enrichment. It is often difficult and expensive, limiting the practical application of ^{2}H NMR. There is significant interest in developing new techniques to obtain similar information directly from the natural-abundance NMR spectrum.

The SEVACP experiment (Urbina and Oldfield, 1998) is a simple 2D NMR experiment measures inter-pair proton order parameters as well as spin diffusion from broad ^{1}H spectral patterns that are separated along the ^{13}C NMR chemical shift dimension. For lipids with loosely coupled proton pairs, in which the intra-pair dipolar interaction (protons on the same carbon) is assumed to be considerably larger than corresponding inter-pair counterpart (protons on different carbons), this experiment reflects the order of adjacent chain segments and thus lipid bilayer organization. The methylene chains and headgroups of phospholipids in bilayer membranes are known as a loosely-coupled system, since rapid flexing and twisting motions of these domains reduces the inter-pair dipolar interaction but leaves the intra-pair dipolar interactions intact.

The SEVACP pulse sequence consists of two parts (Fig. I-11). First, two phase-shifted 90° pulses comprise a standard solid echo that yields an accurate representation of the wideline ^{1}H shape. Second, the ^{1}H magnetization is continuously transferred to directly coupled carbon nuclei by variable-amplitude cross polarization (VACP). Thus, the ^{1}H spectra are separated according to the high-resolution ^{13}C chemical shifts of their covalently attached carbons. The inter-pair order parameter $S_{ch(inter)}$ for each methylene carbon position may be calculated from the ^{1}H linewidths measured in a SEVACP spectrum, provided that the corresponding ^{13}C resonances are well resolved. The procedure for order parameter calculation will be detailed in Chapter V. Because sufficient contact time is required at each amplitude step in the up-down VACP sequence, the total contact time used in VACP is longer than standard CP. If a mixing time is introduced between the solid echo and the VACP, all ^{1}H linewidths are reduced to the values corresponding to more mobile methylene segments, as a consequence of spin diffusion with the phospholipid acyl chains.

Fig. I-11: The pulse sequence for a SEVACP 2D NMR experiment (Urbina and Oldfield, 1998)

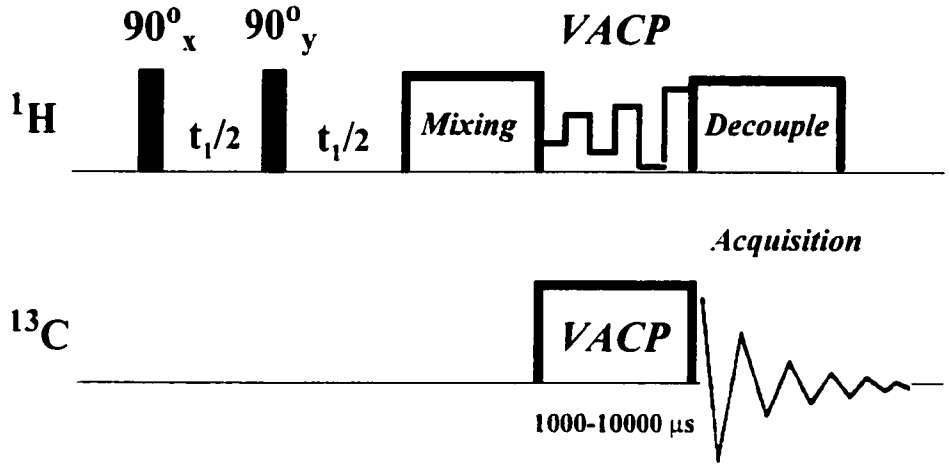

Chapter II Introduction to Quasi-elastic Light Scattering (QLS)

A Introduction and Methodology

A-1 Basic theory of dynamic laser light scattering (QLS)

Laser light scattering measurements can be classified into two major types, static and dynamic light scattering, depending on how the scattered intensity is measured (Chu, 1991). In classical static light scattering, the time-averaged total intensity is measured as a function of scattering angle. The technique has been widely used to construct Zimm plots, from which the z-average molecular weight, the second Virial coefficient, and the radius of gyration (R_g) of the scattering particles (macromolecules, micelles, or molecular aggregates) can be revealed. When the size of the scatterer is sufficiently large to show a measurable angular dependence on scattered intensity, it is possible to probe the shape of the scatterer.

In fact, the scattered intensity is not only a function of scattering angle; it is a fluctuating function of time, too. When a focused laser beam passes through a dilute suspension of scatterers, the light is scattered from each particle. The individual scattered light waves mutually combine, or interfere, to produce a net scattering intensity measured by a photomultiplier tube detector. The instantaneous intensity $i(s,0)$ always fluctuates around an average scattered intensity, because the suspended scatterers undergo constant random Brownian motion. The time-averaged intensity $\bar{i}(s)$ is defined by the following equation (Hiemenz and Rajagopalan, 1997):

$$\bar{I}(s) = \lim_{t_n \to \infty} \frac{1}{t_n} \int_0^{t_n} i(s,t)\,dt = \lim_{n \to \infty} \frac{1}{n} \sum_{j=1}^{n} i(s,j\Delta t) \qquad \text{(Eq. II-1)}$$

Where t_n is the duration time of the measurement, n is the number of small discrete time ranges Δt ($t_n = n \times \Delta t$), and j is value of n. The limits $t_n \rightarrow \infty$ and $n \rightarrow \infty$ in Eq. II-1 indicate that QLS measurements should be made over a sufficiently long time for the time-averaged intensity to be accurate.

The fluctuation of the instantaneous scattered intensity contains information on particle diffusion, which is the basis of a dynamic light scattering measurement. This method is also referred to as quasielastic light scattering (QLS), because the laser light scattering involves almost no loss of energy (Cohen et al., 1990). In modern dynamic light scattering, the temporal variation of the scattered intensity is recorded and represented through an autocorrelation function that is defined as follows (Hiemenz and Rajagopalan, 1997):

$$C(s,t_d) = \lim_{t_n \to \infty} \frac{1}{t_n} \int_0^{t_n} i(s,t)i(s,t+t_d)dt = \overline{i(s,0)i(s,t_d)}$$
$$= \lim_{n \to \infty} \frac{1}{n} \sum_{k=0}^{n} i(s,k\Delta t)i(s,(k+j)\Delta t) \qquad \text{(Eq. II-2)}$$

where the time t_d is known as the delay time between two intensity measurements, which represents the delay in time between two signals, and k is another constant variable similar to j in Eq. II-1. The autocorrelation function has its maximum value $[i(s,0)]^2$ at $t_d = 0$; it approaches a constant $[i(s)]^2$ as $t_d \rightarrow \infty$ and decays (becomes uncorrelated) with increasing delay time. These situations are described schematically in Figures II-1 and II-2 (Hiemenz and Rajagopalan, 1997).

The ratio of the autocorrelation function to its asymptotic value $[i(s)]^2$ can be written as

$$\frac{C(s,t_d)}{[\bar{i}(s)]^2} = g_2(s,t_d) = 1 + \xi|g_1(s,t_d)|^2 \qquad \text{(Eq. II-3)}$$

Eq. II-3 is known as the Siegert relation in mathematics, in which ξ is an instrumental constant approximately equal to unity. The Siegert relation is valid except in the case of samples with a very small number of scatterers or when the Brownian motion of the scatterers is limited. Subsequent analysis of QLS data is simply associated with the interpretation of the $g_1(s,t_d)$ function in terms of the size of the scatterers.

Figure II-1: Fluctuation of instantaneous scattered intensity with measurement time

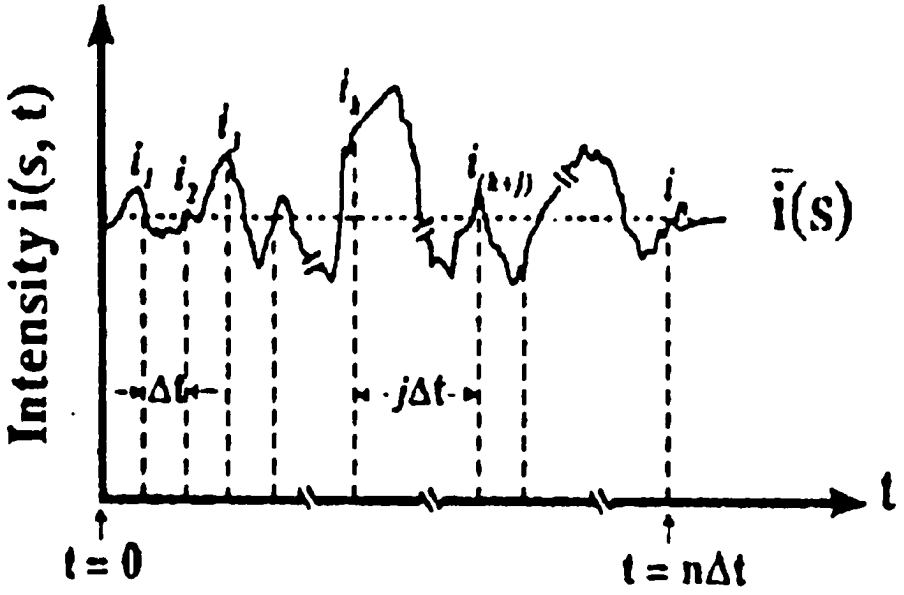

Figure II-2: Decay of the autocorrelation function with delay time t_d

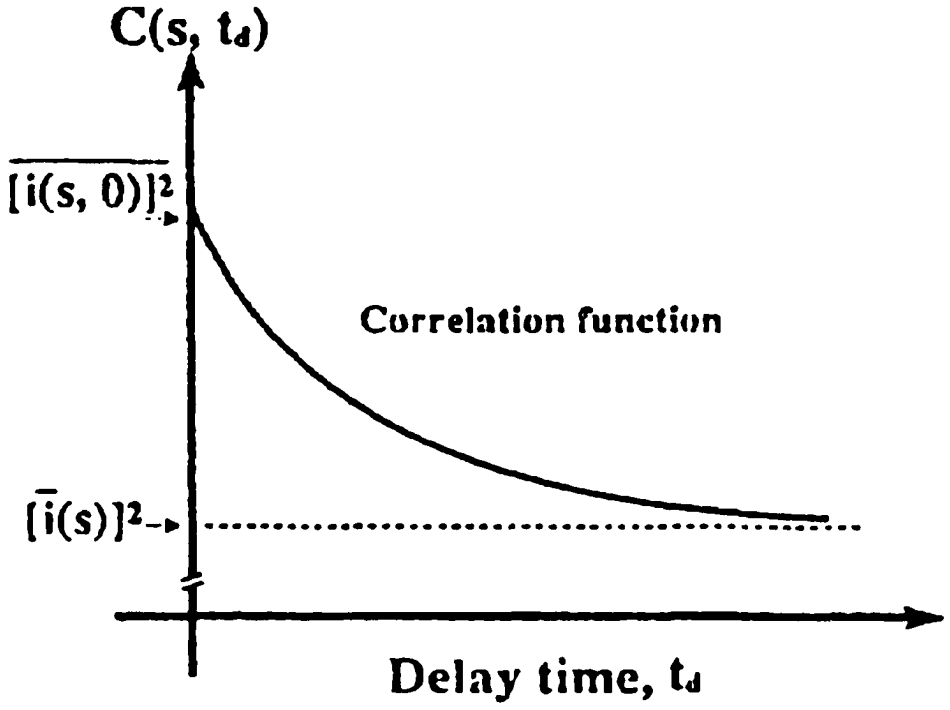

A-2 Size and size distribution of scattered particles

The most common application of QLS is in size determination. When QLS is applied to dilute, monodisperse solutions, it can measure the average hydrodynamic radius R_h of scatterers in the solution. Even if the scatterers comprise a polydisperse system, QLS can successfully estimate the size and the size distribution of these scatterers, which may be difficult to obtain by other conventional techniques, such as static light scattering (SLS) and gel permeation chromatography (GPC, also called size exclusion chromatography, SEC).

For a monodisperse distribution of spherical particles, the $g_1(s,t_d)$ term of the Siegert relation decays exponentially as

$$g_1(s,t_d) = \exp(-s^2 D t_d) \qquad \text{(Eq. II-4)}$$

Here D is the diffusion coefficient of the scatterers and s is the magnitude of the scattering vector. Furthermore, the hydrodynamic radius of the scatterers can be calculated by the Stokes-Einstein equation from the diffusion coefficient D:

$$D = \frac{k_B T}{6\pi\eta R_h} \qquad \text{(Eq. II-5)}$$

where η is the viscosity of the solvent, k_B is the Boltzmann constant, and T is the absolute temperature of the sample solution.

When the particle size has a polydisperse distribution, the situation becomes much more complicated because the overall decay of the function $g_1(s, t_d)$ is a weighted average of contributions from each particle defined by the weight-distribution function $w_j(s^2, D_j)$. Thus,

$$g_1(s,t_d) = \lim_{n\to\infty} \frac{1}{n} \sum_{j=1}^{n} w_j(s^2 D_j) \exp(-s^2 D_j t_d) \qquad \text{(Eq. II-6)}$$

Several mathematical methods are available to analyze the size information from the experimentally obtained $g_1(s, t_d)$ function. The n^{th} Cumulant expansions provide the simplest method as shown in Equation II-7 (Hiemenz and Rajagopalan, 1997):

$$\begin{aligned} \ln g_1(s,t_d) &= \sum_{n=1}^{\infty} k_n(s) \frac{(-t_d)^n}{n!} \quad \text{in the limit } \tau_d \to 0 \\ &= -\bar{D} s^2 t_d + \sigma^2 s^4 \frac{t_d^2}{2!} + \text{higher order terms} \end{aligned} \qquad \text{(Eq. II-7)}$$

As long as the size distribution is sufficiently narrow ($M_z/M_w < 1.25$), the Cumulant method can analyze the results quickly and accurately (Brown and Pussy, 1975). However, since the linear relationship between $\ln g_1(s, t_d)/s^2 t_d$ and $s^2 t_d$ (Eq. II-7) is satisfied only for small variations in t_d. Cumulants are only suited to deal with the QLS data obtained from a narrow monodisperse sample. When scatterers have broad monodisperse or two-size distributions, corresponding to a large range of delay times, the Cumulants method becomes problematic since the Cumulant expansion may diverge or converge too slowly (Provencher, 1979).

To solve the problem caused by two-size distributions, a new double-exponential function has been used to represent $g_1(s,t_d)$ (Chu, 1991):

$$g_1(s,t_d) = A_1\exp(-s^2Dt_d) + A_2\exp(-s^2Dt_d) \qquad \text{(Eq. II-8)}$$

where $A_1+A_2=1$. Since two exponential functions are introduced, the new method, known as DBLEXP, shows advantages in QLS data analysis for two-size distribution samples. It also can fit over a broader range of t_d than Cumulants (about 1.5 times quantitatively). However, its success is limited; its methodology is the same as the Cumulants, so that the delay time t_d has to be sufficiently small (in other words, the size distribution should be sufficiently narrow too).

A more straightforward approach to the problem of polydispersity is through Laplace inversion. In mathematics, Eq. II-6 can be re-written in an integral form. Solving for the weight-distribution function $w_i(s^2D_i)$ based on an experimentally obtained $g_1(s, t_d)$ using an integral equation is known as Laplace inversion (Chu, 1991). In other words, using the $g_1(s, t_d)$ information obtained from a QLS measurement directly yields the value of diffusion coefficient D. Unfortunately, the accuracy of this method is extremely sensitive to noise in the original autocorrelation function.

In the past a few decades, computational advances have led to the development of nonlinear least-squares fitting programs. Two Laplace-inversion methods, non-

negatively constrained least squares: multiple pass (NNLS) and regularized (CONTIN), are installed in the BI-9000AT QLS instrument. Both NNLS and CONTIN can analyze the size and size distribution of polydisperse aggregates. In practice, CONTIN is more suitable for the case in which two size fractions are widely separated, while NNLS often loses some information. On the other hand, NNLS is less affected by dust because it ignores such abnormal signals. As long as the size distribution is demonstrated to be narrow and monodisperse, Cumulants is the preferred method. Because each available data analysis method has specific limitations, none of them completely satisfies all the requirements of size distribution analysis. Often, the results of QLS analysis are best interpreted as semiquantitative values.

A-3 Shape deduction from the dependence of scattered intensity on particle size

Although the dominant practical application of QLS is in size measurement, another important capability of QLS is deducing the shape of a molecular aggregate. For instance, when suspended lipid micelles are monodisperse and noninteracting, the time-averaged scattered intensity is given as follows (Mazer et al., 1980):

$$\bar{i}(s) = ACMP \qquad \text{(Eq. II-9)}$$

Here A is a calibration constant, C is the concentration (w/v) of micellar aggregates, M is the micellar weight, and P is the scattering form factor which describes the angular anisotropy of the scattered light. If we neglect very weak effects of temperature, lipid

concentration, and lipid/surfactant ratio on the value of A, the quantity $i(s)/C$ is proportional to the product MP. For a given R_h, the corresponding factor MP will have different values depending on the shape of the micellar scatterers. For this reason, the shape of a micellar aggregate can be experimentally deduced by analyzing the dependence of $i(s)/C$ (i.e. MP) on hydrodynamic radius R_h, which can be varied in turn by changing the temperature, total lipid concentration, or lipid component molar ratio.

Many aggregates of analytical interest do not really have a spherical shape. Generally, four shape models, oblate ellipsoid, prolate ellipsoid, disk, and cylinder-like rod, are considered. The equations for converting the hydrodynamic radius measured by QLS and assuming a sphere to the corresponding dimensions of a disk or rod can be deduced from the following formula

$$R_h^{-1} = (2/3)V^{-1}\int_V (r)^{-1} dV \qquad \text{(Eq. II-10)}$$

Here r represents the distance from the geometric center of the particle to the volume element dV, and V is the total volume of the particle. The models and corresponding equations for the disk and cylinder-like rod are shown in Appendix A (Mazer et al., 1980).

For the purpose of deducing the shape of a micellar aggregate, theoretical curves of the dependence of MP ($i(s)/C$) on R_h are calculated and plotted assuming

curve with these theoretical curves, it is possible to determine the micellar shape. As noted above, this methodology is applicable only to solutions that contain monodisperse, noninteracting particles.

B QLS Measurements

B-1 QLS apparatus and parameter settings

The QLS apparatus consists of a LEXEL Model 75 (200mW) argon ion laser (Palo Alto, CA), a Brookhaven BI9000AT autocorrelator (Brookhaven, NY), and a NESLAB Model RTE-100 compact bath/circulator (Portsmouth, NH). The wavelengths of laser output can be set at 488 nm, 514 nm, or 615 nm; our measurements used 488 nm or 514 nm. The autocorrelator is equipped with a maximum of 522 time channels. The QLS instrumental system is shown in Figure II-3.

Fig. II-3. BI-9000AT QLS instrumental system

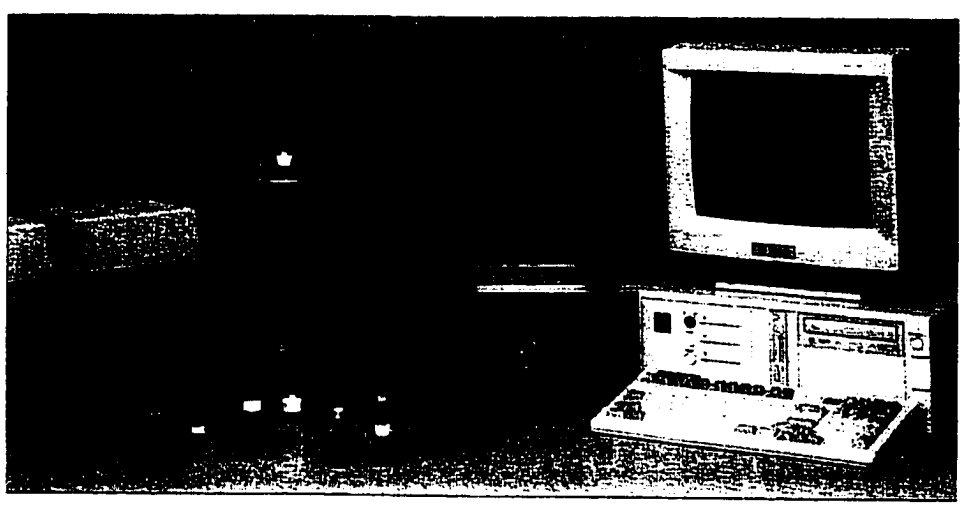

Aqueous QLS samples are normally prepared by dissolving the compound of interest in clean deionized water, which is filtered twice with 0.2 μ filters (first a hollow fiber filter and then a pump filter) and referred to henceforth as best water. A minimum sample volume of 1 ml is placed in a quartz cell. For the purpose of removing dust, filtration of the sample solution with a pump filter (0.2 μ) may be necessary. Since filtration may alter the concentration of sample solution or even remove molecular aggregates, it is not recommended, especially when mixed aggregates are present. In fact, filtration was used only in QLS measurements of polystyrene size standards, bile salts (TC), and buffer solutions.

The QLS measurements were generally performed under the following conditions: scattering angle $\theta = 90^{o}$, laser input power $P \approx 50$ mW, pinhole size = 200 μm, duration time ≈ 300 seconds, first delay time = 1/10 the smallest size obtained, last delay time = 10 times the largest size obtained. The viscosity of water at the temperature of the QLS measurement (5-45 ^{o}C) was used as the viscosity parameter. Before any measurement, the sample was set in the QLS cell assembly for at least 15 minutes to ensure thermal equilibration.

B-2 Data treatment programs

The BI-9000AT autocorrelator is equipped with software for analysis by Cumulants (from 1st-order to 4th-order), double exponentials (DBLEXP), exponential

sampling, non-negatively constrained least squares: multiple pass (NNLS) and regularized (CONTIN). Generally, we used CONTIN to analyze size distribution and the 2^{nd} or 3^{rd} Cumulant to calculate hydrodynamic sizes; the former is the best available method for the analysis of size distribution of polydisperse mixtures, and the latter is sufficiently reliable and accurate as long as the distribution is narrow and monodisperse. A more detailed explanation of the QLS data analyses will be given in Section D-3.

C QLS measurements of standard samples

C-1 Method validation

Measurements of polystyrene size standards were designed to check our laser scattering instrument, to develop QLS operational skills, and to accumulate practical experience with sample preparation, parameter optimization, data treatment, and problem solving. Another important purpose was to examine the behavior of a two-size distribution sample in QLS experiments.

As practice, 50 nm and 503 nm polystyrene standard samples were measured at different concentrations (by diluting a concentrated solution) until correct size results were obtained. In order to understand the QLS behavior of polydisperse samples, a mixture of 50 nm and 503 nm polystyrene standards was used to mimic the two-size distribution case.

Micelles of the detergent sodium dodecyl sulfate (SDS) in NaCl solution were found previously by QLS to have a rod shape (Mazer et al., 1976). In order to understand the process of shape determination by QLS methods, this work was repeated with a 20 mg/ml SDS sample in 0.45 M NaCl.

Bile salts are a family of amphipathic steroids used widely in biological research. Bile salts have extensive hydrophobic portions and easily form dimer or tetramer self-aggregates in aqueous media because of their specific molecular structure: one hydrophilic face with typically three hydroxyl groups and another hydrophobic face (Carey, 1985). However, QLS measurements for bile salt systems are often more difficult than detergents such as SDS due to their small size (weak scattering). In order to gain confidence in dealing with these samples, measurements were made for the smallest bile salt, taurocholic acid sodium salt (TC) in NaCl solution.

C-2 Materials and Sample Preparation

Standard polystyrene beads (50 ± 2 nm by Transmission Electron Microscopy (TEM) and 54 ± 2.7 nm by QLS; 503 nm (503 ± 4 nm by TEM) were purchased from Duke Scientific Corporation (Palo Alto, CA). They consisted of a 1-2% (w/v) aqueous solution of solid polystyrene beads containing 0.4-5% (w/v) of surfactant. The best water was always used for sample preparation and dilution.

A few drops of each polystyrene standard (50 nm or 503 nm) was transferred into a clean QLS cell and diluted with 1 ml of best water. After QLS measurement, the sample was gradually diluted and remeasured; the dilutions were repeated until no further changes in size were observed. After QLS experiments for single-size samples, a mixture of 50 nm and 503 nm beads was made by adding a few drops of the 503 nm solution to 1 ml of the 50 nm solution. (This protocol was also the basis for an exercise in the undergraduate Physical Chemistry Lab.)

The SDS sample was prepared by dissolving 20 mg of SDS in 1 ml of 0.45 M NaCl solution in a clean quartz QLS cell. The NaCl solution was filtered with a 0.2 μ pump filter before use.

The TC sample was prepared by dissolving 125 mg of TC in 5 ml of 0.60 M NaCl solution in a clean glass bottle. The NaCl solution was filtered with a 0.2 μ pump filter before use. 1 ml TC of the solution was transferred to a clean quartz QLS cell for QLS measurements.

C-3 QLS Results

Size and size distribution of polystyrene standards

QLS results for the dispersion of 50 nm polystyrene standards, in which the concentration dependence was removed by gradual dilution, are shown in Figure II-4. The size distribution was analyzed by CONTIN, demonstrating a highly monodisperse sample. The size was also calculated by the Cumulant method. Both CONTIN and Cumulants yielded the same size results. It should be noted that the mean size found by QLS was ~10% larger than that by TEM. This result is not surprising because the size measured by QLS is a so-called Z-average (Hiemanz and Rajagopalan, 1997); this average is based on the contribution to scattered intensity from each fraction, so that it favors the large size fraction. Similar results were obtained for the 503 nm sample (data not shown).

QLS results for the mixture of 50 nm and 503 nm beads are shown in Figure II-5. The CONTIN method clearly illustrates a two-size distribution. However, the sizes of the two fractions are found to shift toward the middle of the CONTIN diagram. Because the 503 nm fraction is much smaller in number, its size deviation is significantly larger than that of the 50 nm fraction. Furthermore, Cumulants fail to calculate the size of the individual aggregates; instead, the method yields an average size (55-103 nm) between the sizes of the two standards.

Size of 25 mg/ml taurocholic acid sodium salt (TC) in 0.6 M NaCl

QLS results obtained using both Cumulants and CONTIN methods yielded a hydrodynamic radius for the TC aggregates of 1.5-2 nm (Fig. II-6). This result was similar to published data (R_h=1.7 nm) (Mazer et al., 1976).

Fig. II-4: QLS results for a 50 nm polystyrene standard by Cumulants and CONTIN

Cumulants

	Amp	Diam(nm)	Gamma	Poly	Skew	Kurtosis	RMS Error
Linear	1.167	55.0	5112.7				1.52[illegible]E-04
Quadratic	1.167	54.6	5154.9	0.019			7.83[illegible]E-05
Cubic	1.167	54.4	5171.0	0.034	3.45		6.94[illegible]E-05
Quartic	1.167	54.0	5209.6	0.089	7.17	26.88	4.31[illegible]E-05

CONTIN

Percent	Lower	Upper
By Inten.	100	0
By Weight	100	0
By Number	100	0

Mean = 55nm
Var. = 0.002
Skew = 0.047

RMS = 9.57E-05

50nm Polystyrene Size Standard

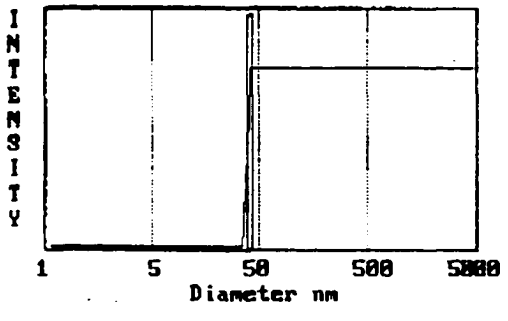

d/nm	G(d)	C(d)
27	0	0
29	0	0
31	0	0
33	0	0
36	0	0
38	0	0
41	0	0
44	0	0
47	0	0
50	22	14
54	100	76
58	39	100
62	0	100
67	0	100
71	0	100
76	0	100
82	0	100
dust	0	100

Fig. II-5: QLS results for mixture of a 50nm/503nm standards by Cumulants and CONTIN

Cumulants

Polystyrene 50/500 Mixture

	Amp	Diam(nm)	Gamma	Poly	Skew	Kurtosis	RMS Error
Linear	1.233	102.9	2452.9				6.520E-03
Quadratic	1.246	84.9	2974.7	0.199			4.170E-04
Cubic	1.251	77.6	3251.8	0.328	0.25		2.360E-03
Quartic	1.253	74.5	3387.7	0.395	0.43	3.08	3.180E-04

CONTIN

Percent	Lower	Upper
By Inten.	100	0
By Weight	100	0
By Number	100	0

Mean = 133nm
Var. = 0.758
Skew = 0.983

RMS = 3.57E-04

Polystyrene 50/500 Mixture

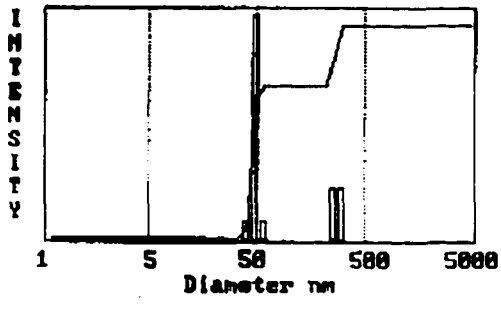

d/nm	G(d)	C(d)
21	0	0
25	0	0
30	0	0
35	0	0
42	0	0
50	9	5
60	100	62
71	9	67
84	0	67
101	0	67
120	0	67
142	0	67
169	0	67
202	0	67
240	0	67
286	24	80
340	24	94
dust	11	100

Fig. II-6: QLS results for 25 mg/ml TC in 0.6 M NaCl by Cumulants and CONTIN

Cumulants

TC(25mg/ml) in NaCl(0.6M)

	Amp	Diam(nm)	Gamma	Poly	Skew	Kurtosis	RMS Error
Linear	1.247	4.9	51542.4				2.390E-02
Quadratic	1.262	3.4	74409.8	0.237			2.250E-02
Cubic	1.261	3.5	72582.8	0.188	-0.38		2.260E-02
Quartic	1.255	4.1	61285.9	0.085	-2.93	1.04	2.250E-02

CONTIN

Percent	Lower	Upper
By Inten.	100	0
By Weight	100	0
By Number	100	0

Mean = 3nm
Var. = 0.011
Skew = 0.290
RMS = 2.17E-02

TC(25mg/ml) in NaCl(0.6M)

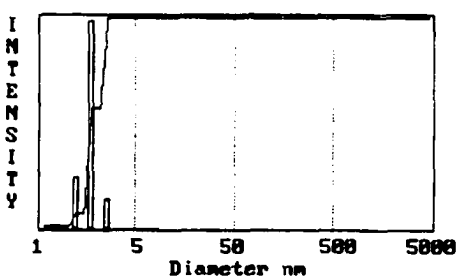

d/nm	G(d)	C(d)	d/nm	G(d)	C(d)
1	0	0	4	0	100
1	0	0	5	0	100
1	0	0	5	0	100
1	0	0	6	0	100
1	0	0	6	0	100
2	0	0	7	0	100
2	0	0	7	0	100
2	0	0	8	0	100
2	0	0	9	0	100
2	0	0	9	0	100
2	0	0	10	0	100
2	25	7	11	0	100
3	66	27	12	0	100
3	100	56	13	0	100
3	89	82	14	0	100
3	49	96	dust	0	100
4	14	100			
4	0	100			

Shape of SDS micellar aggregates in NaCl solution

The dependence of scattered intensity on hydrodynamic radius R_h for SDS solutions was obtained from QLS measurements at different temperatures. Both hydrodynamic radius and scattered light intensity were measured simultaneously as a function of temperature in the range of 15-45°C. CONTIN analysis showed a monodisperse size distribution for the SDS micelles, but the size distribution spanned a range of ~15 nm, possibly because of insufficient equilibration time. However, the results from Cumulants were very similar. The 3rd Cumulant was used to calculate the hydrodynamic radius in each case, because the 3rd Cumulant gives a better correlation for broad distribution samples than the 2nd Cumulant. The curve of scattered intensity vs. hydrodynamic radius R_h was fit by a 3rd order polynomial as shown in Figure II-7.

Based on the results shown in Fig. II-7, a curve of experimental intensity ratio (I/I_{min}) vs. R_h was compared with the theoretical *MP* vs. R_h curves corresponding to each model of aggregate shape (Fig. II-8) (Mazer et al., 1976). Because the hydrodynamic radius of SDS aggregates approaches a minimum value of 2.5 nm with increasing temperature and is independent of the concentration of NaCl or SDS, the thickness of the disk and the diameter of the rod (Fig. II-9) are taken to be twice the length of an SDS molecule (5.0 nm) (Mazer et al., 1976). Here all intensities are normalized to the I_{min} corresponding to R_h=2.75 nm, the smallest size obtained in our QLS measurements. Fig.II-8 confirmed that the shape of the SDS micelles in NaCl

solution is a cylinder-like rod, in agreement with the published literature (Mazer et al., 1976). To describe the SDS micellar aggregates, the rod-shape model is displayed in Figure II-9.

Fig. II-7: Scattered intensity dependence on hydrodynamic radius R_h for SDS aggregates measured at different temperatures (15-45 °C)

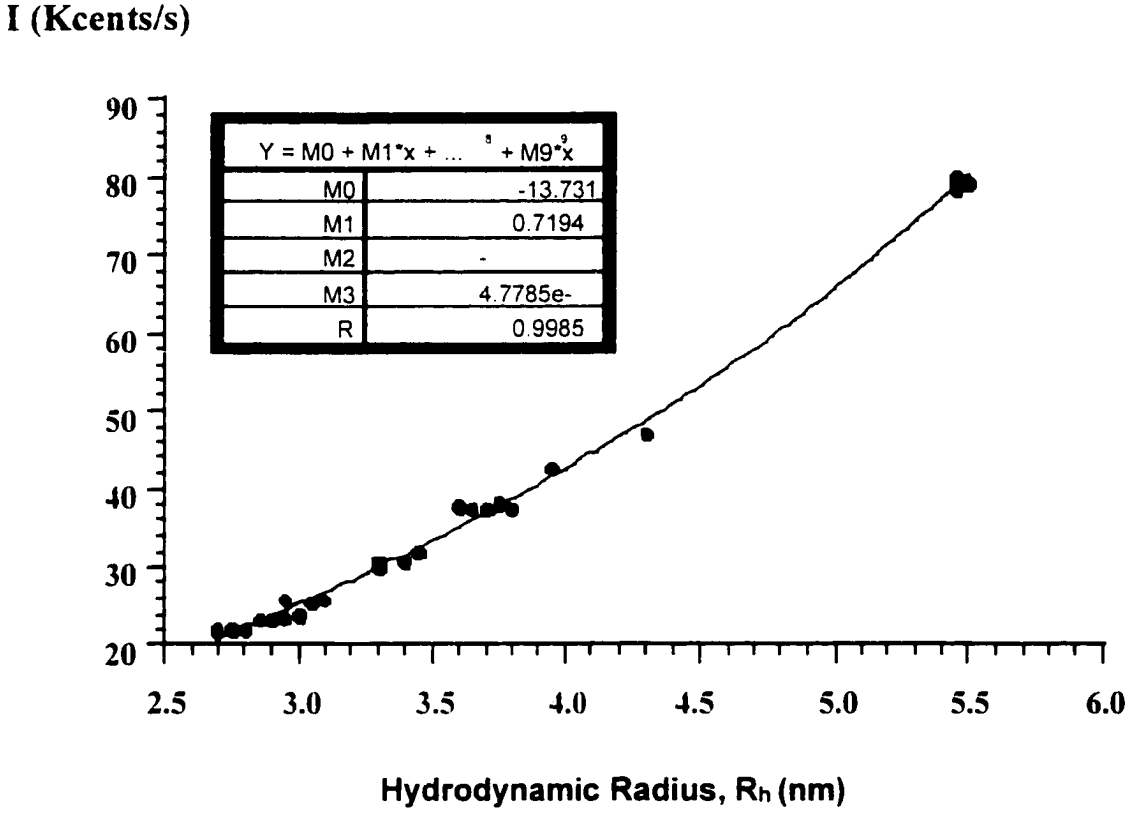

Fig. II-8: Shape determination for 20 mg/ml SDS micelles in 0.45 M NaCl

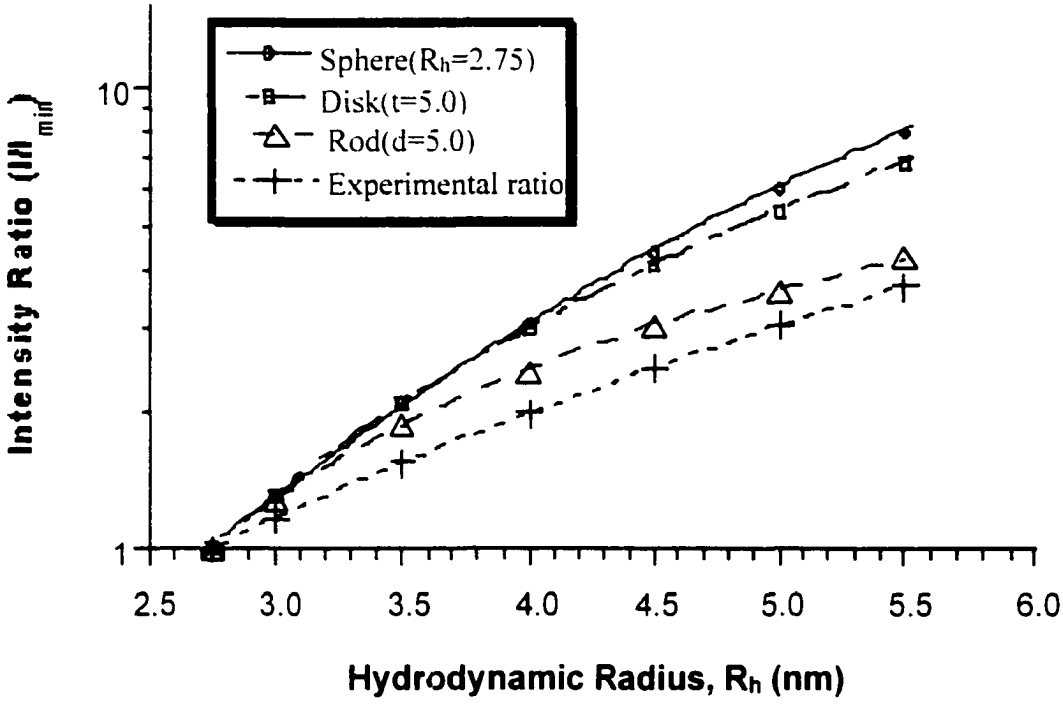

Fig. II-9: Rod-shaped model of SDS micellar aggregates in 0.45 M NaCl

a) Longitudinal section

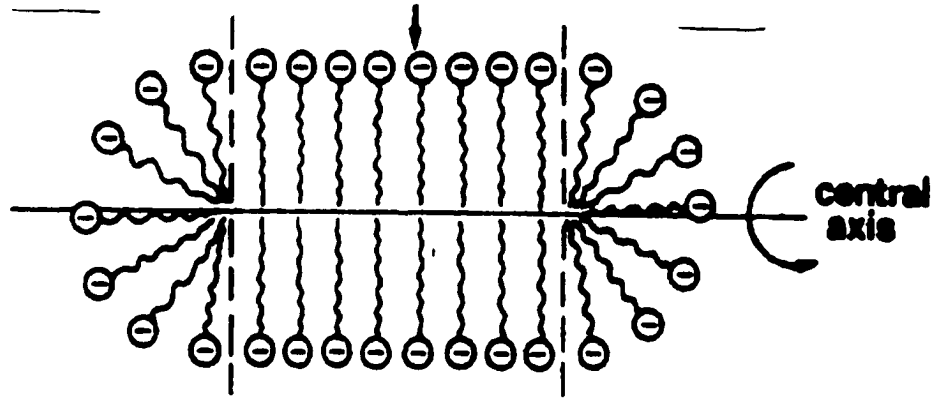

b) Cross section

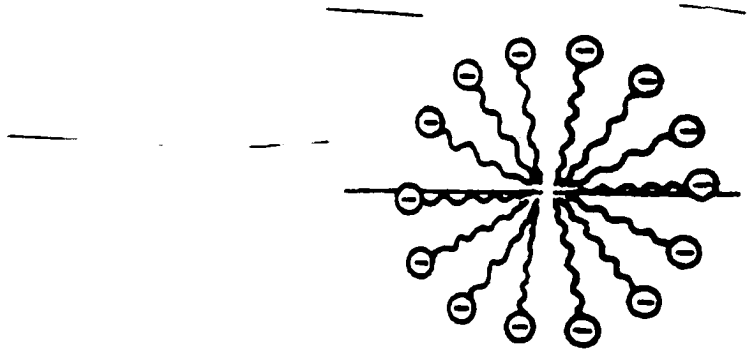

D Discussion

These tests validated the use of QLS methods for determinations of size, size distribution, and shape of lipid aggregates, but they also revealed a number of caveats and limitations.

D-1 Evaluation of size and size distribution by QLS

The QLS technique is based on the measurement of diffusional motion for a solution of scatterers. There are two physically distinct translational diffusion coefficients: the self-diffusion coefficient D_s and the mutual diffusion coefficient D_m. The former measures the diffusional motion of an identified particle through a uniform environment, and it is sensitive to the concentration of the system. The latter indicates the molecular diffusion due to a concentration gradient, and it is relatively independent of the concentration of the system (Phillies, 1990). Because the translational diffusion coefficients are less affected by intermolecular interactions than other parameters like osmotic pressure and sedimentation coefficient, QLS has remarkable advantages for size measurement in macromolecular solutions and micellar systems. Since the autocorrelation function is recorded as an assembly of contributions from various size fractions, QLS can also solve the size distribution problem, which cannot be done by classical SLS methods. The ability to analyze size and size distribution for relatively small particles makes the QLS technique very useful in the study of biological mixtures.

D-2 Overestimation of size in QLS

For a sample with a narrow monodisperse size distribution, the Cumulants method offers sufficient accuracy for size analysis. But if the sample aggregates have a broad monodisperse or even a two-size distribution, QLS data analysis uses the Z-averaged mode, which is a statistical method defined by Eq. II-10:

$$M_Z = \Sigma Z_i M_i / \Sigma Z_i = \Sigma W_i M_i^2 / \Sigma W_i M_i = \Sigma n_i M_i^3 / \Sigma n_i M_i^2 \qquad \text{(Eq. II-10)}$$

Because the Z-averaged mode favors larger-sized fractions, QLS usually yields an over-estimated size value. Compared with the size found by TEM, 10% overestimation by QLS is expected (Manual, Duke Scientific Corporation). On the other hand, for aqueous solutions, hydration will legitimately increase the size since their diffusional motion includes at least one shell of water around the scatterers. These effects were observed experimentally in the measurement of the 50 nm polystyrene size standard (Fig. II-5).

D-3 Challenges of polydisperse samples

Once a second large-size fraction is present, even in trace amounts, both Cumulants and CONTIN fail to provide reliable size information. The dominant

intensity contribution from the large fraction is a great obstacle to data treatment. The signals from the small fraction may be obscured or even eliminated by the signals from the large size fraction. Cumulant analysis shows only a Z-average of all size fractions, as noted above. Although the Laplace-inverse method (CONTIN) can deal with the polydispersity problem, it is very sensitive to noise in the QLS data. The results shown in Fig. II-6 demonstrate that CONTIN analysis produces size deviations for both 50 nm and 503 nm standards. However, CONTIN remains still the best method available for size estimation in polydisperse samples.

D-4 Effects of sample concentration and viscosity

Although the mutual diffusion coefficient is not highly sensitive to concentration, it is not completely independent of this variable. Generally, sample concentrations used for QLS are about 10-30 mg/ml (Phillies, 1990). Once the concentration is higher than this limit, molecular interactions may affect the rate of diffusive motion, and such effects can be either positive or negative. In addition to mutual diffusion, repeated collisions between the scatterers may increase the scattered intensity, and the problem will become more serious as the sample concentration rises. It must be demonstrated that there is no measurable dependence of scattered intensity on sample concentration before the QLS results can be used with confidence.

The viscosity of the solvent (i.e. water) is used in Eq. II-5 as a viscosity parameter. For macromolecular solutions and aqueous biological assemblies, the solvent viscosity may be significantly different from the viscosity of the sample solution. An underestimated viscosity in Eq. II-5 will result in an overestimated size. In addition, the BI-9000AT instrument has a limitation that the product of aggregate size (diameter) in μm and the viscosity of the solution in cP must be smaller than ~2-5. Otherwise the experimental results are not considered reliable.

D-5 Shape deduction by QLS

Light scattering (SLS and QLS) techniques offer possible experimental approaches to analyze the shape of micellar aggregates. With SLS, when scatterers are sufficiently large (mean radius of gyration R_g ≥10 nm) to produce an angular dependence in the time-averaged scattered intensity that can be measured as a dyssymetry ratio d(θ) (defined as the ratio of the ratio of scattering form factor P at supplementary angles), the shape of the scatterers can be deduced based on the relationship between mean radius of gyration R_g and hydrodynamic radius R_h (Young et al., 1978). Alternatively, for QLS, a comparison of scattered intensity ratio at constant concentration with theoretical predictions of this ratio derived from R_h using different shape models (as shown in Appendix A) can be used to deduce the shape of the scatterers (detailed in A-3) (Mazer et al., 1980).

Because of the factor of mean radius of gyration R_g, the first method is not able to deal with aggregates of small size (<10 nm), in which the angular dependence of the scatterers can be identified by the time-averaged scattered intensity. Specifically, the method is not suitable for the fat digestive model mixtures and binary phospholipid bicelles of interest in this work.

The QLS method has no such minimum size limitation, so it is suitable for SDS micelles and the fat digestive model mixtures and phospholipid bicelles described in Chapter III and IV. However, once the size distribution of the scatterers becomes broad or even a two-size distribution, the method will fail to yield the shape of the scatterers. No data treatment method for polydisperse samples satisfies the accuracy requirements of shape analysis. It can be challenging to prepare a narrow monodisperse sample for QLS purposes, and to keep it that way when temperature, total concentration, or molar ratio of molecular aggregates are changed. This requirement may demand very careful sample preparation, sufficiently long times to achieve a homogeneous and stable mixture, and very clean glassware and chemicals. However, it is still feasible. As long as the sample maintains a narrow monodisperse size distribution, it should be possible to obtain shape information from QLS experiments.

Chapter III Solution NMR and QLS studies of model mixtures for fat digestion and transport

A Introduction

Dietary fats (mainly triglycerides) supply a majority of the energy of human daily activity because they are highly reduced and anhydrous. An adult Western man consumes about 150 g of triglyceride and 4-8 g of phospholipids per day (Carey et al., 1983). Both digestion and absorption of dietary fats play important roles in human health. Those people suffering from dysfunction in fat digestion may have various health problems in nutrition, brain development, and obesity. To understand the mechanism of fat digestion, prior investigations have used the methodologies of biology, physical chemistry, nutrition, enzymology, and medicine.

Gastrointestinal fat digestion requires three sequential steps (Carey et al., 1983): 1) the separation of bulk fat globules into finely emulsified particles (<500 nm in diameter), 2) the hydrolysis of fatty acid esters by enzymes, and 3) the desorption and dispersion of hydrophobic fat products into an absorbable form. The digestion of fats requires interaction between fats and water-soluble enzymes. Because hydrophobic fats and hydrophilic enzymes are present in two different phases, the interaction of fats with enzymes must occur at the interface of fatty aggregates, so that the structure of these digestive assemblies can provide important information to understand the process of dietary fat digestion.

Although the enzymatic hydrolysis of fats is considered to begin as early as in the mouth and stomach, where up to 30% of fats may be digested, quantitative hydrolysis and absorption of dietary fats proceed in the upper small intestine. The lumen and mucosa of the upper small intestine supply an appropriate environment of less acidity (pH 5-7), lipases and bile salts, and specialized absorptive cells for fat hydrolysis (Hamosh, 1990). We focus our study on the micellar late-stage of fat digestion because it is the rate-limiting step for dietary fat absorption.

The mechanism of intestinal lipid absorption consists of two parts: how they reach microvillus membrane of the enterocyte and how they are transported across the brush border membrane of the enterocyte to be metabolized. It is generally accepted that bile salts (BS) play a key role in facilitating hydrolyzed lipid through the unstirred water layer to the absorption site. However, the molar ratio of fatty acid to bile salt is an important factor that may alter the route of lipid absorption. Different molar ratio lipid-bile salt systems (low ratio, ~0.2-0.5; high ratio, ~1.3-2.6) may have different absorptive mechanisms (diffusion or collision controlled), since their aggregation-states may be different.

Because of the functional importance of late-stage digestive aggregates in fat utilization, understanding the digestive aggregate structure is a vital step toward description of this physiology. Directed by prior research results (Chen, 1996), we designed late-stage model mixtures that consist of a bile salt (taurocholic acid sodium

salt, TC), C_8-based fatty acid (octanoic acid, FA), and monoglyceride (1-monocapryloyl-*rac*-glycerol, MG) in physiologically appropriate ratios, to mimic fat digestion in the upper small intestine. We used C_8-based fatty acids in the fat digestive model mixtures for three reasons: 1) C_8-based fatty acids are the main digestive product of milk and butter; 2) significant research work had been done on long-chain fatty acids (oleic acid, monoolein, and diolein) using dynamic light scattering (QLS) (Staggers et al., 1990) and both ^{2}H NMR and X-ray diffraction patterns (Westerman, 1995); and 3) short- and medium-chain fatty acids are administered therapeutically to patients suffering from digestive dysfunction.

To deduce a structural model for late-stage fat digestive aggregates, we obtained the necessary information from NMR and QLS experiments. Here, NMR techniques helped us to determine the intermolecular arrangement and interfacial groups in fat digestive aggregates. QLS measurements provided the size and size distribution of these particles. Furthermore, QLS analyses indicated that these aggregates adopt a rod shape. NMR and QLS together allowed us to propose a rod-shaped organizational model for fat digestive aggregates.

Since fat digestion is a dynamic process and the molar ratio between FA, MG, and TC will always vary during the course of fat digestion, the organizational structure of fat digestive aggregates may be different at various stages of digestion. Our NMR and QLS data were collected from two different model mixtures at constant total

concentration (2.0 g/dl): FA:MG = 20:1 (NMR results from Chen Zhenjia) and FA:MG = 10:1 (this work).

A series of mixtures that contain long-chain (18:1) fatty acids and sodium taurocholate (TC) have been studied in the context of fatty acid transport by our collaborators Judith Storch and Shiuying Ho at Rutgers University. Based on our work for fat digestive model mixtures, we used the same investigative protocol (NMR spectroscopy and QLS) to study these fatty acid-TC aggregates. Because the oleic acid-TC system has better solubility in aqueous solution than other model systems, 1:1 and 1:2 molar ratios with TC at 10 mM were studied first.

B Experimental

B-1 Samples

B-1.1 Materials

Commercial octanoic acid (99.5% FA) was purchased from Aldrich Chemical Company, Inc. (Milwaukee, WI). 1-monocapryloyl-*rac*-glycerol (99% MG) and taurocholic acid sodium salt (98% TC) were purchased from Sigma Chemical. Co. (St. Louis, MO). Deuterium oxide was purchased from Cambridge Isotope Laboratories (Woburn, MA). Oleic acid (OA, 100 mg/ml in hexane) was purchased from Doosan

Serdary Research Laboratories (Englewood, NJ) and was supplied by the Storch group at Rutgers University. All chemicals were used without further purification.

B-1.2 Sample preparation

To prepare model digestive mixtures, octanoic acid (FA), 1-monocapryloyl-*rac*-glycerol (MG), and taurocholic acid sodium salt (TC) were dissolved in a 50:50 (v/v) $CH_3OH/CHCl_3$ mixture. The solution was blown into a dry film with N_2 gas and subjected to a vacuum overnight to remove any remaining organic solvents. The dry film was rehydrated in the required volume of buffer solution (100 mM phosphate, 150 mM NaCl, pH 6.5). The samples were stored in the refrigerator (~4°C) until use.

The C_8-based fat digestive model mixtures had a total lipid concentration of 2.0 g/dl and molar ratio TC: (FA+MG) = 20:80. The ratio FA:MG was set to 10:1 and 20:1 in different mixtures. NMR samples included a D_2O buffer, and QLS samples used a best water buffer (deionized water filtered twice with a 0.2 μ syringe filter). The resulting aqueous mixtures formed optically clear solutions.

A buffer solution, including 137 mM NaCl, 2.7 mM KCl, 1.5 mM KH_2PO_4, and 8 mM Na_2HPO_4 (pH 7.4), was made by dissolving all weighed chemicals in the required volume of autoclaved best water. The solution was filtered with a 0.2 μ pump

filter to remove dust. The buffer solution was kept in the freezer (-12°C) to avoid bacterial growth.

To prepare model mixtures for fatty acid transport mixtures (OA/TC=1:1) for QLS measurements, 10 mg OA (0.1 ml hexane solution) was transferred to a clean glass bottle and placed under vacuum at least overnight to evaporate the hexane solvent. After adding 19 mg TC, 3.54 ml buffer solution (pH 7.4) was added to dissolve the dry OA film and TC powder. The solution was a little cloudy at first, and then it became clear. The sample for NMR experiments was prepared in the same way, but D_2O (99.9 %) was used instead of water. To change the molar ratio of OA/TC solution from 1:1 to 1:2, a certain volume 1:1 solution was transferred to another clean bottle, then the same volume of 10 mM TC buffer solution was added to double the TC molar ratio. Analogous steps were used to further decrease the OA/TC molar ratio.

B-2 NMR experiments

All 1D and 2D solution NMR experiments were performed using a Varian Unity*INOVA* U600 (^{1}H resonance frequency at 600 MHz) spectrometer at the College of Staten Island/CUNY. Data were processed using Varian software on a Sun workstation.

For the fat digestive mixture (10:1), the 1D ^{1}H spectrum, as well as the Mn^{2+} titration spectra, were acquired at 30°C with a one-pulse sequence with a typical 9.8 μs 90° pulse. All peaks were referenced to the TC-18 methyl protons (0.73 ppm) (Chen, 1996). The 2D COSY experiment was run with the double-quantum filter pulse sequence (DQF-COSY), with an 8.4 μs 90° pulse. The 2D TOCSY and NOESY data were acquired with Varian pulse sequences using 8.4 μs and 5.5 μs 90° pulses, respectively. The mixing time was 50 ms for TOCSY, 100 ms and 200 ms for NOESY. Typically, 256 scans were used in 2D NMR experiments.

For OA/TC NMR experiments, including the 1D ^{1}H spectrum, 2D gradient DQF-COSY, TOCSY, and NOESY, were performed using new Nanoprobe with MAS spinning (500 Hz and 1900 Hz) at 20°C. A 12 μs 90° pulse was used in 1D ^{1}H, 2D COSY, TOCSY experiments, and 5.5 μs in the 2D NOESY experiment. 256 scans were acquired for all 2D datasets.

NMR experiments for lipid semi-solid samples were performed using a Varian Unity*plus* U300 instrument at the College of Staten Island/CUNY. Data were also treated with Varian software on a Sun station. All experiments used Varian pulse sequences, except the 2D SEVACP used an in-house sequence. Three different probes (7mm Varian, 5mm triple-resonance DOTY, 5mm XC-5 DOTY), were used in these experiments. The temperature for each probe was calibrated by observing changes in

the ^{1}H NMR spectrum during the melting of selected crystalline compounds (Neue and Dybowski, 1997) (Section V B-2).

B-3 QLS experiments

QLS measurements for fat digestive mixtures (20:1 and 10:1) and the fatty acid transport mixture (OA/TC=1:1 and 1:2) were performed using the BI-9000AT laser light scattering instrument. Data were analyzed using installed Brookhaven software. The work followed the same conventions as described in Chapter II.

For any QLS measurement, the sample was equilibrated at the required temperature for at least 20 minutes before data were acquired. To dilute the concentration of fat digestive mixtures, the necessary volume of buffer solution was added. To double the molar ratio of TC in the OA/TC mixture, the same volume of 10 mM TC buffer solution was added to the original sample. As recommended by the Storch group, the OA/TC solution was first shaken at 37°C and 125 Hz/minute for one hour in a Q24 Environmental Incubator Shaker.

C Results

C-1 NMR results for a fat digestive model mixture (10:1)

C-1.1 Assignment of the ^{1}H NMR spectrum of a 10:1 fat digestive model mixture

Before we can interpret 2D NOESY and ROESY NOE cross-peaks and locate specific polar groups at the surface of fat digestive aggregates, we need to assign all ^{1}H peaks based on 2D COSY and TOCSY NMR spectra. The 2D DQF-COSY spectrum of the 10:1 fat digestive mixture is shown in Figure III-1. By reference to published data (Barnes and Geckle, 1982; Halvorsen et al., 1989; Davis and Thompson, 1993; Croasmun and Carlson, 1994), some particular TC protons could be easily assigned: methyl protons TC-18, TC-19, and BS-8; methylene protons TC-25, TC-26, and FA-2; and protons of TC-3, TC-7, and TC-12 that are attached to carbons with hydroxyl groups. The assignment of COSY cross-peaks starts from TC-3, TC-7, and TC-12 step by step through pairwise J-coupling correlations. In order to overcome some ambiguities due to peak overlap on the diagonal, a 2D TOCSY spectrum (Figure III-2), was used to identify extended networks of J-coupled protons found in the acyl chains that are unique to the FA constituent.

Figure III-3 shows the 600 MHz 1D ^{1}H NMR spectrum of a 10:1 fat digestive model mixture, along with the assignments derived from 2D COSY and TOCSY

spectra. Here all chemical shifts were referenced with respect to CH_3-18 protons of TC at 0.73 ppm. The complete ^1H chemical shift assignments for taurocholate (TC) and caprylic acid are presented in Table III-1. For comparison, the TC chemical shift assignments of a 20:1 fat digestive mixture (Chen, 1996) are also shown in Table III-1. The strong agreement of their respective chemical shifts suggests similarities in their aggregate structures.

Fig. III-1: 2D DQF-COSY spectrum of late-stage (10:1) fat digestive model mixture (The numbering scheme is shown in Fig. III-3)

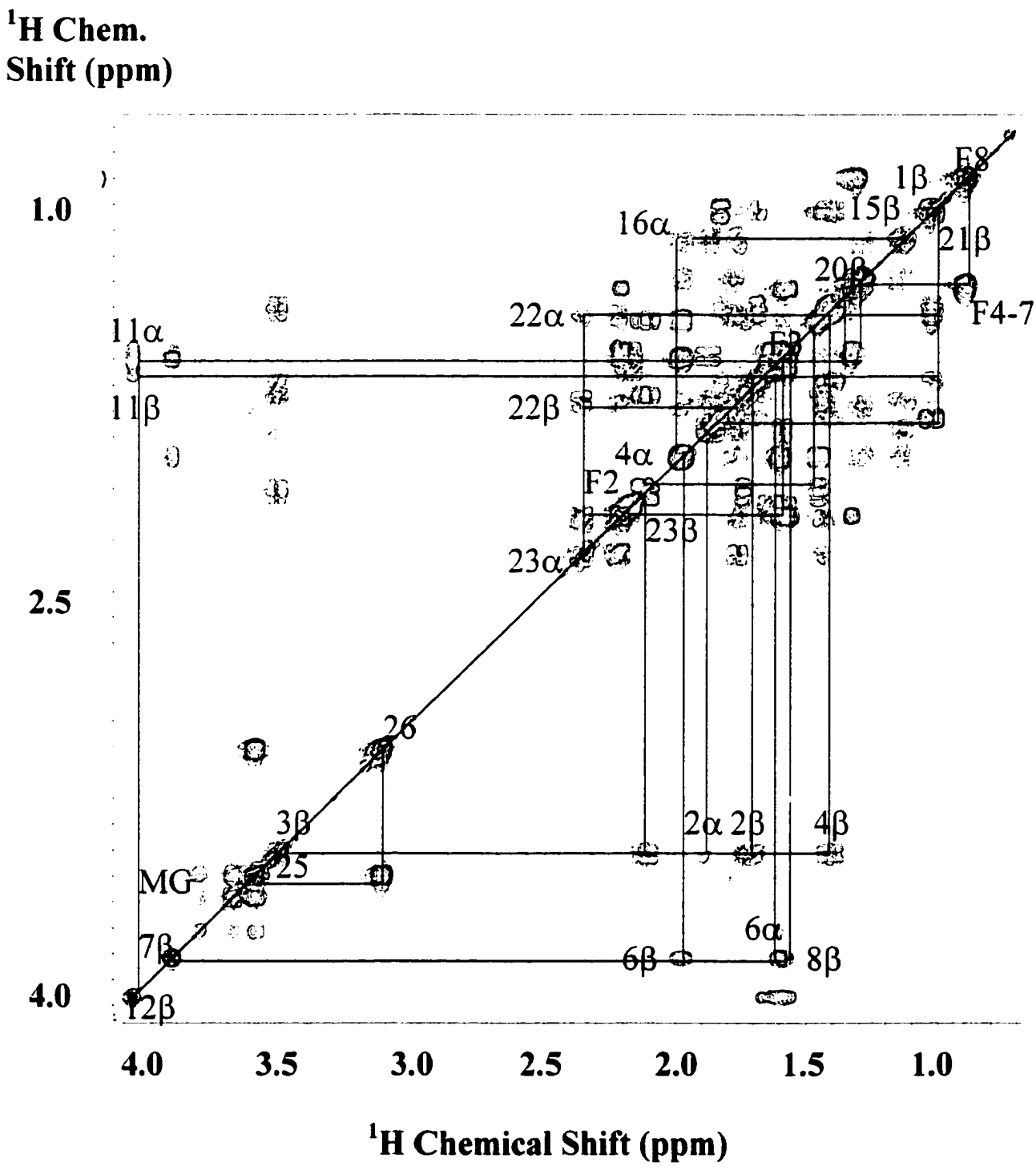

Fig. III-2: 2D TOCSY spectrum of late-stage (10:1) fat digestive model mixture, obtained with a mixing time of 50 ms. (The numbering scheme is shown in Fig. III-3)

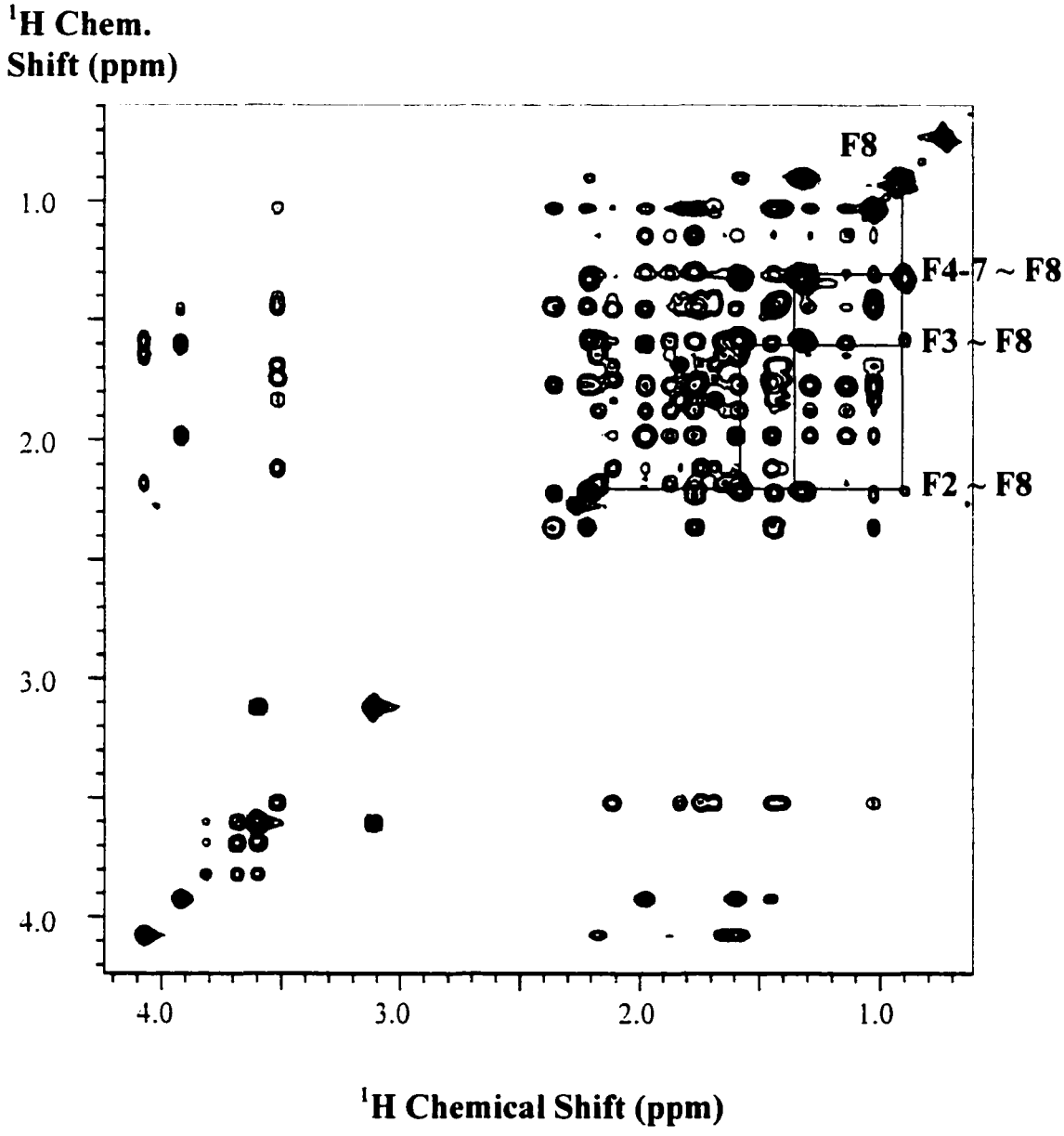

Fig. III-3: Assigned ^{1}H spectrum of late-stage (10:1) fat digestive model mixture

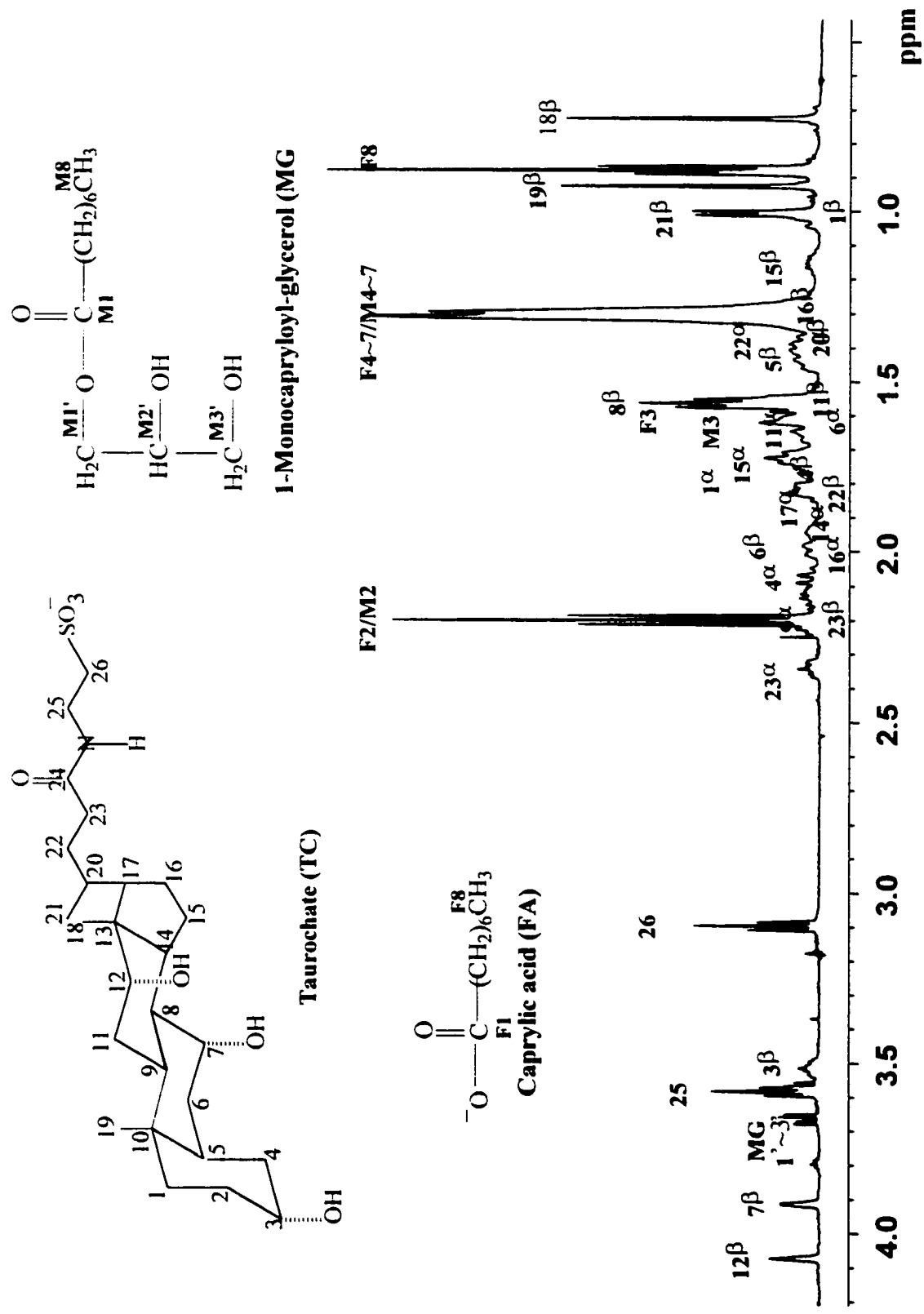

Table III-1: ^1H chemical shift assignments for TC and C_8 FA in fat digestive model mixtures

Number of TC proton	10:1 model mixture		20:1 model mixture*	
	α	β	α	β
1	1.84	1.03	1.84	1.01
2	1.41	1.69	1.43	1.70
3		3.51		3.52
4	2.12	1.75	2.15	1.75
5		1.46		1.44
6	1.61	1.97	1.63	1.95
7		3.92		3.92
8		1.57		1.55
9	2.18		2.18	
10				
11	1.66	1.58	1.66	1.59
12		4.07		4.06
13				
14	1.89		1.92	
15	1.79	1.14	1.80	1.12
16	1.98	1.29	2.01	1.29
17	1.79		1.82	
18		0.73		0.73
19		0.93		0.93
20		1.41		1.44
21		1.03		1.02
22	1.43	1.76	1.48	1.75
23	2.37	2.20	2.37	2.21
25	3.60		3.59	
26	3.11		3.11	
FA2	2.20		2.24	
FA3	1.57		1.60	
FA4-7; MG4-7	1.31		1.34	
FA8; MG8	0.88		0.91	
MG1'			4.19	
MG2'	3.80		4.00	
MG3'	3.67		3.64	

* Data from Z. Chen's Ph.D. thesis (Chen, 1996).

C-1.2 Molecular arrangement in fat digestive aggregates through NOE cross-peaks: NOESY

Since NOE cross-peaks appearing in the 2D NOESY spectrum yield information about spin correlations through space, this experiment is a powerful tool for analyzing the conformation of biomolecules and molecular structure of micellar aggregates. However, due to the relatively narrow chemical shift range of ^1H nuclei, the NOESY spectrum may be seriously overlapped for biomolecules and molecular aggregates. As noted in Chapter I, Section C-4, another inherent drawback of NOESY measurements is that the NOE signal could be rather weak for medium size molecules ($\omega\tau \approx 1$) (Croasmun and Carlson, 1994).

The 2D NOESY spectrum of the 10:1 fat digestive model mixture is shown in Figure III-4. To avoid spin diffusion artifacts, the NOESY spectrum was acquired at a relative short mixing time (200 ms). Although the experiment was performed at a ^1H resonance frequency of 600 MHz, the peak resolution is still not sufficient to identify all NOE cross-peaks unambiguously.

Because intermolecular through-space NOE peaks may appear in the NOESY spectrum, and intramolecular cross-peaks from geminal and vicinal protons appear in both TOCSY and NOESY spectra, it is possible to isolate the intermolecular NOE cross-peaks by comparing TOCSY and NOESY spectra. For example, TC18 or TC19

will not show cross peaks in the TOCSY spectrum because they are separated by a tertiary carbon. However, they may exhibit valuable intermolecular NOE cross peaks.

Fig. III-4: 2D NOESY spectrum of late-stage 10:1 fat digestive model mixture. Negative peaks (shown in red color) are described in the text

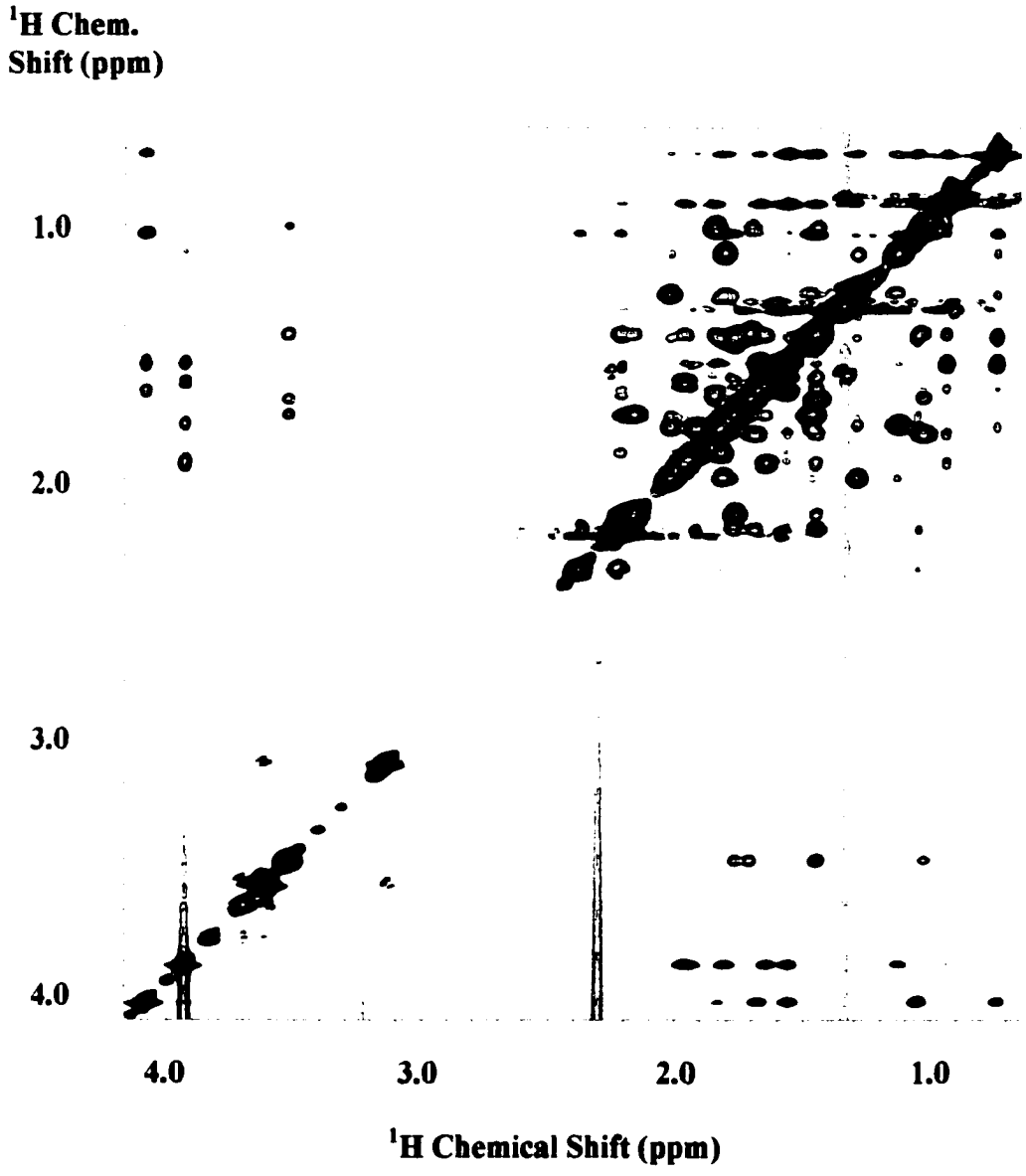

Another interesting phenomenon exhibited by the NOESY spectrum is that FA chain protons, TC-25, and TC-26 show both positive and negative NOE cross-peaks. It is known that large molecules and molecular aggregates display the same sign cross-peaks as the diagonal peaks (negative NOE) because they tumble slowly. On the other hand, small molecules exhibit opposite sign cross-peaks to the diagonal peaks (positive NOE) since they move rapidly. The observation of both positive and negative NOE cross-peaks for TC-25, TC-26, and FA implies two conclusions: the side chain of TC is more mobile than its steroid domain, and some free FA molecules may be located outside of the aggregates. After comparison of TOCSY and NOESY data as described above, some valuable intermolecular interactions (TC-TC and TC-FA) may be identified from the NOESY spectrum (Table III-2 (a) and (b)). Because some NOE cross peaks could be missing from the NOESY spectrum, the ROESY data (not shown) were also analyzed. No additional information appeared in the ROESY spectrum.

These long range NOE cross peaks, such as between TC methyl protons and the protons at TC carbons with hydroxyl groups (3β, 7β, 12β), are found in 10:1 fat digestive mixture, but not in TC alone (Chen, 1996), indicating the formation of large aggregates and the presence of TC dimers or tetramers. Furthermore, the assigned intermolecular (TC-FA) NOE cross peaks define the organization of FA-TC molecules. An arrangement between TC and FA molecules is illustrated in Figure III-5. Here four FA molecules are shown since the molar ratio of TC:FA = 1:4.

Table III-2: (a) Important intermolecular (TC-TC) NOE cross peaks

(b) Important intermolecular (TC-FA) NOE cross peaks

(a)

Assignment*	Chem. Shift connectivity (ppm)
12β - 19	4.06 – 0.93
7β - 15	3.92 – 1.12
7β -19	3.92 – 0.93
7β - 18	3.92 – 0.73
15 /17α /1α - 18	1.80 – 0.73
11α /6α / - 18	1.66 – 0.73
18 - 19	0.93 – 0.73

* Alternative assignments are separated by a slash as a/b.

(b)

Bile salt (TC)	Fatty acid (C_x)	Chem. shift connectivity (ppm)
5β	FA(8)	1.46 – 0.91
6β	FA(8)	1.97 – 0.91
15β	FA(3)	1.14 – 1.57
16β	FA(2)	1.29 – 2.20
20	FA(2)	1.41 – 2.20
21β	FA(2)	1.03 – 2.20
15α/22	FA(2)	1.79 – 2.20

Fig. III-5: Aggregate organization of TC and FA based on their NOE proximities

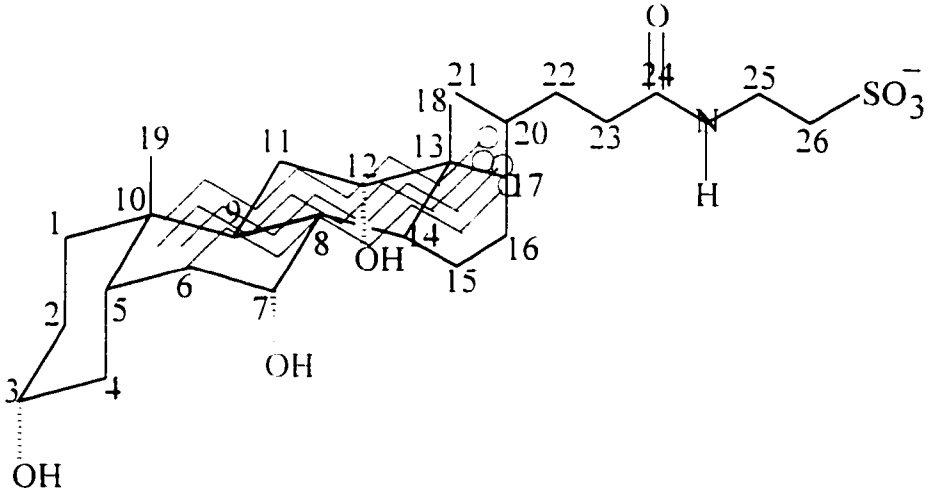

C-1.3 Mn^{2+} titration: water accessibility of the surface groups in fat digestive model aggregates

The presence of a small amount of paramagnetic compound, for example a salt of manganese ion (Mn^{2+}), will result in NMR peak broadening of resonances from nearby ^{1}H and ^{13}C nuclei, because paramagnetic impurities markedly accelerate the spin-spin (T_2) relaxation (Wang et al., 1992, a). This property of a paramagnetic compound makes it a sensitive tool to probe surface accessibility of polar functional groups at the interface of aqueous micellar aggregates.

We used Mn^{2+} titration ^{1}H NMR experiments to determine the arrangement of FA, MG, and TC molecules. The ^{1}H stacked plots of the 10:1 fat digestive model mixture during Mn^{2+} titration are shown in Figure III-6. Significant peak broadening was found for certain proton resonances, including TC-25, TC-26, and FA2.

Figure III-6 reveals several evident differences among molecular sites: 1) the protons at TC-7 and TC-12 do not show line broadening; 2) TC-25 and TC-26 show line broadening as Mn^{2+} concentration increases; 3) FA-2 also shows line broadening, and this site looks even more sensitive to Mn^{2+} than TC-25 or TC-26. The first point strongly suggests that hydroxyl groups of TC are shielded from water media. This argues against a disk-shaped aggregate such as that reported for lecithin-TC aggregates, in which TC molecules form a shell with the hydrophilic side of TC facing outward to

water (Mazer et al., 1980). For this reason, it also opposes our early model of micellar organization (Wang et al., 1992, b). The second and the third observations suggest that the side chain of the TC molecule and the polar end of the fatty acid extend into the aqueous environment in mixed FA-TC aggregates. The line broadening trends upon Mn^{2+} titration 20:1 and 10:1 fat digestive model mixtures are very similar qualitatively, though quantitative comparisons are unwarranted in light of uncertainties in the Mn^{2+} concentrations.

C-2 QLS results for fat digestive mixtures (20:1 and 10:1)

C-2.1 Size and size distribution

Besides size analysis, an important application of the QLS technique is the measurement of size distribution, because the overall decay of the autocorrelation function can be measured and analyzed for each size fraction according to its weighted-average decay rate. Figure III-7 shows the QLS results for the fat digestive model mixtures analyzed by the CONTIN method. These CONTIN analyses demonstrate that both 20:1 and 10:1 fat digestive model mixtures consist of two-size aggregates. Judging from either the number or mass of scatterers, the small size aggregates dominate over the larger size. Even though the large size aggregates are close to negligible in number or mass, they have a significant contribution to the total scattered intensity.

Fig. III-6: Stacked plots of ^{1}H spectra of 10:1 fat digestive model mixtures by Mn^{2+} titration

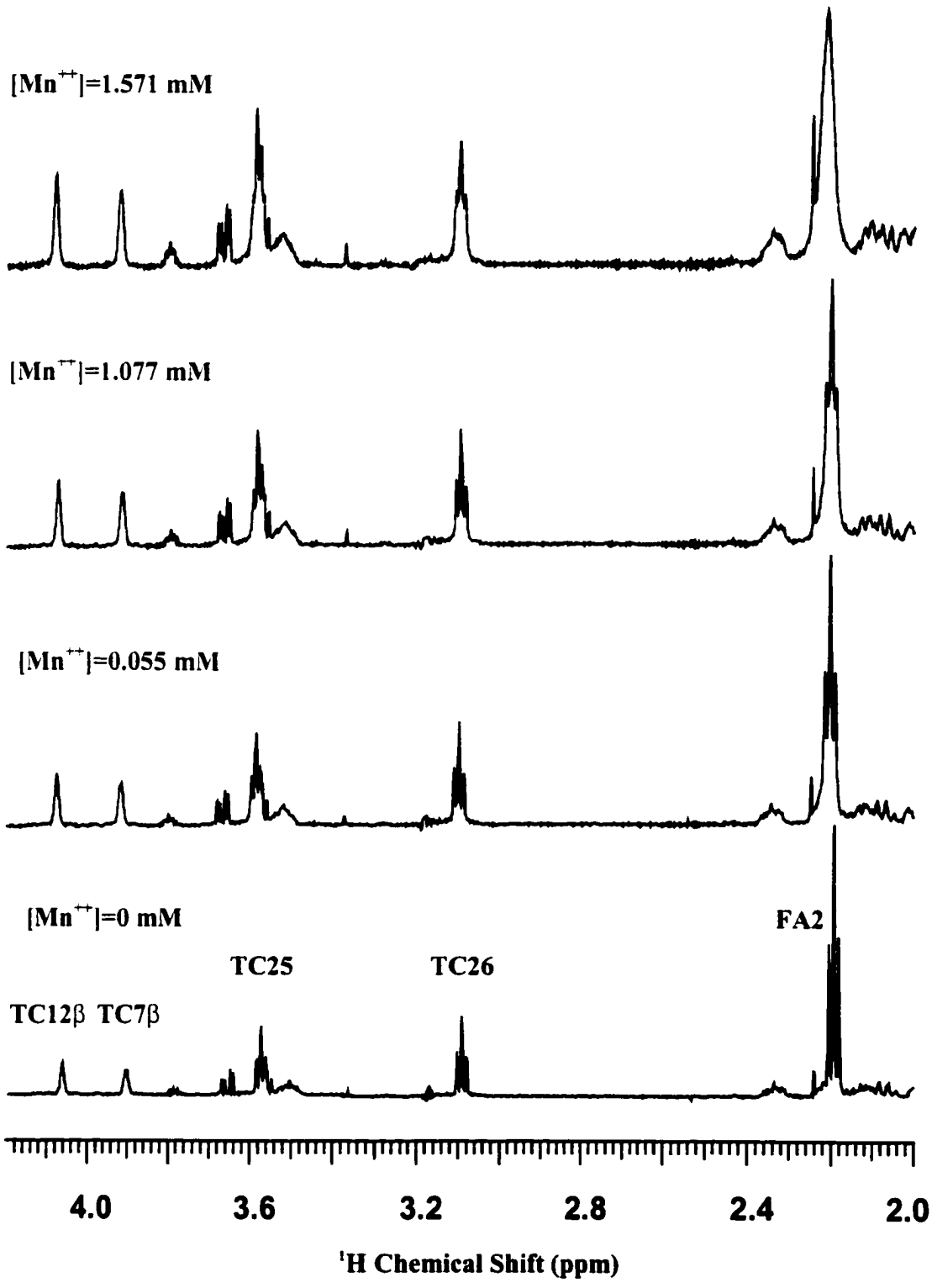

Fig. III-7: (a) QLS results (CONTIN & Cumulant) of 20:1 fat digestive model mixture

(b) QLS results (CONTIN & Cumulant) of 10:1 fat digestive model mixture

(a)

Percent	Lower	Upper
By Inten.	43	57
By Weight	100	0
By Number	100	0

Mean = 64nm
Var. = 0.445
Skew = -.484
RMS = 1.95E-02

Digestion 20:1

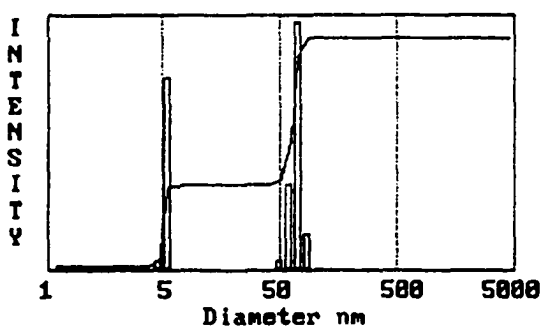

d/nm	G(d)	C(d)
7	4	2
8	77	31
8	4	33
12	0	33
14	0	33
17	0	33
20	0	33
24	0	33
28	0	33
34	0	33
40	0	33
48	0	33
57	0	33
69	4	34
82	34	47
97	100	86
116	14	92
dust	22	100

***** Cumulant Analysis *****

Digestion 20:1

	Amp	Diam(nm)	Gamma	Poly	Skew	Kurtosis	RMS Error
Linear	1.344	42.5	4481.3				4.460E-02
Quadratic	1.360	28.9	6468.5	0.282			5.550E-02
Cubic	1.371	21.4	8742.5	0.525	0.31		3.230E-02
Quartic	1.379	16.7	11221.5	0.748	0.53	3.12	2.190E-02

(b)

Percent	Lower	Upper
By Inten.	41	59
By Weight	100	0
By Number	100	0

Mean = 81nm
Var. = 0.326
Skew = -.216
RMS = 1.59E-02

Digestion Model 10:1

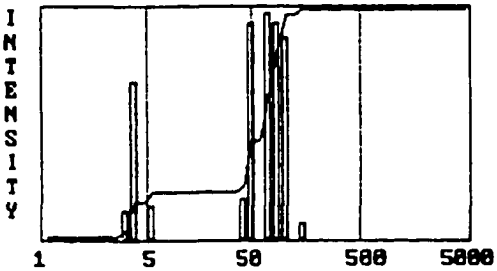

d/nm	G(d)	C(d)
5	13	3
6	70	16
8	16	20
11	0	20
14	0	20
18	0	20
23	0	20
30	0	20
39	0	20
51	19	23
65	95	42
85	100	62
109	95	81
141	90	90
183	0	100
237	0	100
306	0	100
dust	0	100

***** Cumulant Analysis *****

Digestion Model 10:1

	Amp	Diam(nm)	Gamma	Poly	Skew	Kurtosis	RMS Error
Linear	1.223	55.3	5922.4				2.30E-02
Quadratic	1.232	38.2	8564.5	0.415			0.76E-02
Cubic	1.238	29.3	11178.1	0.718	0.44		1.82E-02
Quartic	1.242	23.4	13987.4	0.998	0.69	3.28	0.36E-02

C-2.2 Shape determination in fat digestive model aggregates by QLS

Deduction of micellar shape is another unique application of the QLS technique. An evident problem in determining the shape of digestive aggregates is their two-size distribution. Because fat digestive model mixtures consist of mostly small size aggregates, our interest focuses on the small size fraction. Although the number of large aggregates is very small, their presence has troublesome consequences. It is impossible to accurately isolate the dependence of scattered intensity on the size of the small aggregates, because the QLS signal intensity goes as the sixth power of radius and thus the signal from large aggregates will overwhelm that from small aggregates.

In aqueous micellar systems containing bile salts, it is known that dilution causes some aggregates to break up in order to maintain the intermicellar concentration (IMC) of TC dimers and act as a reservoir of molecules for the growth of the small aggregates (Mazer et al., 1980). Because the number of large aggregates is very small, that population may quickly disappear to produce a single-size distribution of sample amenable to shape analysis. The analysis of QLS dilution measurements by the CONTIN method illustrates this possibility. We obtained an ideal monodisperse distribution of aggregates by very modest dilution with buffer solution. Figure III-8 shows the QLS result for a 20 mg/ml (10:1) fat digestive model mixture prepared by gradually diluting a 30 mg/ml solution.

Fig. III-8: QLS results of a 10:1 fat digestive model mixture diluted to 20 mg/ml

Percent	Lower	Upper
By Inten.	100	0
By Weight	100	0
By Number	100	0

Mean = 7nm
Var. = 0.017
Skew = 0.849
RMS = 1.15E-03

Digestion 10:1; 20mg/ml; 1ml

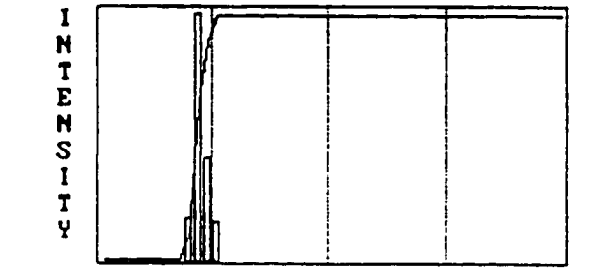

d/nm	G(d)	C(d)
2	0	0
2	0	0
3	0	0
3	0	0
4	0	0
4	0	0
5	10	10
6	100	65
7	42	88
8	17	98
10	0	98
12	0	98
14	0	98
16	0	98
19	0	98
22	0	98
26	0	98
dust	4	100

***** Cumulant Analysis *****

Digestion 10:1; 20mg/ml; 1ml

	Amp	Diam(nm)	Gamma	Poly	Skew	Kurtosis	RMS Error
Linear	1.436	6.8	37306.5				1.300E-03
Quadratic	1.437	6.6	38385.6	0.063			1.090E-03
Cubic	1.436	6.7	37702.3	0.005	0.00		1.010E-03
Quartic	1.436	6.7	37607.5	0.005	0.00	-38.55	1.010E-03

By further diluting the fat digestive model mixture from a total concentration of 20 mg/ml to 10 mg/ml, it was possible to obtain the dependence of scattered intensity as a function of size (R_h). After data treatment as described in Section II-A.3 and Appendix A, the dependence of I/I_{min} (or MP) on R_h was plotted for theoretical sphere, disk, and rod models, comparing them to the measured variation in scattered intensity ratio (I/I_{min}). Figure III-9 shows the comparison of the scattered intensity ratio with theoretical curves for sphere, disk, and rod. The results reveal that the shape of fat digestive model aggregates is best fit to a rod shape. Here the thickness of the disk and the diameter of the rod cylinder are chosen as 5.0 nm since it is assumed as the length of two TC molecules with one shell hydrating water and ~10-15% overestimation by QLS.

Fig. III-9: Shape deduction of a 10:1 fat digestive model aggregate by QLS

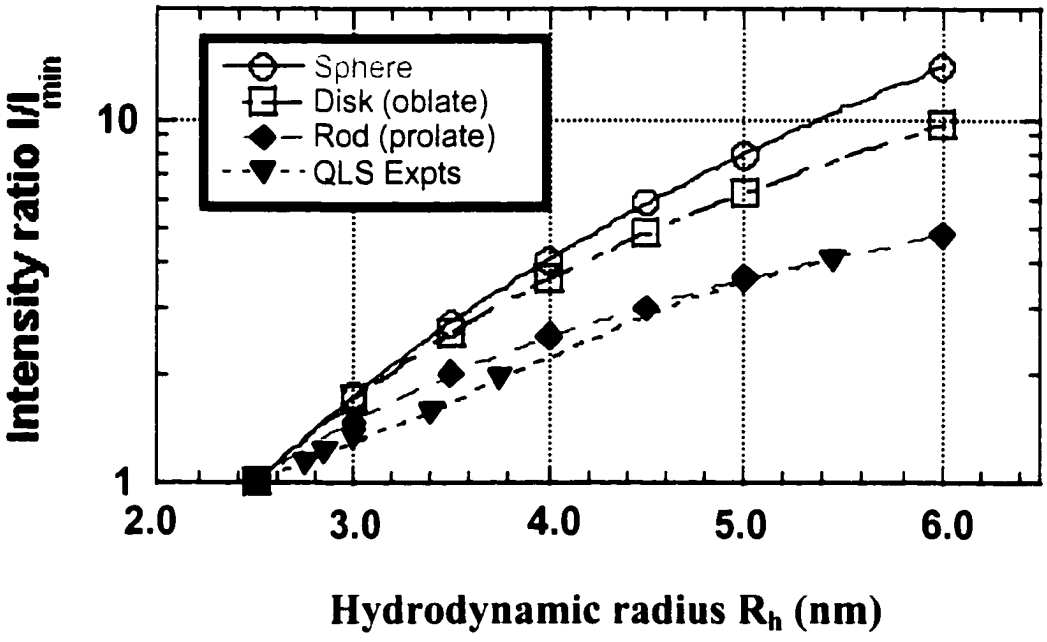

C-2.3 Rod-shaped fat digestive aggregate model

Combining our NMR and QLS experimental results together, we may design a model of fat digestive aggregates with rod shape, as shown in Figure III-10. Dimers (or tetramers) of TC define the radius of the cylinder domain of the rod, which is sealed by two half-spheres with TC dimers as radii. The steroid portion of TC is located inside the rod aggregate; the short side-chain faces outside and retains significant motional freedom. FA and MG molecules span the TC from the second 6-membered steroid ring to the 5-membered ring, with the FA-2 polar end towards the aqueous interface (Fig. III-10). FA molecules are not inserted deeply into the rod aggregate, possibly because its central portion contains tightly packed TC steroid rings. The length of 10 nm in Figure III-10 corresponds to the concentration of 20 mg/ml; and the 30 nm length pertains to the concentration of 10 mg/ml. These lengths of rod are transferred from hydrodynamic radii (sphere) with the diameter of the rod at 5.0 nm.

Fig. III-10: Rod-shape model of fat digestive aggregate based on NMR and QLS results

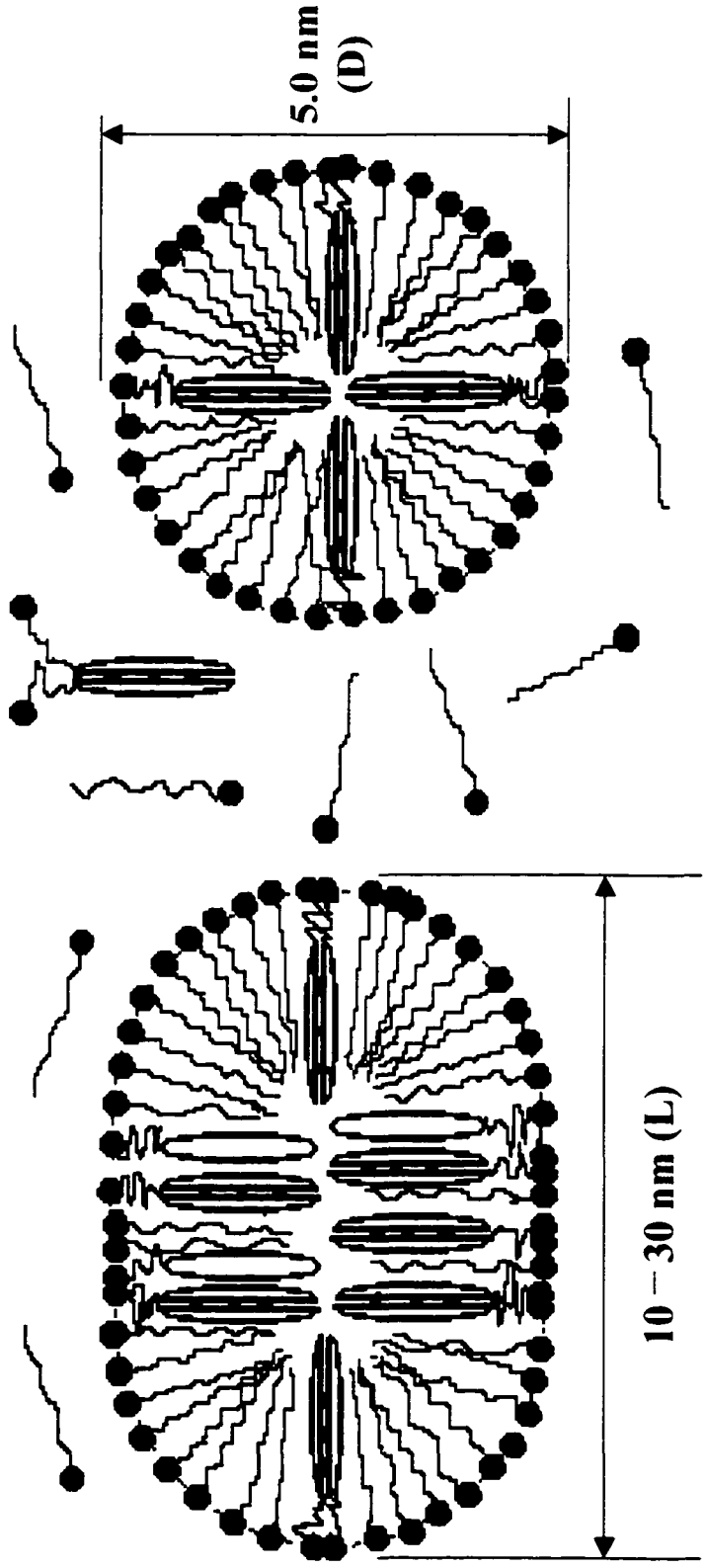

D: Diameter of cylinder portion

L: Length of rod-shaped aggregates

C-3 QLS results for OA/TC (1:1, 1:2) model mixtures for fatty acid transport

Our work described above not only provides information on molecular organization in fat digestive model aggregates, but it also illustrates a successful methology for the study of other mixed biological assemblies. The protocols were repeated for larger oleic acid/TC mixtures of interest in studies of fatty acid transport. Because the size of the aggregates became larger, new complications appeared and required additional experimental adjustments. Nevertheless, our preliminary results show promise for structural studies in these molecular aggregates.

The OA/TC system requires a long time to achieve a stable, homogeneous state; QLS measurements revealed significant variations in scattered intensity over the first 2-hour time period. By monitoring the scattered intensity from a 1:1 OA/TC (10 mM) sample for 3 days, it was demonstrated that the mixture took about 2 days before it equilibrated.

QLS measurements were then performed to find the size and size distribution of the OA/TC aggregates. The QLS results for OA/TC (TC 10 mM) mixtures were analyzed by CONTIN and shown in Fig. III-11, which illustrates that OA/TC aggregates are 5-8 times larger than the small aggregates in the model fat digestive mixtures.

Fig. III-11: (a) CONTIN result of 1:1 OA/TC (10 mM) mixture at 25 °C

(b) CONTIN result of 1:2 OA/TC (10 mM) mixture at 25 °C

Percent	Lower	Upper
By Inten.	25	75
By Weight	75	25
By Number	96	4

Mean = 25nm
Var. = 0.860
Skew = -1.085
RMS = 3.10E-04

OA/TC=1:1(10mM)

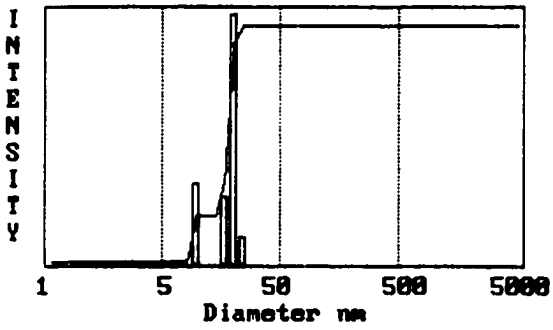

d/nm	G(d)	C(d)
12	0	0
13	33	18
14	0	18
20	0	18
24	27	33
28	100	87
33	12	94
40	0	94
47	0	94
56	0	94
66	0	94
79	0	94
93	0	94
111	0	94
131	0	94
156	0	94
185	0	94
dust	11	100

Percent	Lower	Upper
By Inten.	100	0
By Weight	100	0
By Number	100	0

Mean = 59nm
Var. = 0.233
Skew = 4.965
RMS = 1.81E-04

2(10mM)(after re-shake at 38 C)

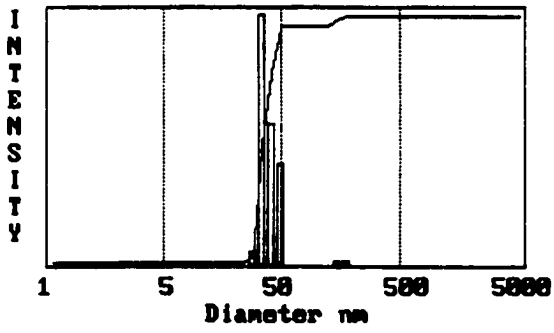

d/nm	G(d)	C(d)
14	0	0
17	0	0
20	0	0
24	0	0
28	0	0
34	0	0
40	7	3
48	100	49
57	57	76
68	41	94
81	0	94
96	0	94
115	0	94
137	0	94
163	0	94
195	3	96
232	3	97
dust	6	100

C-4 NMR results in OA/TC (1:1and 1:2) model mixtures for fatty acid transport

C-4.1 NMR spectral resolution improvement by MAS

The first trials of the NMR experiments failed to yield good NMR spectra. The peaks in the ^{1}H spectrum were broadened, and some expected peaks were not observed even though these experiments were acquired with a 600 MHz instrument. We inferred this result was a consequence of limited motion of the aggregates because of their large size. One way to produce further line narrowing is to run NMR with MAS, as in solid-state NMR. Small sample size (40 μl) and modest spinning speeds (2000 Hz) may be used for aqueous samples with the Nanoprobe. A ^{1}H NMR comparison of 1:1 OA/TC (10 mM) with Z-axis spinning and MAS is shown in Fig. III-12.

C-4.2 ^{1}H peak assignment from 2D COSY and TOCSY spectra

With the use of MAS, the ^{1}H 1D spectrum of the OA/TC mixture (Fig. III-13) could be assigned by 2D COSY and TOCSY experiments (data not shown). All peaks were referenced to TC-18 methyl protons (0.73 ppm). Analysis of the 2D COSY spectrum (data similar to Fig. III-1) proceeded as in the fat digestive model mixture; assignments of weak TC peaks in OA/TC mixtures were also checked against the fat digestive mixtures. The weak COSY cross peaks from TC may be attributed to its low concentration (10 mM, 5.4 mg/ml), and to the fact that MAS at 1900 Hz achieves only

partially averaging of dipolar interactions and leaves significant sidebands in the spectrum.

In theory, magnetization can transfer along the whole methylene chain in TOCSY experiments as long as the protons have no intervening nonprotonated carbon. However, oleic acid cross peaks between double bond protons (9, 10) and C2 and C3 protons were not observed in the TOCSY spectra of either 1:1 mixture (t_m = 50 ms) or 1:2 mixture (t_m = 70 ms). This negative result agrees with prior solution-state NMR of oleic acid.

Fig. III-12: Stacked plot of ^{1}H spectrum of 1:1 OA/TC sample with and without MAS

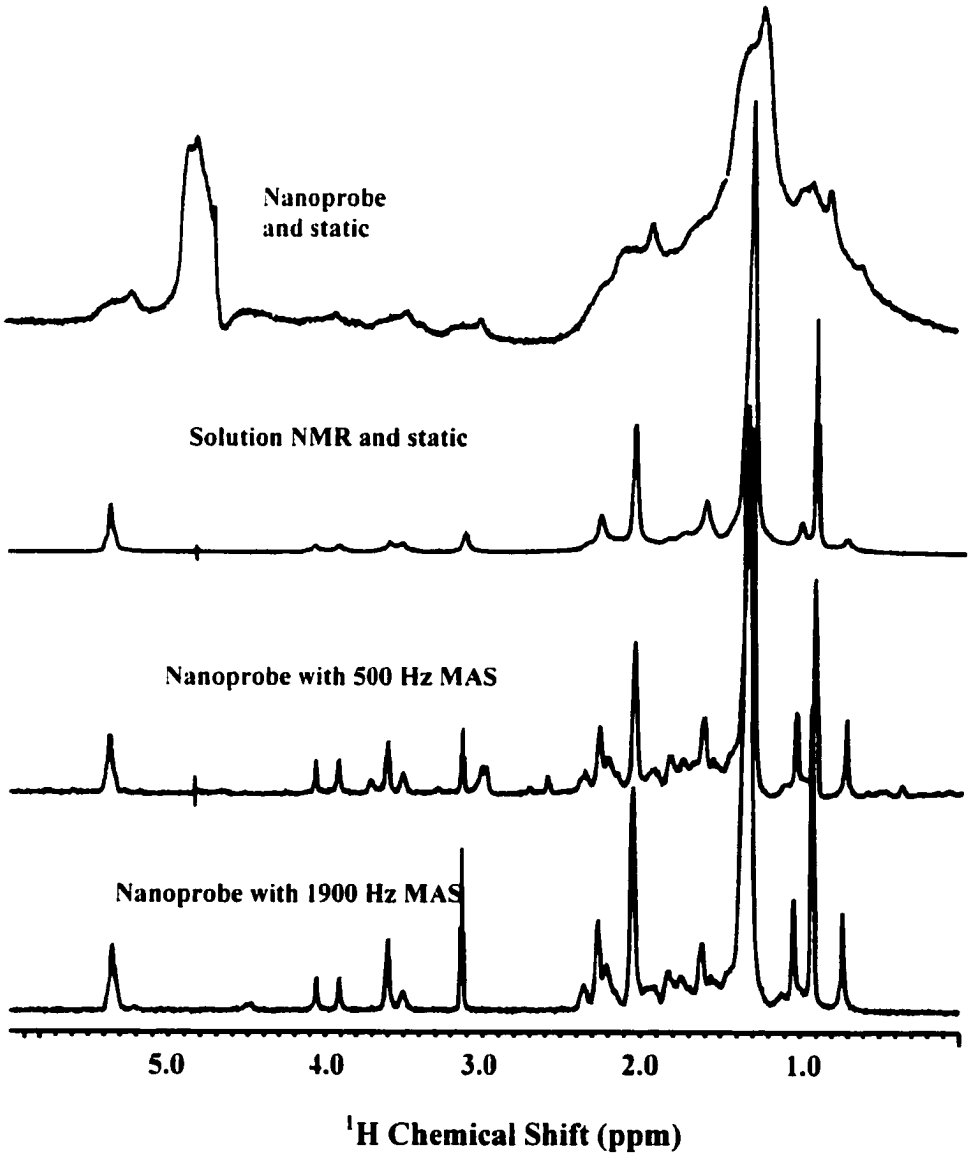

Fig. III-13: Assigned ^{1}H 1D spectrum of OA/TC mixture and molecular structure of oleic acid (OA)

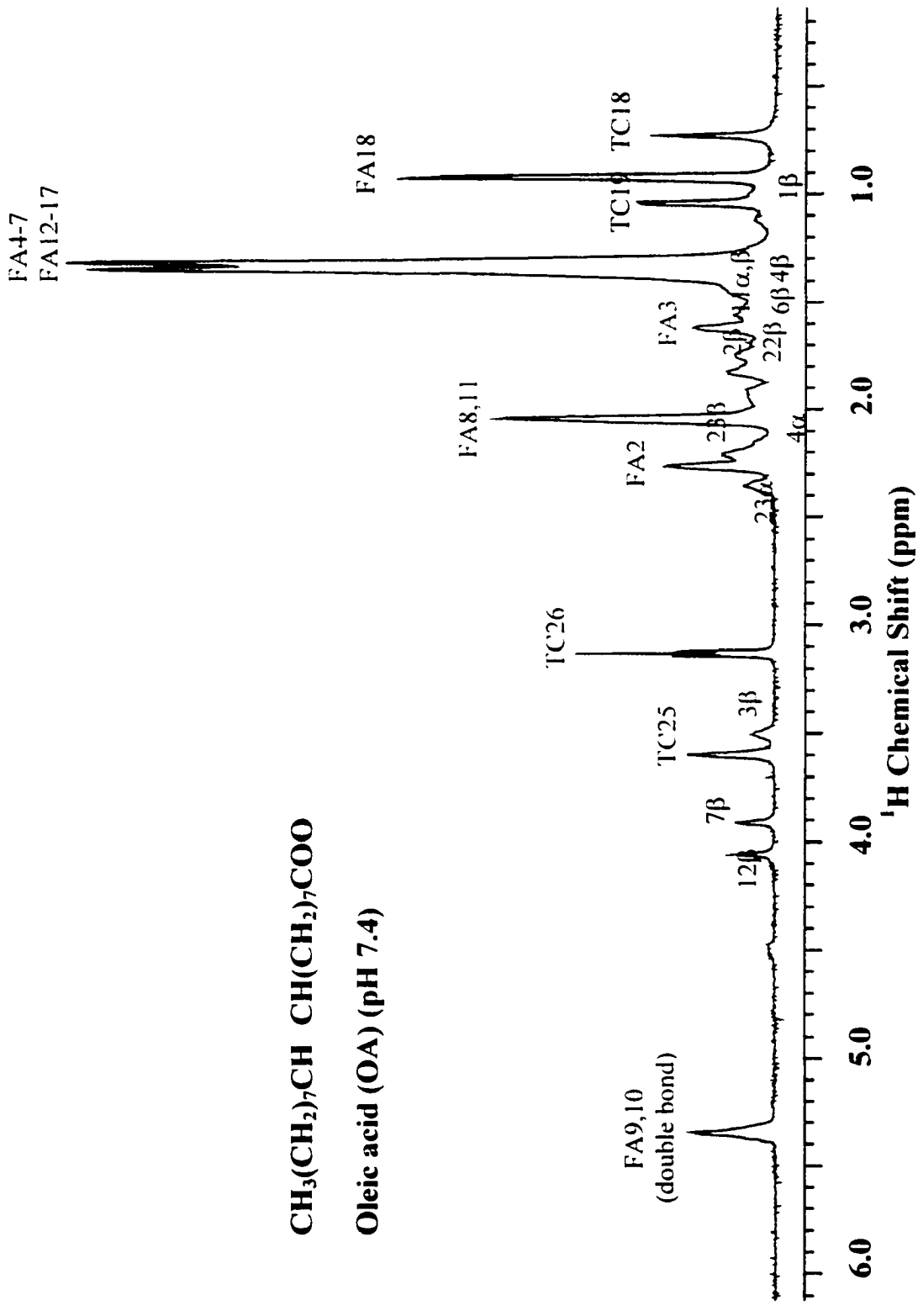

C-4.3 NOE cross peaks in the NOESY spectrum

NOE cross peaks provide important information regarding molecular organization since they indicate the distance between two spins is within 0.5 nm. NOESY spectra of the 1:1 OA/TC mixture shown in Fig. III-14 illustrate the following: there is an NOE cross peak between TC18 and FA18, but no cross peak between TC19 and FA18 (Fig. III-14(a)); TC25 and TC26 exhibit cross peaks only between each other (Fig. III-14(b)); and FA2 has NOE cross peaks with other FA protons, but no NOE cross peaks are found between FA2 and TC (Fig. III-14(c)).

Based on the intermolecular (OA-TC) NOE cross peaks, as well as the size of OA/TC aggregates, a discoid shape is most likely for the OA/TC aggregates. A spherical shape is preferred because the hydrodynamic radius of OA/TC aggregates is 25-45 nm. In contrast to the model digestive mixtures, a rod shape is also unlikely since it would require rod aggregates to be very long. A discoid shape is most likely to fit the data from QLS and NOESY. FA molecules may arrange themselves in the middle of disk with polar end (FA2) facing water media and hydrophobic chains overlapping together; TC molecules form a shell around the disk with hydroxyls facing outward to prevent FA hydrophobic chains from exposure to water. The side chains of TC and polar end of FA still have motional freedom in the discoid aggregates so that NOE cross peaks between TC side chains or FA2 and TC steroid are not observed in the NOESY

spectrum. Possible experiments to conform this preliminary model are described in Section D.

Fig. III-14: 2D NOESY spectra of an OA/TC (1:1) mixture (t_m = 200 ms)

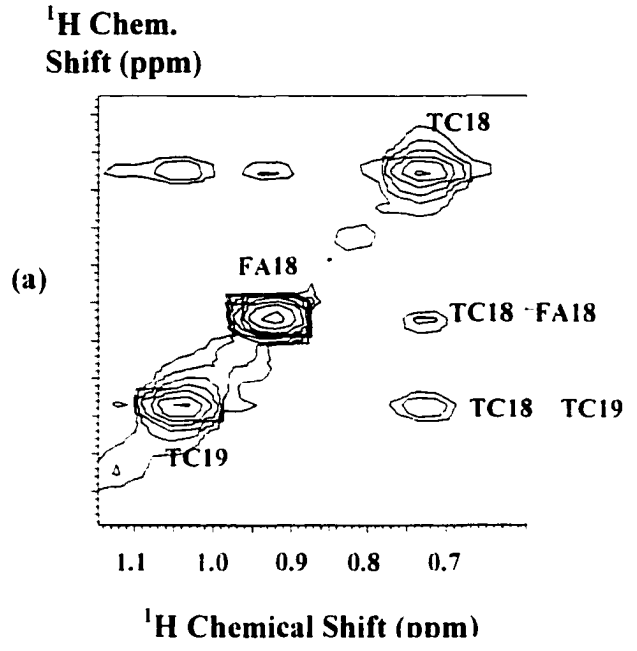

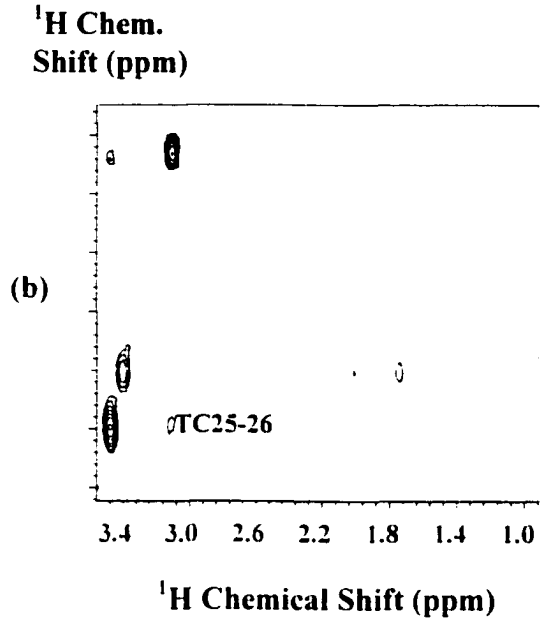

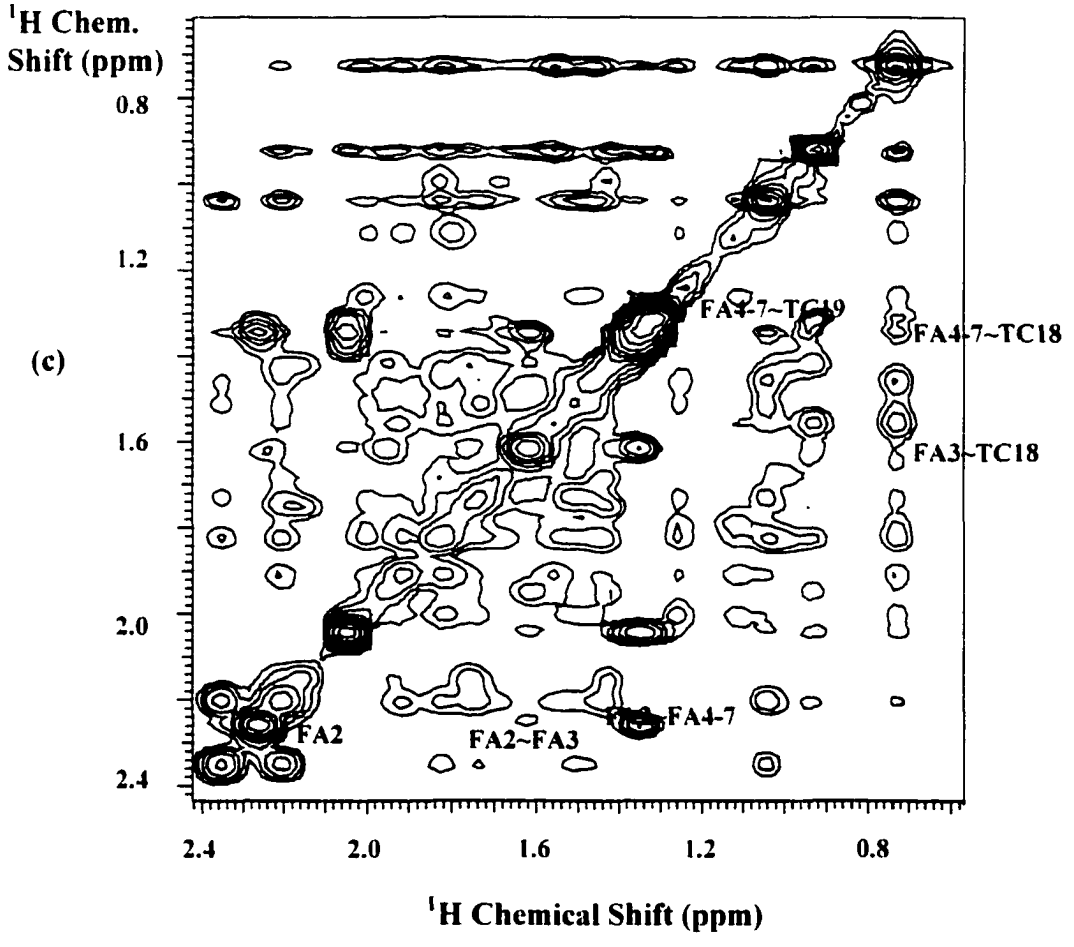

D Discussion

D-1 Fat digestive model mixtures

D-1.1 Structural information from NMR data

Several NMR studies of fat digestive model mixtures from our laboratory provided useful molecular information preceding this work. All peaks of the ^{1}H spectrum were assigned based on 2D DQF-COSY, TOCSY, and ^{1}H-^{13}C HMQC experiments (Longo, 1992; Chen, 1996). The ^{13}C spin-lattice T_1 relaxation times and $^{13}C\{^{1}H\}$ NOEs suggested that the C_8 fatty digestive mixtures form three-component (TC-FA-MG) mixed micellar aggregates (Wang, 1992, b). Selected NOE cross peaks in NOESY spectra were used to delineate intermolecular (TC-TC, TC-FA) proton-proton proximities. Mn^{2+} titrations revealed the surface accessibility of polar groups in the aggregates. In the first portion of my studies, a model mixture with FA:MG of 10:1 was found to have significant structural similarity with the 20:1 aggregates, judging from ^{1}H chemical shift assignments, NOE cross peaks, and Mn^{2+} titrations.

However, these NMR data are not sufficient to design a complete organizational model of fat digestive aggregates. In my study, the main goal was to developing such a model that augments NMR data with new size and shape information from QLS measurements.

D-1.2 Does the structure of fat digestive aggregates change during dilution?

The dilution of the fat digestive sample provides us two very valuable results. First, the gradual dilution process produces a one-size particle distribution, presumably because a few of the large aggregates are broken up (In Section II-C, we already explained why a narrow monodisperse distribution is essential to shape analysis by QLS). Secondly, continuous dilution provides a way to measure the relationship between scattered intensity and scatterer size, in cases where changing the temperature or FA/TC molar ratio might risk large changes in supramolecular organization.

Is the structure of fat digestive aggregates maintained as the mixture is diluted? This premise must be tested before the dilution series of QLS measurements is accepted. The simplest test uses Mn^{2+} titration of the ^{1}H NMR spectrum, where any significant change in the aggregate structure should produce an altered pattern of peak broadening. No such changes were found when the concentration was changed from 20mg/ml to 10mg/ml (data not shown).

D-1.3 Is the rod model consistent with the stoichiometry of the model digestive mixtures?

Based on the experimental results of NMR and QLS measurements, we successfully designed a rod-shape fat digestive aggregate model. Although the model

nicely explains all experimental data, it should also be tested for consistency with the required molar ratio of (FA+MG)/TC, which is 4 in our samples. In other words, is there sufficient empty space among TC dimers to accommodate four times as many fatty acid and monoglyceride molecules as TC molecules?

To answer this question, the rod shape model was further classified into four shells from inside to outside. The first shell is left empty to account for molecular repulsive forces that occur if the molecules approach too closely. The second shell only contains the first 6-membered steroid ring of TC, the third shell contains the remaining steroid rings and the fatty acids, and the fourth shell contains only the TC side chains. The thickness of each shell can be determined based on the molecular lengths of TC and FA. The second shell includes the size of the first 6-membered ring. The third shell should match the length of the FA molecules. The fourth shell can be neglected here since its size does not depend on the number of TC or FA. The four-shell structure is diagrammed in Fig. III-15.

Fig. III-15: Four-shell diagram for rodlike fat digestive aggregate model

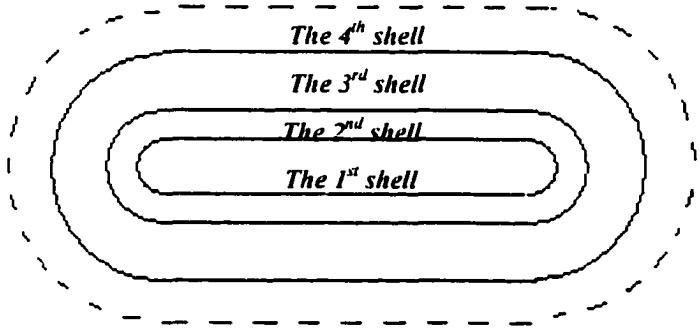

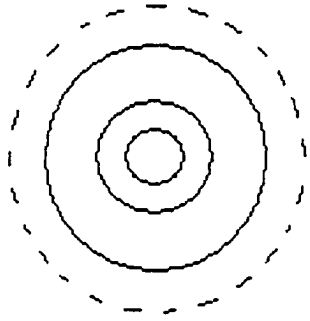

steroid rings in the third shell

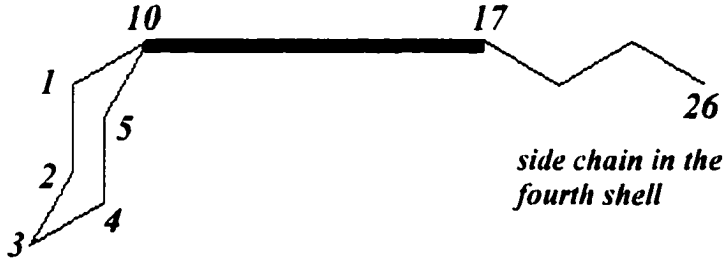

The first 6-membered ring
in the second shell

In this model, the volume of the second shell limits the number of TC molecules in the rodlike aggregate, and the volume of the third shell exclusive of the TC steroid domain restricts the number of fatty acid molecules. If the volumes of the second and third shells, the steroid domain of TC, and the fatty acid could be obtained, the numbers of TC and fatty acid and their ratio should be able to be calculated. The MG is counted with FA to simplify the problem.

The molecular dimensions needed for these calculations were derived from the SYBYL program, which uses standard bond lengths and angles from X-ray crystallographic data. After drawing the molecular structures of TC and C_8-FA on the computer, the distance between atoms was measured by picking the required atoms. Typical distances between particular atom pairs of TC and FA are shown in Table III-4.

Table III-3: Distances between two particular atom-pair measured by SYBYL molecular model

Atomic pair	Distance (nm)	Atomic pair	Distance (nm)
C1 - C20	0.811	C10 - C17	0.599
C5 - C20	0.812	H3 - OH	0.178
C3 - C4	0.155	C10 - C17	0.599
O - H (C3)	0.111	H8 - H8 (FA)	0.310
C1 - C8 (FA)	0.850		

It is also known from QLS measurements that the length of one TC molecule is 1.7 nm (Mazer et al., 1976), and the radius of the cylinder is 2.5 nm in the QLS-determined rod model. This is because the radius (2.5 nm) includes the length of one TC molecule (1.7 nm), one shell of hydration water (0.3 nm) (Cantor and Schimmel, 1980), 10-15% overestimation by QLS (0.3 nm), and the excluded volume to avoid intermolecular repulsions. The excluded radius should be 0.2 nm (the distance between two hydrogen atoms is 0.072 nm) within the first shell. We further estimate the second shell as 0.3 nm (two C-C bonds with a certain bond angle), and the third shell as 0.85 nm (the length of an FA molecule). The fourth shell will not considered because it does not affect how many FA molecules can be fit into the rod aggregate. These dimensions are shown in Fig. III-16.

Based on Fig. III-16, we can calculate the number ratio of FA to TC. If the ratio is larger than 4, the rod-shaped model stoichiometrically fits our fat digestive mixtures. First, the volumes of the first 6-membered ring of TC and of FA are estimated using the densities of cyclohexane (0.779 g/ml) and heptane (0.684 g/ml), respectively:

$$V \text{ (6-membered ring)} = 84.16 \times 10^{21}/(0.779 \times 6.02 \times 10^{23}) = 0.179 \text{ (nm)}^3$$

$$V \text{ (FA)} = 100.21 \times 1021/0.684 \times 1023 = 0.243 \text{ (nm)}^3$$

Then, the numbers of TC and FA molecules are calculated as a function of the length of the cylinder portion (L), where the volumes of the other three TC rings are assumed to be three times the 6-membered ring.

Fig. III-16: Size distribution of the four-shell model based on the molecular structure of TC

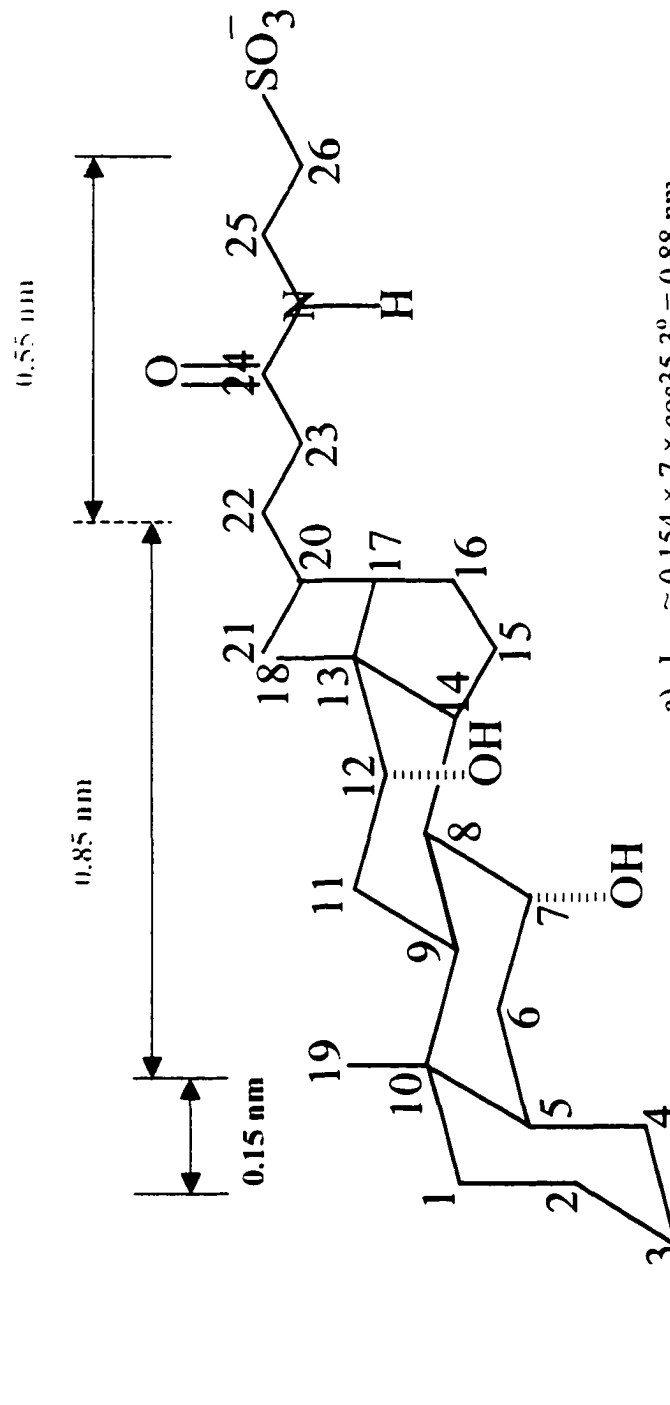

a) $L_{FA} \approx 0.154 \times 7 \times \cos 35.3^{o} = 0.88$ nm

b) $L_{empty\text{-}gap} = 2.5 - 0.3$ (10-15% overestimation by QLS) $- 0.3$ (a shell of hydrating water) $- 1.7$ (TC) $= 0.2$ nm

c) L(TC) = 0.15 + 0.15 + 0.85 + 0.55 = 1.7 nm

$V(\text{second shell}) = \pi L(0.5^2 - 0.2^2) + (4/3)\pi(0.5^3 - 0.2^3) = 0.659L + 0.490\ (\text{nm})^3$

$V(\text{third shell}) = \pi L(1.35^2 - 0.5^2) + (4/3)\pi(1.35^3 - 0.5^3) = 4.938L + 9.777\ (\text{nm})3$

$\#TC = V(\text{second})/0.179$

$\#FA = \{V(\text{third shell}) - \#TC \times V(\text{three rings})\}/0.243$

The results of the above calculations are shown in Table III-4 and a plot of the number ratio of FA to TC appears in Fig. III-17.

Figure III-17 yields an approximate but important conclusion: there is enough empty space among the TC molecules for FA molecules to fit within the aggregates over the whole size range of the QLS dilution experiment. The number ratio of FA to TC is larger than 4 when the length of the cylinder is smaller than 10 nm (total length of rod is 15 nm). When the length is larger than 10 nm, the ratio is slightly smaller than 4. Nevertheless, as we see in NOESY spectrum, negative NOE cross peaks tell us some free FA molecules may be present in systems, so that fat aggregates are still stable when the ratio is a little lower than 4. Since the inside environment of aggregate is highly hydropholic, water factor do not be considered here.

Table III-4: FA/TC number ratio analyses from volume calculation

L (nm)	V_2 $(nm)^3$	#TC	V_3(FA) $(nm)^3$	# FA	#FA/#TC
2.5	2.138	12	15.678	64	5.333
5.0	3.785	21	23.190	95	4.524
10.0	7.080	39	38.214	157	4.026
15.0	10.375	58	52.701	217	3.741
20.0	13.670	76	67.725	279	3.671

Fig. III-17: Dependence of FA/TC on length of the cylindrical portion in the rodlike model

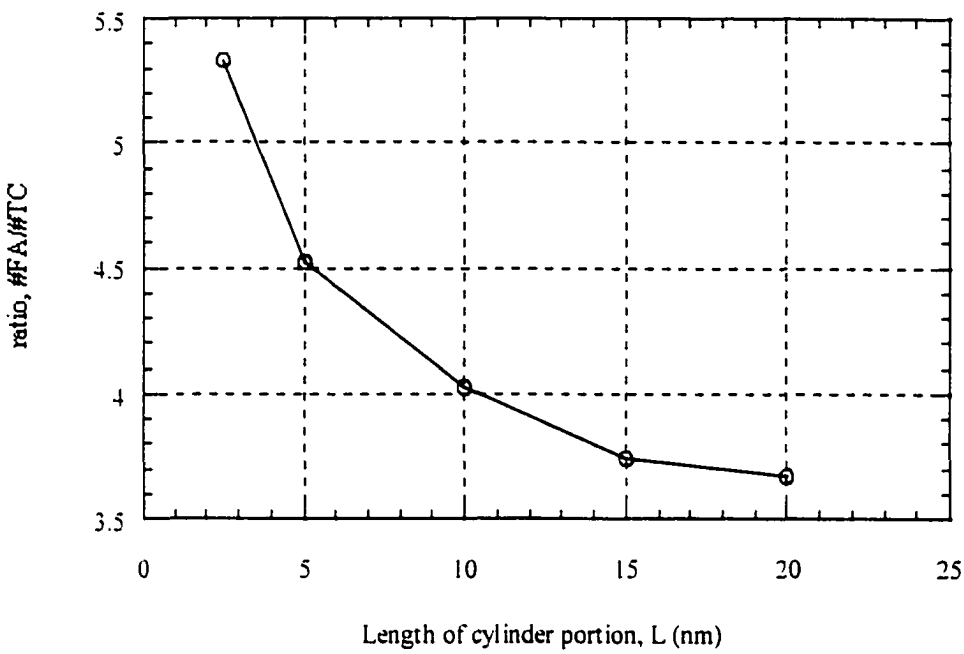

D-1.4 Conclusions for model fat digestive mixtures

In this study of molecular organization in fat digestive model mixtures, a sequence of NMR experiments was applied to a new FA/MG=10:1 mixture. From the assignment of the ^{1}H 1D NMR spectrum by 2D COSY and TOCSY, NOE crosspeak analyses in NOESY and ROESY spectra, and Mn^{2+} titrations of ^{1}H spectra, the NMR data were found to be in close agreement with the results obtained for the analogous FA/MG=20:1 mixture by Z. Chen (Chen, 1996).

In the absence of information about size, size distribution, and shape of fat digestive aggregates, it is not possible to design a molecular model of the fat aggregate. The QLS results in the present work illustrated that both 20:1 and 10:1 fat digestive model mixtures have two-size distributions. The small aggregates are dominant in total aggregate number so they probably exert the main effect in fat digestion and are of greatest interest. Although the large aggregates are rare in number, they show a significant contribution to scattered light intensity.

The presence of large aggregates compromises the determination of shape for the predominant small particles. We successfully overcame the two-size distribution problem by gradual dilution the sample from 30 mg/ml to the required 20 mg/ml, rather than directly preparing a 20 mg/ml sample. In this way, we produced a monodisperse sample of micellar aggregates suitable for shape deduction by QLS. By further dilution

of the concentration to 10 mg/ml, the digestive aggregates maintained a one-size distribution and allowed measurement of the dependence of scattered intensity on the hydrodynamic radius R_h. After numerous QLS experiments and analyses, we were able to conclude that the small model digestive aggregates assume a rod-like shape.

Based on consideration of both NMR and QLS data, we designed the rod-shaped fat digestive aggregate model, as described in Figure III-10. In addition to consistency with all NMR results, it was possible to use known molecular geometries to demonstrate that there was an adequate empty space among the TC dimers to accept all FA and MG molecules in the rod model. Thus, the rodlike model provides a plausible description of aggregate organization in mixed micelles that model the late stage of fat digestion.

D-2 Fatty acid transport model mixtures

D-2.1 Magic-angle spinning improves NMR spectral resolution of large-size fatty acid transport (OA/TC) aggregates

It has been demonstrated that a combined NMR and QLS strategy works effectively to determine a three-dimensional micellar model for fat digestive model mixtures. However, the same protocol was not as successful when applied to fatty acid

(oleic acid) transport model mixtures, in which NMR spectral resolution and peak intensities of were diminished due to line broadening.

Figure III-11 (Section C-3) showed that the size of fatty acid (oleic acid)/TC aggregates was 5-8 times larger than that of fat digestive model aggregates. This is easily understood because oleic acid is longer and more hydrophobic than octanoic acid. As a consequence of aggregate growth, both significant increases in dipolar interactions and limited overall motion resulted in NMR peak broadening and 'loss' of signal into the base line. Since the situation was similar to that encountered in solid-state NMR spectroscopy, magic angle spinning (MAS) was likely to be the most effective technique to narrow the NMR peaks.

After introducing MAS, NMR experiments were conducted as for the fat digestive model mixtures. For example, MAS (1900 Hz) gradient DQF-COSY and TOCSY spectra (data not shown) provided enough data to assign most of the ^{1}H peaks (Fig. III-13). However, due to limitations on the amount of sample (~40 μL) and the maximum MAS spinning speed (<2500 Hz) of the Nano-MAS probe, it still proved difficult to obtain high-quality NMR spectra and to run a series of Mn^{2+} titration experiments.

D-2.2 Preliminary discoid model for OA/TC fatty acid transport aggregates

To design a three-dimensional model for mixed aggregates, information about the size, size distribution, and shape (from QLS), intermolecular organization (from NOE analyses), and polar group orientation (Mn^{2+} titration) have to be determined. Although the shape and water accessibility were not determined in the present study, a preliminary discoid model could be proposed for OA/TC aggregates based on results obtained for the size of OA/TC aggregates (R_h: 14-28 nm) and intermolecular NOE cross peaks.

First, if OA/TC aggregates adopted a rod-like shape, the length of these aggregates would be as long as 100-250 nm with a radius of 2.5 nm (approximate length of one OA molecule), in order to conform to the size derived from QLS measurements. The possibility of a rod-like model is considered unlikely, because it is hard to imagine stable aggregates that are so long and thin. Secondly, a sphere is not preferred since several OA molecules would need to be arranged in a line to reach the radius (25-50 nm). Discoid aggregates may offer the best model to explain both size results from QLS and intermolecular NOE cross peaks from the NOESY spectrum. To confirm this model and distinguish between spherical and discoid shapes, the Mn^{2+} titration experiment is the most direct and rapid method, because line broadening of the protons on the same carbon as the hydroxyl groups is expected for discoid aggregates.

Several interesting NOE cross peaks (Fig. III-14) help to define the possible molecular organization in OA/TC aggregates and support a preliminary discoid model:

(1) TC25 and 26 protons show only NOE cross peaks between themselves, which suggests that the side chains of the TC molecules are not packed inside the OA/TC aggregates. Otherwise, the side chains would exhibit NOE cross peaks with the steroid rings of TC or with OA molecules. (2) the FA2 proton has FA-FA NOE cross peaks with FA3 and FA4-7 protons, but it has no FA-TC NOE cross peaks. This may indicate that FA2 is located at the interface of the OA/TC aggregates, so that the polar end retains significant motion freedom. (3) FA18 displays an NOE cross peak with TC18, but not with TC19, indicating that FA18 is closer to TC18 than TC19. The hydrophobic portions of OA molecules may be protected by a rim of TC molecules with their hydrophilic sides facing toward the water media. Because the TC molecule is shorter than the OA molecule, OA molecules may overlap ~70-80% in the bilayer domain to fit the length of TC. The absence of an NOE cross peak between FA2 and FA18 can be explained by both the protruding FA2 and its motional freedom. The preliminary discoid model is shown in Fig. III-18.

Fig. III-18: Preliminary discoid model of OA/TC fatty acid transport aggregates

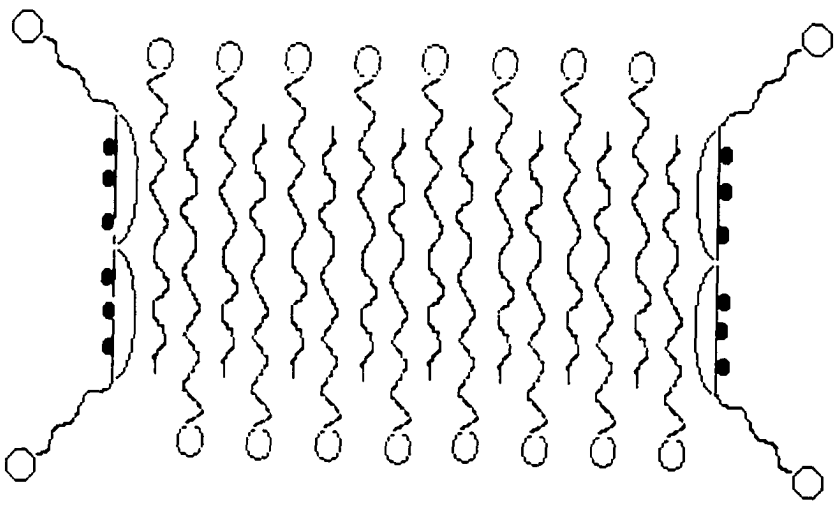

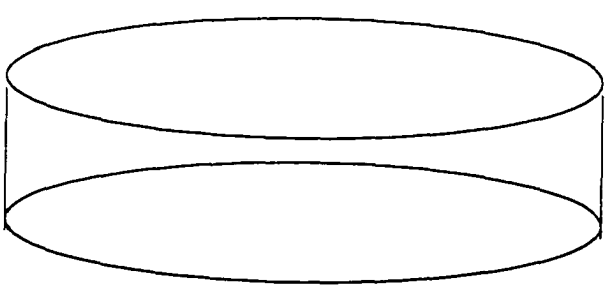

Chapter IV QLS Study of Phospholipid (DMPC/DHPC) Bicelles

A Introduction

X-ray crystallography and NMR spectroscopy are two major molecular structural analysis techniques for the study of biological macromolecules, such as proteins and peptides. X-ray crystallography can provide a very precise view of the high-resolution molecular arrangement for very large proteins, but it is often difficult to prepare a good crystalline sample for X-ray measurement. This method also misses important dynamic information. NMR can directly determine the structures of proteins in aqueous solution, whereas it is limited to relatively small water-soluble proteins. As molecular size increases the NMR spectrum becomes overlapped and rapid signal decay attenuates the structurally useful spectral features. Recently, new techniques, such as NMR in liquid-crystalline media containing 1,2-dimyristoyl-*sn*-glycero-3-phosphocholine (DMPC) and 1,2-dihexanoyl-*sn*-glycero-3-phosphocholine (DHPC) bicelles (Tjandra and Bax, 1997; Vold et al., 1997) and transverse relaxation-optimized spectroscopy (TROSY) (Wuthrich, 1997) have been developed. These approaches yield additional distance constraints and select a narrower component of the peak, respectively, giving NMR more ability to deal with complex problems in structural biology.

Membrane proteins have proven especially challenging for structural studies, since they often fail to crystallize or dissolve in aqueous media. The ability of proteins to dissolve in aqueous solution with detergent micelles (sodium dodecyl sulfate (SDS) or dodecyl phosphocholine (DPC)) provides a well-characterized model system for NMR studies of protein structure. Since proteins associated with micelles undergo effectively isotropic reorientation in solution, multimensional solution NMR experiments are feasible on these samples. However, in order to form uniform micelles and fully solubilize the protein, the detergent concentration is typically required to be 20-100 times its critical micellar concentration (CMC). Such a high concentration of detergent produces a large aggregate with broad NMR spectral features and may also denature the protein (McDonnell and Opella, 1993).

An alternative membrane-mimetic medium is based on phospholipid mixtures. It is well known that the structures of phospholipid aggregates in aqueous solution depend critically on the length of the phospholipid acyl chains. Short-chain PC's (6 or 8) form stable aqueous micellar structures, for example, while long-chain PC's (>12) constitute aqueous multilamellar structures. Roberts and coworkers first found that another unique class of unilamellar vesicles formed spontaneously upon mixing long-chain (multilamellar, liquid crystalline) phospholipids with a small amount of short-chain (micellar) phospholipid when the temperature was higher than the T_m of the long-chain PC (Gabriel and Roberts, 1984). The structures of liquid-crystalline PC aggregates are controlled by the molar ratio of short-chain PC to long-chain PC. Based on the phase

diagram published by Roberts, the structures of binary PC aggregates are summarized in Table V-1 (Bian and Roberts, 1990).

One of the possible applications of these binary PC devices was to improve the attack of water-soluble enzymes on hydrophobic long-chain PC membranes. A few years ago, Bax et al. found an interesting NMR application of binary PC bicelles (bilayered micelles) made from dilute solutions of 1,2-dimyristoyl-*sn*-glycero-3-phosphocholine (DMPC) and 1,2-dihexanoyl-*sn*-glycero-3-phosphocholine (DHPC). For a protein sample in binary PC liquid crystalline media, the small preferential orientation of the PC aggregates in a magnetic field will gently align the protein molecules and yield distance information that can improve the quality of protein structures derived from NMR spectra (Tjandra and Bax, 1997).

Table V-1: Structures of diheptanoyl-PC/dipalmitoyl-PC aggregates at different molar ratios

Molar ratio of PCs (short-chain/long-chain)	Structure of PC aggregates
<0.1	Multibilayer
0.1-0.45	Simple bilayer
0.45-0.6	Coexisting simple and mixed bilayers
>0.6	Mixed bilayer

In order to achieve a full understanding of the structure of DMPC/DHPC bicelles, it has been of particular interest to determine the shape and possible bilayer arrangement of the aggregates. Roberts inferred that dipalmitoyl-PC/diheptanoyl-PC particles were flattened and closed to form an oblate shape (Bian and Boberts, 1990). She discarded the possibility of a classic rod shape because the aggregates were nonlytic to human erythrocytes. She also argued that the aggregates should not have a spherical shape because it was almost impossible for dipalmitoyl-PC to form and maintain such a small sphere (R_h: ~4.5 nm). Sanders (Sanders and Schwonek, 1992) reported that DMPC/DHPC mixed aggregates formed a well-oriented discotic nematic bicelle based on ^{31}P NMR measurements during the titration of DMPC with DHPC. In this work, the progressive line shape changes of the DMPC were characterized as a function of the amount of DHPC: from the L_α phase bilayer line shape of pure DMPC, to the downfield shift and decrease in the ^{31}P peak intensity of the DMPC, until the convergence of the ^{31}P peak of the DMPC to the isotropic chemical shift of the micellar DHPC. It was concluded that the DMPC/DHPC bicelle was a disk-shaped aggregate with bilayer DMPC in the planar center and the DHPC primarily sequestered along the rim to shield the hydrophobic chains of DMPC but also mixed with the DMPC domain.

Vold and Prosser (Vold et al., 1996) used ^2H quadrupole-echo experiments to measure the ratio of quadrupolar splittings (Δ_L/Δ_S) for the α-deuterons (the ester α-methylene groups), where Δ_L is the observed quadrupolar splitting of the DMPC bilayer "plateau region" domain (17.3 $\pm$ 0.1 kHz) and Δ_S is the quadrupolar splitting of the

DHPC rim domain (3.8 ± 0.1 kHz). The results revealed that DMPC/DHPC bicelles were macroscopically aligned in the magnetic field when the DMPC/DHPC molar ratio q>2.5. They proposed that DMPC and DHPC were almost completely separated into two domains. The rim of the discoid contains only DHPC and the bilayer plane of the discoid only DMPC, because the Δ_S/Δ_L data (0.22 ± 0.01) measured from bicelles with q=3.2 agreed closely with theoretical predictions (0.236). A simple mathematical disk-like model was proposed to describe the dependence of bicellar size on DMPC/DHPC molar ratio q, subject to two assumptions: the polar end-groups for DMPC and DHPC have the same surface area, and that these two compounds remain in completely separate domains. The dependence of the size of bicelles on the molar ratio of DMPC/DHPC can be defined from the model as follows:

$$R = (1/2)rq[\pi + (\pi^2 + 8/q)^{1/2}] \qquad \text{(Eq. IV-1)}$$

where R is the radius of the DMPC domain, r is the radius of DHPC rim, and q is the molar ratio DMPC/DHPC. The consensus model based on the considerations above is shown in Figure IV-1.

Fig. IV-1: Discoid model of DMPC/DHPC bicellar aggregates (Vold et al., 1997; Zemd et al., 1999)

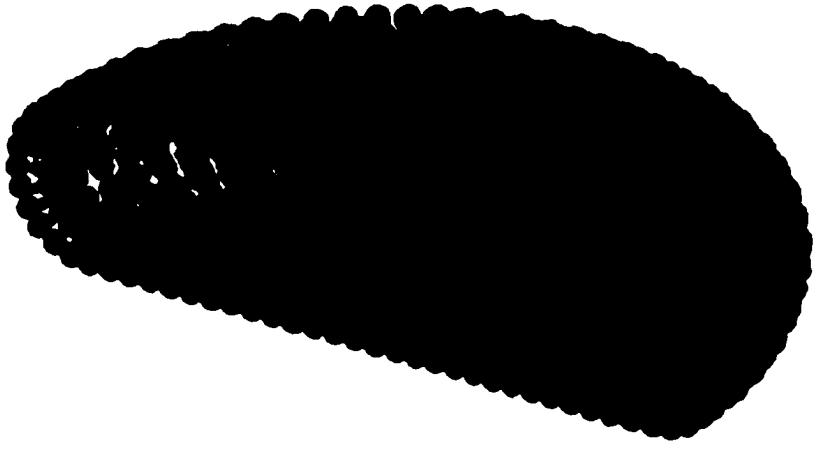

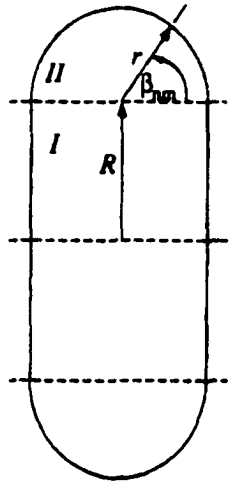

The use of phospholipid bicelles was recently extended to isotropic solutions with DMPC/DHPC molar ratio q as low as 0.5 and a total lipid concentration of 15% (w/v), in which small peptides adopted a helical conformation and well-resolved NMR spectra were obtained (Vold et al., 1997). The implication of this work was that bicelles rich in short-chain lipid could serve as membrane-mimetic media without adopting a liquid-crystalline phase, thus avoiding line broadening of peptide or protein solutes and permitting high-resolution NMR structure determination. Nevertheless, the morphology of these aggregates has not been established, and thus their suitability as a membrane-mimetic medium has not been evaluated critically.

B Quasielastic Light Scattering (QLS) Experiments

B-1 Materials and sample preparation

1,2-Dimyristoyl-*sn*-glycero-3-phosphocholine (DMPC) and 1,2-Dicaproyl-*sn*-glycero-3-phosphocholine (DHPC) were purchased from Avanti Polar Lipids, Inc. (Alabaster, Alabama, USA) and used as received.

25 mg/ml (2.5% w/v) DMPC/DHPC mixtures

16 mg of DHPC was dissolved in 1ml of deionized water filtered twice with 0.2 μ syringe filters (best water) . The solution was kept in the refrigerator (-4 °C) at least

overnight. 9 mg of dry DMPC powder was added into the DHPC solution to produce a mixture with q=0.376 and overall 2.5% (w/v) as described previously (Vold et al., 1997). The solution was placed in a 40°C warm-water bath for at least 1 hour. The powdered DMPC was solubilized and the solution became optically clear. Then the solution was placed in a 0°C ice-water bath for at least another 1 hour. The process was repeated twice to ensure that the solution was homogeneous.

After the first set of QLS measurements, 5 mg of DMPC powder and 0.2 ml of water were added to the original mixture to change the DMPC/DHPC molar ratio but maintain a constant mass concentration (2.5% w/v). The process above was repeated to dissolve and homogenize the mixtures. As the DMPC/DHPC ratio was increased, the solution at 40°C became light milky. It reverted to a clear solution at 4°C and room temperature. The DMPC/DHPC molar ratio was increased as high as 2.05. Higher molar ratios were avoided because the product of particle diameter and viscosity approached the limit for reliable size determinations. For our BI-9000 laser scattering instrument, the limitation is that the product of particle hydrodynamic diameter (D in μ) and the viscosity (η in cP) should not exceed 2-5. Based on information supplied by the Vold group, the viscosity of bicelles at q=2 and 10°C is estimated to be higher than 50 cP. Since the diameter of bicelles under these conditions exceeds 0.02 μ (i.e. 20 nm), the product of ηD is larger than 1.0.

In order to generate additional low-q bicellar mixtures, 20 mg of DHPC was dissolved in 0.8 ml of water. The solution was put in the refrigerator (~4°C) for 2 days. After QLS measurements on the DHPC micellar solution, 5 mg of DMPC and 0.2 ml of water were added to the DHPC solution. After temperature cycling as detailed above and QLS measurement, the DMPC/DHPC molar ratio q was changed by adding another 2.5 mg of DMPC and 0.1 ml of water to the original solution.

100 mg/ml (10.0% w/v) DMPC/DHPC mixtures

Because the total lipid concentration of bicellar solutions for many NMR applications is in the range of 5-40% (w/v) (50 mg/ml - 400 mg/ml), the 25 mg/ml solutions might be too dilute to represent practical membrane-mimetic mixtures. In order to make our QLS results commensurate with other spectroscopic studies, 70 mg of DHPC was dissolved in 1 ml of filtered deionized water. The solution was placed in the refrigerator (~4°C) overnight. 30 mg of DMPC powder was added to the DHPC solution (10.0% w/v). To change the DMPC/DHPC ratio, 10 mg (or 20 mg) of DMPC and 0.1 ml (or 0.2 ml) of water were added into the original solution. The other steps were the same as those described for the 25 mg/ml samples.

B-2 QLS Experimental Results

The DMPC/DHPC bicellar mixtures display anomalous increases in viscosity at high temperature (data supplied by the Vold group). QLS measurements were performed at 10°C and 15°C to avoid significant deviation of the viscosity of the bicellar solution from water, because the viscosity of the solvent must be used in the Stokes-Einstein equation (Eq. II-5) that converts the diffusion coefficient of scatterers to hydrodynamic radii. Since the viscosity of solvent and the hydrodynamic radius have an inverse relationship in the Stokes-Einstein equation, assuming a value of viscosity that is too low will result in an overestimation in size.

All QLS measurements were performed under common conditions as described for prior QLS experiments on polystyrene standards (Chapter II). The first delay time was set at about one tenth of the smallest size, and the last delay time was set about ten times the largest size obtained in the QLS measurements, in order to accurately sample the autocorrelation function of scattered light intensity. The duration time of each measurement was chosen in the range of 2-5 minutes. The incident intensity was 40 mW for the 25 mg/ml samples and 50 mW for the 100 mg/ml samples. The wavelength of the incident laser light was 488 nm.

Size and Size Distribution

The QLS measurements were repeated five times at each DMPC/DHPC molar ratio and temperature, unless stated otherwise. The DMPC/DHPC mixtures showed a monodisperse size distribution, which was analyzed by the CONTIN algorithm and illustrated in Figure IV-2. The CONTIN method is considered to be the best existing method to analyze size distribution (Chu, 1991). However, because the CONTIN program installed in the BI-9000 instrument does not display size precisely enough to generate a valid curve of I/C vs. R_h, the Cumulant Method was used for size and shape calculations. The size obtained from the 3rd Cumulant was in good agreement with that from CONTIN.

As expected, the size of DMPC/DHPC bicelles gradually increases as more DMPC is added to the bicellar solutions. The changes in hydrodynamic radius of bicelles as a function of DMPC/DHPC molar ratio q at 10°C are shown in Fig. IV-3(a) (25 mg/ml (2.5% w/v) mixtures) and Fig. IV-3(b) (100 mg/ml (10% w/v) mixtures). The consistency of separate size determinations is reflected in the small error bars of Figure IV-3(a), indicating the homogeneity and stability of our bicellar samples and the good quality of the QLS measurements. A comparison of the bicelle size predicted by the Vold theoretical model (Eq. IV-1) and found by QLS experiments is made in Section C-3.

Fig. IV-2: (a) Size and size distribution of DMPC/DHPC (q=0.376) bicelles at 25 mg/ml and 10°C (data analyzed with the CONTIN program)

(b) Size and size distribution of DMPC/DHPC (q=0.585) bicelles at 100 mg/ml and 10°C (data calculated with the CONTIN program)

(a)

Percent	Lower	Upper
By Inten.	100	0
By Weight	100	0
By Number	100	0

Mean = 9nm
Var. = 0.032
Skew = 0.465
RMS = 1.06E-03

DMPC/DHPC=14mg/16mg

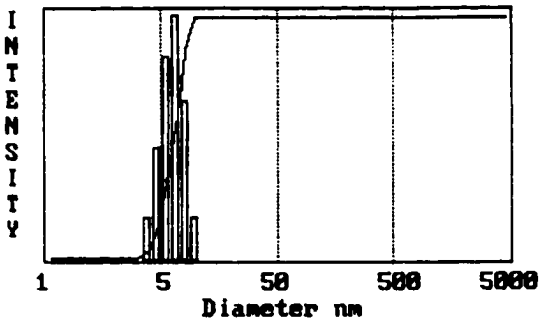

d/nm	G(d)	C(d)
5	0	0
5	0	0
6	0	0
6	19	2
7	32	6
7	48	12
8	66	21
8	83	31
9	95	43
9	100	55
10	95	67
10	83	78
11	66	86
12	48	92
12	32	96
13	19	98
14	10	100
dust	4	100

(b)

Percent	Lower	Upper
By Inten.	100	0
By Weight	100	0
By Number	100	0

Mean = 9nm
Var. = 0.098
Skew = 0.348
RMS = 2.57E-04

DMPC/DHPC=80/70 & T=10C P=50

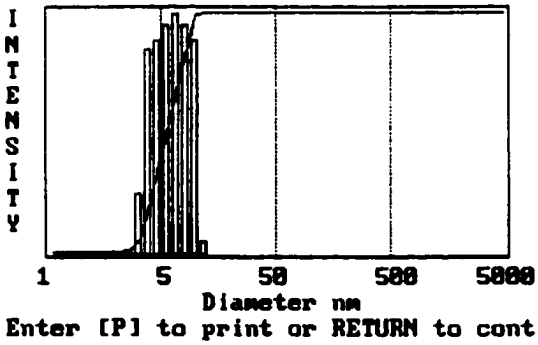

d/nm	G(d)	C(d)
2	0	0
2	0	0
3	0	0
3	0	0
4	3	1
5	26	5
6	86	19
7	90	34
8	95	50
10	100	67
11	95	83
13	90	98
16	7	99
19	0	99
23	0	99
27	0	99
32	0	99
dust	3	100

Enter [P] to print or RETURN to continue:

Scattered light intensity

Because the deduction of the shape of a scatterer by QLS methods is based on the relationship between the ratio of scattered intensity (I/I_{min}) and the size of scatterers (R_h), the dependence of scattered intensity from bicellar mixtures as a function of hydrodynamic radius must be accurately determined. The experimental results for DMPC/DHPC bicelles are plotted in Figure IV-4(a) (25mg/ml mixtures) and (b) (100mg/ml mixtures), illustrating the consistency of the data and smooth variations in intensity with size.

Fig. IV-3: Size dependence of bicelles on DMPC/DHPC molar ratio
(a) 25 mg/ml; (b) 100 mg/ml

(a)

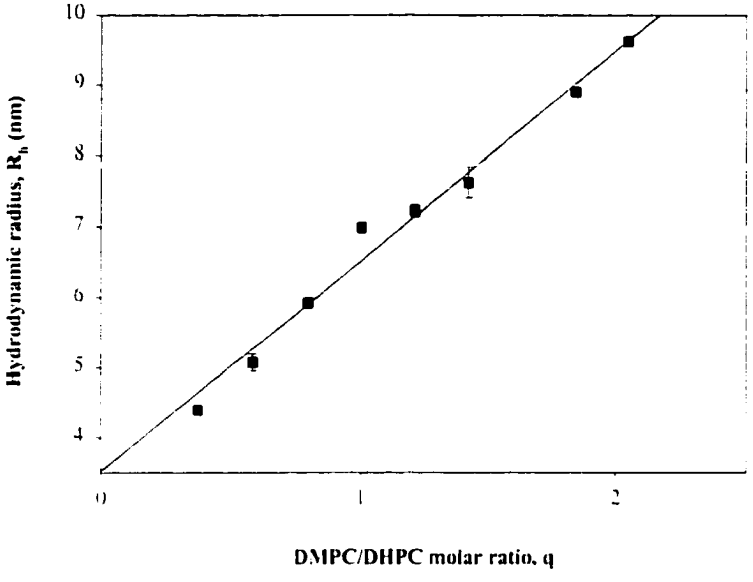

(b)

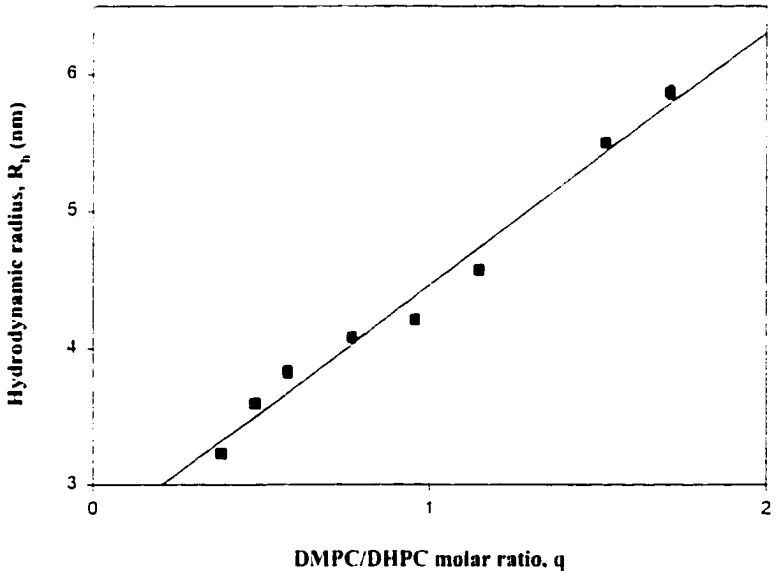

Fig. IV-4: (a) Dependence of scattered I (Kcents/sec.) on bicellar R_h at 25 mg/ml and 10°C

(b) Dependence of scattered I (Kcents/sec.) on bicellar R_h at 100 mg/ml and 10°C

(a)

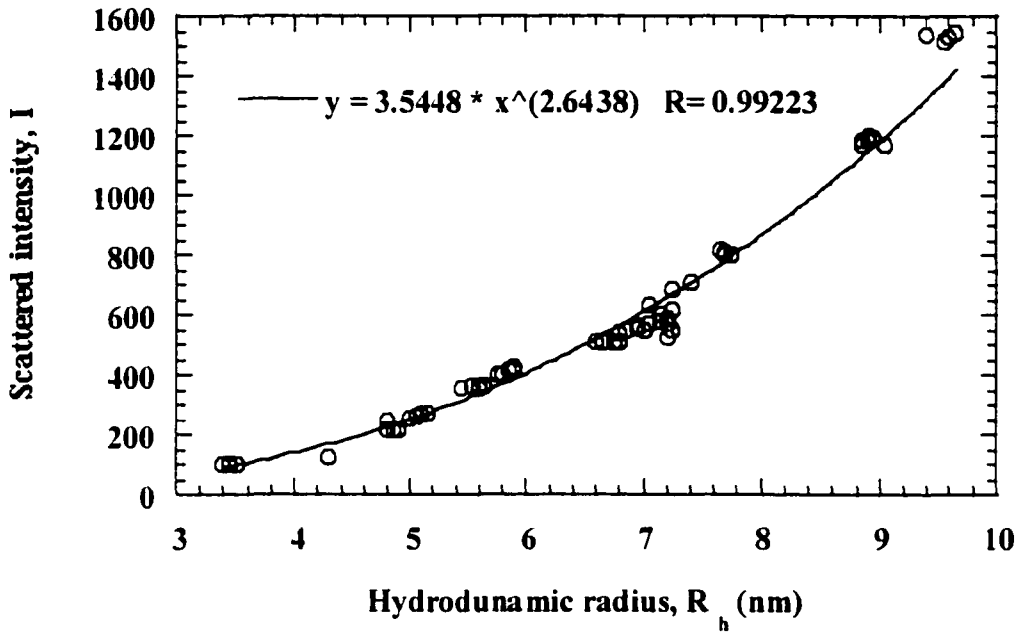

(b)

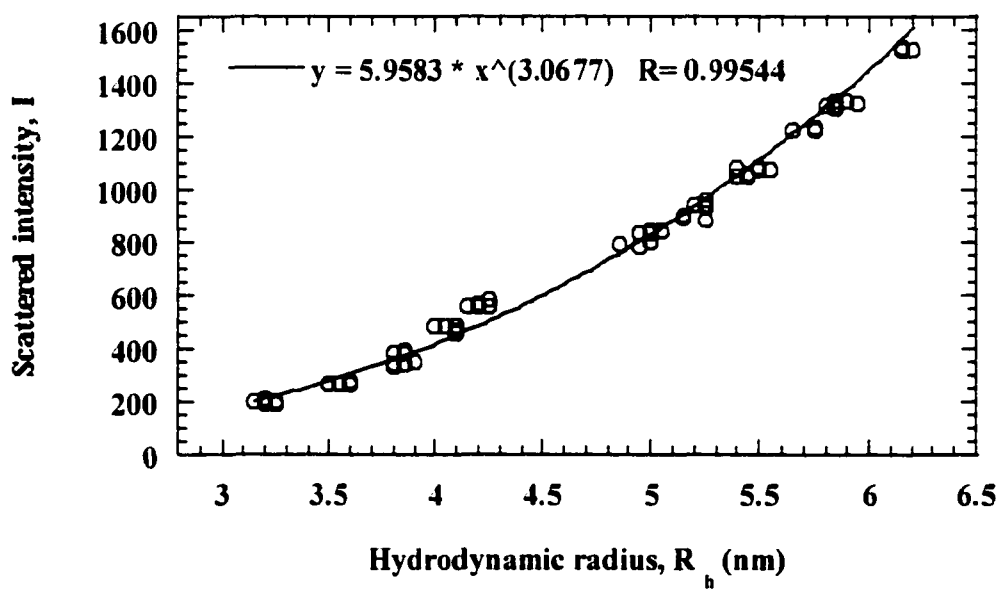

B-3 Deducing the shape of DMPC/DHPC bicellar aggregates

We used the Mazer and Carey method of dynamic light scattering (QLS), which was described in detail in Chapter II, to deduce a discoid shape for DMPC/DHPC bicellar aggregates with total lipid concentrations of 25 mg/ml (2.5% w/v) and 100 mg/ml (10.0% w/v), respectively.

The natural logarithm of the scattered intensity ratio (log I/I_{min}) is plotted against hydrodynamic radius and is compared with theoretical curves for sphere, disk, and rod models in Figure IV-5(a) (25 mg/ml mixtures) and Figure IV-5(b) (100 mg/ml mixtures). Here, the diameter of the rod cylinder was chosen as 5.0 nm and the thickness of disk was taken as 4.0 nm or 5.0 nm, reflecting different assumptions regarding the layer of water that is associated with bicellar particles. The minimum value of 4.0 nm is derived from the X-ray result for DMPC crystals (Small, 1986), but an additional 0.3-0.6 nm is usually added to each edge to account for water of hydration that tumbles with the phospholipid particles (Cantor and Schimmel, 1980). In Figure IV-5, all curves were normalized to intersect at the minimum size that was obtained in the series of QLS measurements. The QLS analyses are consistent with DMPC/DHPC bicellar aggregates having either spherical or disk shapes. The issue of choosing between these possibilities is discussed below.

Fig. IV-5: (a) Shape deduction of 25 mg/ml DMPC/DHPC bicelles by QLS

(b) Shape deduction of 100 mg/ml DMPC/DHPC bicelles by QLS

(a)

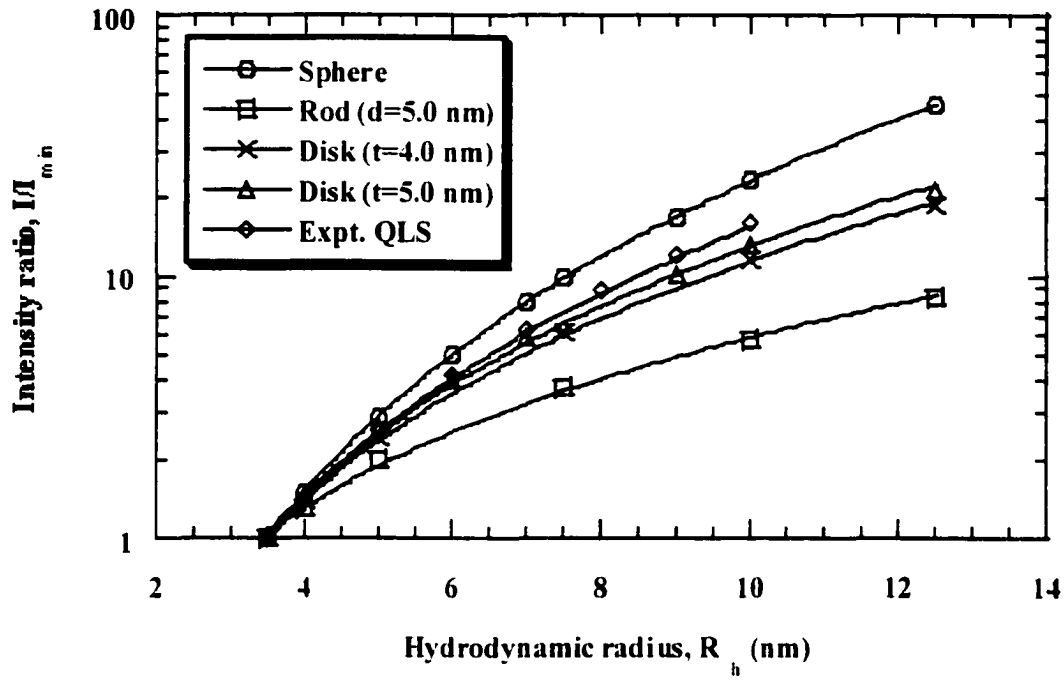

(b)

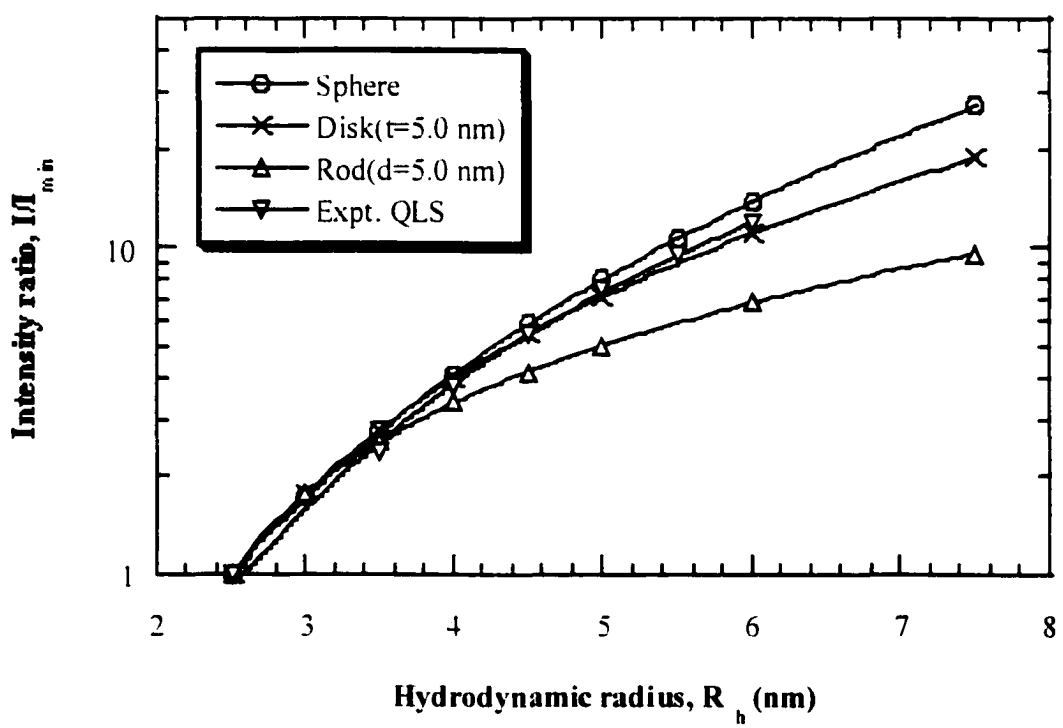

C-1 Size and size distribution of DMPC/DHPC bicellar aggregates

In order to use the formalism of Mazer and Carey (Mazer et al., 1980) with confidence to deduce the shape of micellar or bicellar aggregates, it is essential to deal with monodisperse distributions. Because phospholipid or detergent solutions may commonly form nonequilibrium mixtures, careful consideration was given to methods of sample preparation and equilibration.

Roberts et al. (Gabriel and Roberts, 1984) used two standard methods to prepare long-chain PC/short-chain PC vesicles: (1) mixing two pre-prepared PC aqueous solutions in the required molar ratio, and (2) hydrating a dry film made from organic solutions of the two PC species. In their electron microscopy measurements for short-PC/long-PC mixtures with 25 mM total lipid concentration and 0.2 molar ratio, unilamellar vesicles were formed with radii of 8-50 nm depending on the identity of the lipids. Since multilamellar aggregates form in pure DMPC solution and may persist when mixed with a DHPC solution the first preparation method is not suitable for shape analysis of binary PC bicelles. The second method is also problematic because hydrating a dry binary PC film may result in a mixture with wide size distribution or even coexistence of various structures (data not shown). Since a narrow monodisperse sample is necessary to deduce shape by QLS (Chapter II), it is evident that these two methods are not suitable for preparing the samples for this purpose.

The Vold group developed a new way to prepare DMPC/DHPC bicellar aggregates, in which an aqueous DHPC micellar solution was first made, and the required amount of dry DMPC powder was added to the DHPC solution. After the DMPC was solubilized and the solution became clear, the DMPC/DHPC mixture was put in a 40°C warm-water bath for 20 minutes. Then, it was transferred into a 4°C water bath for another 20 minutes. The process was repeated twice to make sure that the sample solution became homogeneous. Their NMR measurements were conducted at 37-40°C. We found the new method worked very well to make a monodisperse distribution of DMPC/DHPC bicelles, and the size distribution of bicellar aggregates became sufficiently narrow for QLS shape analysis after an additional 2-6 hours was allowed for equilibration (QLS results analyzed by CONTIN were shown in Fig. IV-3).

The formation of monodisperse bicelle distributions by the new method can be rationalized as follows: after sufficient mixing time (at least overnight), a homogeneous DHPC micellar aqueous system forms. When a bit of dry DMPC powder is added to the DHPC solution, the long hydrophobic chains of DMPC preferentially solubilize into DHPC micelles instead of forming multilamellar vesicles. Due to the mismatch in size of the two PCs, they form discoid aggregates rather than large spherical mixed micelles. As further DMPC powder is added, it inserts additionally into the DMPC disk domain, so that the size of the bicelles is found to gradually increase as predicted by the Vold model (Eq. IV-1). Achieving a narrow size distribution of DHPC micelles is an

essential requirement for further shape analysis of DMPC/DHPC mixed bicellar aggregates.

C-2 Optimizing QLS determinations of the shape of DMPC/DHPC bicelles

Although numerous prior investigators have assumed that long-chain PC/short-chain binary PC aggregates have a discoid shape, our QLS analyses provide the first independent experimental evidence for this assertion in isotropic solution. Nevertheless, the scattered intensity ratio vs. R_h curves in Fig. IV-5(a) and (b) lie above the predicted curve for the disk model at large sizes. Several adjustments are considered in the following discussion.

The most direct explanation of this anomaly is inter-aggregate scattering. If there were measurable inter-aggregate scattering, it would become more serious as the incident light power increases and would cause higher-than-expected scattered intensity. To check this hypothesis, scattered intensity was measured as a function of incident power with constant temperature (10°C), total lipid concentration (25 mg/ml or 100 mg/ml), molar ratio, and other QLS parameters. Figure IV-6 shows a linear relationship between scattered intensity and incident light power, excluding the possibility of inter-aggregate scattering as the source of extra scattered intensity.

Fig. IV-6: Dependence of scattered intensity on incident power at constant bicellar size, total lipid concentration, molar ratio, and temperature

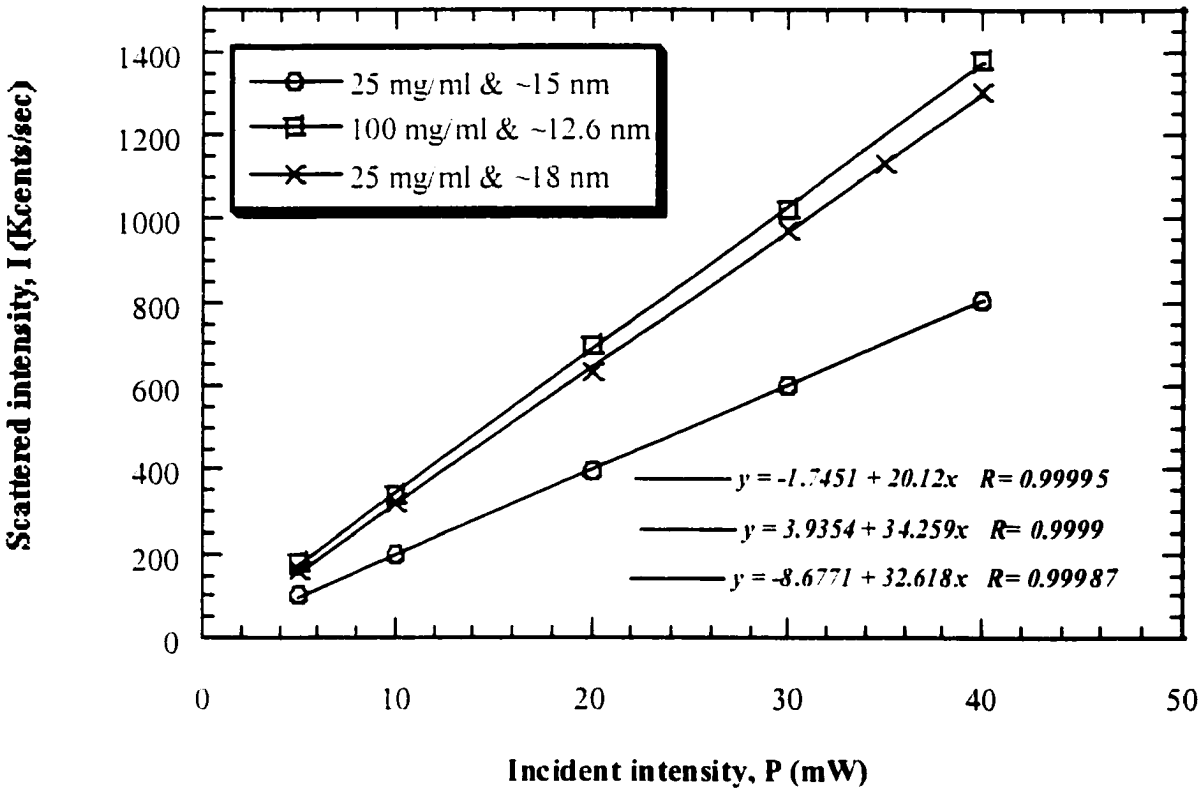

Secondly, the choice of size parameters for the disk model (thickness of disk) and rod model (diameter of rod cylinder) could be a factor affecting the theoretical I/I_{min} curves. A larger thickness will raise the disk curve and bring it into closer agreement with the experimental data. In fact, the disk thickness measured by QLS should include two DMPC molecular lengths (2.5 nm with extended DMPC chains) and a water hydration layer (0.28 nm × 2). Thus 4.0 nm is probably too small a value to use as the thickness of a bicellar disk. The thickness of the disk could be as large as 5.5-6.0 nm, but Figure IV-5(a) shows that the curves with disk thicknesses of 4.0 nm and 5.0 nm are almost coincident. Thus the size parameter is probably not the reason for the evident deviation in the scattered intensity ratio curve (Fig. IV-5).

Thirdly, it is possible that a certain number of simple DHPC micelles remain in the mixture after a small amount of DMPC is added into the DHPC micellar solution. Thus a correction to the total mixed bicellar concentration would be necessary, since the deviation in concentration should have a negligible effect for higher ratio q bicelles but a noticeable effect for lower ratio q bicelles. This determination has an impact on the shape determination through I/I_{min}, which really should be calculated as $(I/C)/(I/C)_{min}$ (Mazer et al., 1980).

If a certain number of simple DHPC micelles exist in bicellar solution, the total concentration of mixed bicelles will be lowered ($C_{mixed} = C_{total} - C_{simple\ DHPC}$). The

intensity ratio curve (I/I_{min}) will then shift upward because I/I_{min} is larger than $(I/C)/(I_{min}/C_{min})$ if C_{min} is smaller than C.

In order to distinguish simple DHPC micelles from mixed bicelles, aggregate size was determined in a 25 mg/ml aqueous sample of DHPC at 10°C. The measurement showed that the hydrodynamic radius of DHPC micelles was 2.0 nm, in agreement with data reported by Roberts (Eum et al., 1989). Thus in the following analysis of the results for bicelles, it was possible to treat aggregates smaller than 2.0 nm as simple DHPC micelles, and those larger than 2.0 nm as mixed DMPC/DHPC bicelles.

We assume that after a small amount of DMPC is added to a stable DHPC solution, the total number of particles (simple DHPC micelles plus mixed DMPC/DHPC bicelles) is the same as the original number of DHPC micelles before DMPC is added. Since DMPC does not dissolve in water, the only thing happening is the solubilization of DMPC into DHPC micelles. We can calculate the fraction of DHPC that remains as pure micelles based on the proportionality of scattered intensity to the product of concentration (w/v) and 6^{th} power of diameter ($I \sim Nd^6$). Because the assumption of a constant number of total aggregates is valid only at rather low DMPC/DHPC molar ratios, two low ratios (q=0.167, 0.334) of 25 mg/ml bicellar mixtures were added to the original series of mixtures. The correction to C_{min} was based

on scattered intensities tabulated by CONTIN (Fig. IV-7); and a detailed example of the concentration correction for 25 mg/ml and q=0.376 bicelles is given in Table IV-2.

Fig. IV-7: CONTIN results for 25 mg/ml DMPC/DHPC bicelles (q=0.376) at 10°C

Percent	Lower	Upper
By Inten.	100	0
By Weight	100	0
By Number	100	0

Mean = 7nm
Var. = 0.043
Skew = 0.351
RMS = 1.43E-03

DMPC/DHPC=9mg/16mg

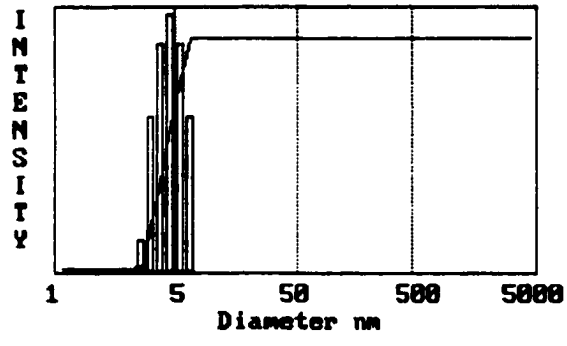

d/nm	G(d)	C(d)
4	0	0
4	13	1
5	21	4
5	32	7
5	45	12
5	60	18
6	75	26
6	88	35
7	97	45
7	100	56
7	97	66
8	88	75
8	75	83
9	60	89
9	45	94
10	32	97
10	21	100
dust	4	100

Table IV-2: Concentration correction for 25 mg/ml DMPC/DHPC bicelles (q=0.376) at 10 °C

R_h (nm)	Scattered I (G(d))*	Relative Num. Fraction of DHPC micelle (10^{-3})**	Num. Of DHPC mocelle %***
2.0	13	3.174	15.75
2.5	158	10.11	50.18
3.0	163	3.494	17.34
3.5	294	2.499	12.40
4.0	163	0.6218	3.090
4.5	105	0.1976	0.981
5.0	53	0.0530	0.263

* The value G(d) indicates the scattered intensity contributed by each size fraction.

** The value is estimated based on the proportional relationship of scattered intensity I to the product of the number of the scatterers and the 6^{th} power of the size ($I \sim NR_h^6$).

*** The number % is calculated by the equation: $N\%(i) = N(i)/\sum N(i)$.

The mass of DHPC micelles and mixed bicelles could be calculated as follows:

$$\text{Mass(simple DHPC micelles)} = 16 \times 15.75\% = 2.52 \text{ (mg)}$$

$$\text{Mass(mixed DMPC/DHPC bicelles)} = 16 + 9 - 2.52 = 22.48 \text{ (mg)}$$

Thus, the intensity ratio curve should have the form $(I/25)/(I/22.48)_{min}$ instead of I/I_{min}. An analogous correction was performed for all low q bicellar mixtures.

Alternatively, the problem of residual simple DHPC micelles may be avoided by discarding data that show a size fraction with hydrodynamic radius smaller than 2.0 nm. Although this modification will diminish the size range of QLS curves used in shape deduction, it may provide a more reliable correction than the first procedure.

The curves of scattered intensity vs. hydrodynamic radius for 25 mg/ml bicellar mixtures are shown in Fig. IV-7 (a) (q: 0.167 - 2.049 without correction), (b) (q: 0.167 - 2.049 with concentration correction), and (c) (q: 0.418 - 2.049 mixtures without simple DHPC micelles).

All three curves in Fig. IV-8 were fit to a power law, which reflects the volume of the scatterers. An interesting trend is evident in the order of these curves. The original curve (Fig. IV-3(a)) has an order of 2.63. After adding new lower-ratio data but

with no concentration correction, the power rises to 2.99 because there are more spherical DHPC micelles. After concentration correction, the power decreases to 2.52. If only QLS data without DHPC micelles are considered, the power decreases to 2.47. Physically, the power 3 corresponds to a spherical shape since the scattered intensity I is proportional to the volume of scatterers (i.e. R_h^3). We can predict that shape analysis based on the curve in Fig. 8(a) will yield a sphere, because the curve power is almost 3. After concentration correction by both methods outlined above, the power order decreases because we eliminate the impact of simple DHPC micelles on apparent bicellar concentration.

Does the concentration correlation yield the expected disk shape following QLS analysis? The shape analysis of 25 mg/ml bicelles based on corrected scattered intensity curves is shown in Fig. IV-9(a) (micellar concentration correction) and IV-9(b) (excluding data with DHPC micelles). Both results demonstrate that the shape of DMPC/DHPC bicelles is very well fit to a discoid shape, with particularly good agreement by the second method. The second method was also used to analyze the 100 mg/ml bicelles. The corrected scattered intensity curve and the shape analysis are shown in Figures IV-9(a) and (b), respectively.

Fig. IV-8: Dependence of scattered intensity of 25 mg/ml of bicelles on R_h

(a) Scattered intensity of 25 mg/ml bicelles vs. R_h at 10°C (q: 0.167-2.049)

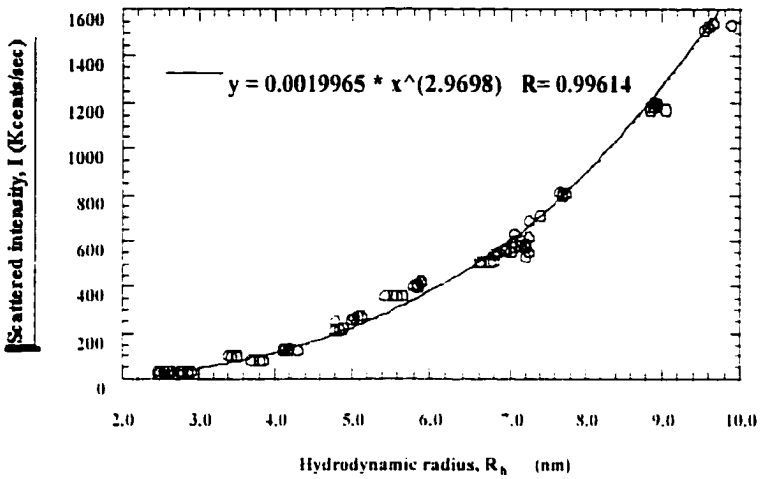

(b) Scattered intensity of 25 mg/ml bicelles vs. R_h at 10°C (conc. corrected)

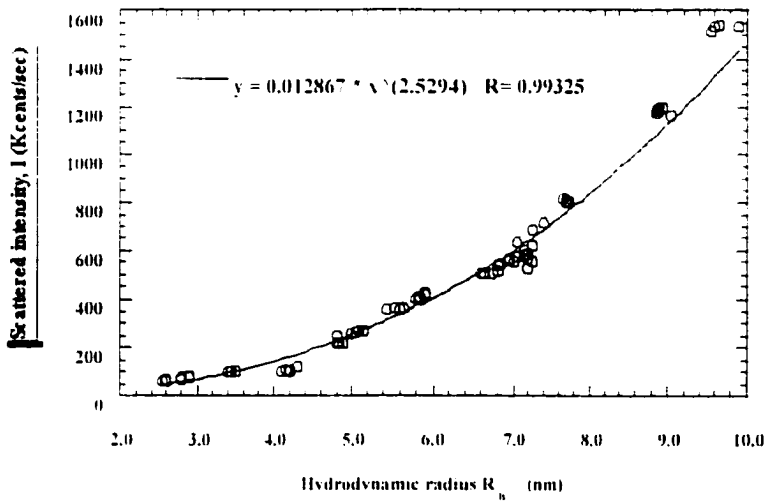

(c) Scattered intensity of 25 mg/ml bicelles vs. R_h at 10°C (R_h>2.0 nm)

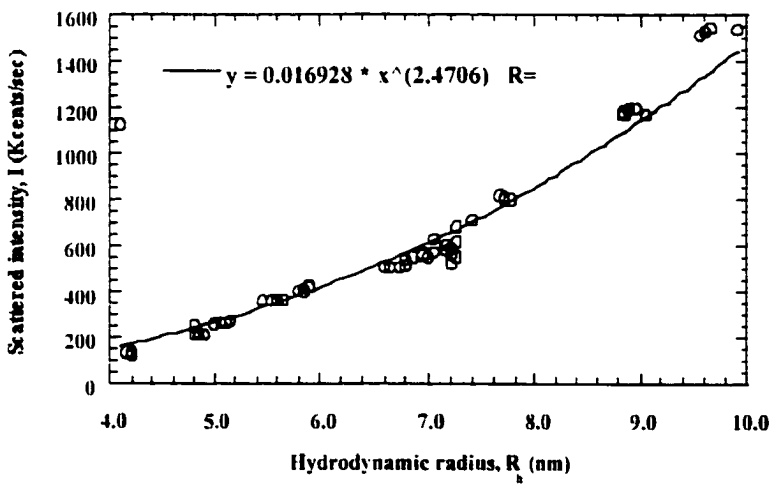

Fig. 9: (a) Shape deduction of 25mg/ml DMPC/DHPC bicelle by QLS (conc. corrected)

(b): Shape deduction of 25mg/ml DMPC/DHPC bicelle by QLS (R_h>2.0 nm)

(a)

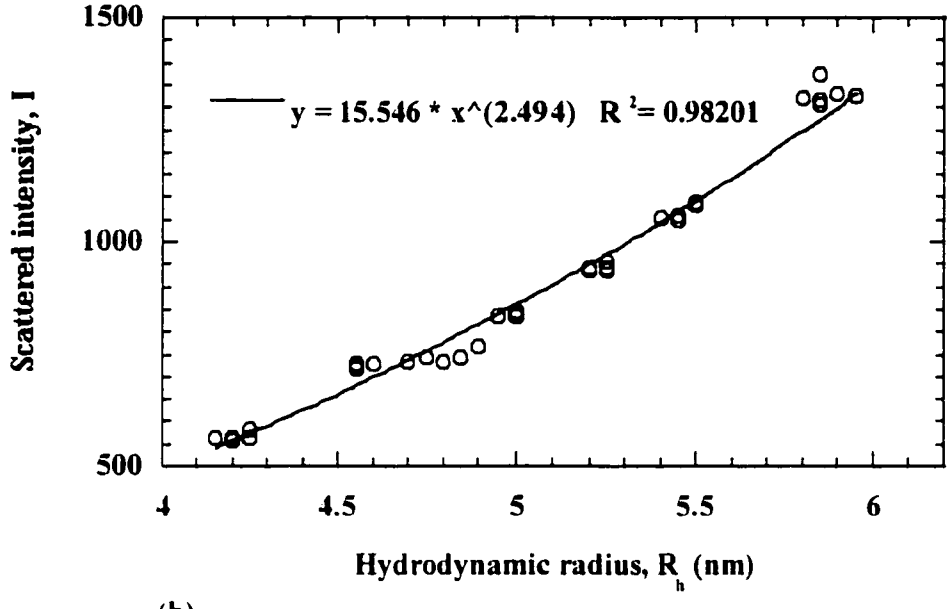

(b)

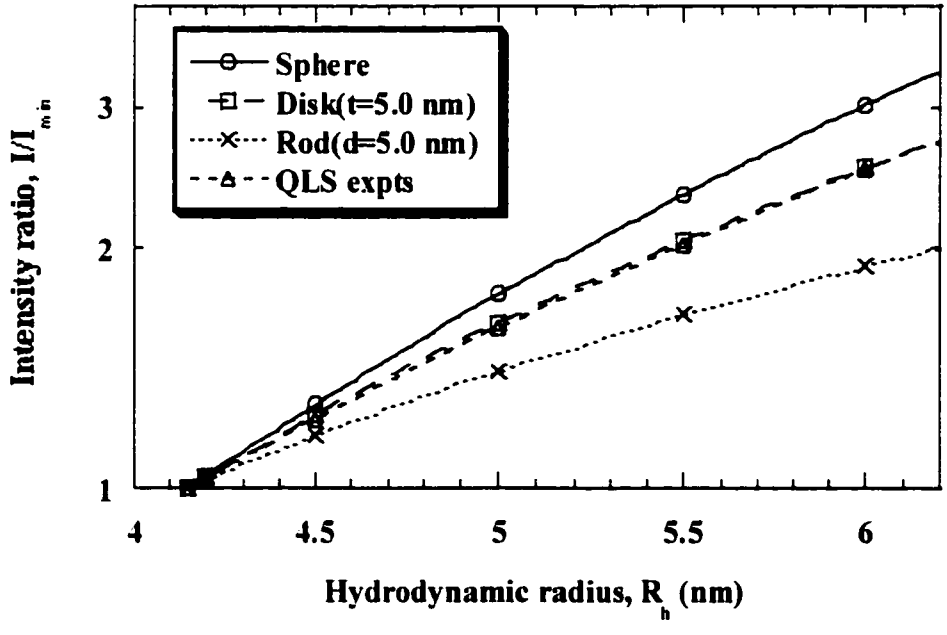

C-3 Further consideration of the Vold diskoid model

The Vold-Prosser model for DMPC/DHPC bicelles (Fig. IV-1) provides a very elegant physical description of the structure. Two approximations were made at the outset: DMPC and DHPC molecules are completely separated in two different domains; and the headgroup areas of DMPC and DHPC are the same. Although these assumptions greatly simplify the deduction of the Vold equation for R (Eq. IV-1), they may produce cause some deviation between the theoretical model and QLS experimental results.

A comparison of the dependence of disk diameter on DMPC/DHPC molar ratio, using the Vold model and our QLS results, is shown in Figure IV-11. The QLS data were based on measurements of a series of 25 mg/ml bicellar mixtures with different DMPC/DHPC molar ratios at 10°C. Because the scatterers are assumed to be spherical in the Stocks-Einstein equation (Eq. II-5), the hydrodynamic radii R_h from QLS must be converted to the corresponding size for a discoid before comparison. The steps in the calculation are illustrated in Appendix A.

Fig. IV-10: Size deviation between Vold model and QLS experimental results

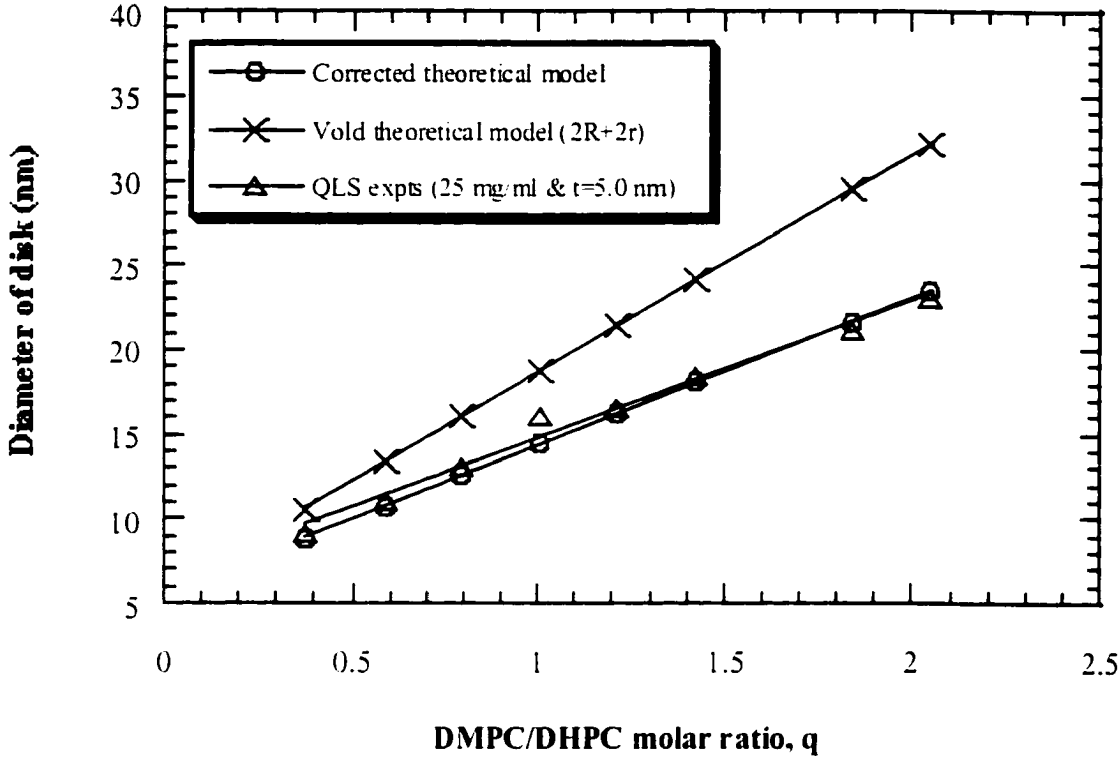

Although both the Vold model and QLS experimental results for 25 mg/ml bicellar mixtures display a similar relationship between bicellar size and DMPC/DHPC molar ratio in Fig. IV-11, the former always has a larger size than the latter. After we take the quotient of the two diameters (d_{Vold}/d_{QLS}) at each molar ratio q, we further find that the fractional deviation is in the range 1.15 - 1.60.

The deviations demonstrated in Figure IV-11 are not surprising, because DHPC molecules located in the bent rim domain will occupy more surface area than DMPC molecules in the central planar domain. If we introduce a factor of k to the conversion of the quotient of areas to a quotient of concentrations, we can follow the Vold procedure (Vold et al., 1996) and deduce a new equation as follows:

$$A(DMPC) = 2\pi R^2 \qquad \text{(Eq. IV-2)}$$

$$A(DHPC) = 2\pi r(\pi R + 2r) \qquad \text{(Eq. IV-3)}$$

where R is the radius of the DMPC planar domain and r is the radius of the DHPC rim domain.

Then $$q = A(DMPC)/A(DHPC) = [DMPC]/k[DHPC] \qquad \text{(Eq. IV-4)}$$

A new expression for the size of the bicelle as a function of DMPC/DHPC molar ratio can be obtained from equations Eq. IV-2 and Eq. IV-3:

$$R = (1/2k)rq\{\pi + (\pi^2 + 8k/q)^{1/2}\} \qquad \text{(Eq. IV-5)}$$

The factor of k in equation IV-5 can be defined quantitatively as the quotient of the area of each DHPC molecule in the bent rim and that of each DMPC in the bilayer disk. Since the headgroup of the DHPC occupies a larger area than that of the DMPC, k is always larger than 1, so that the size calculated from the new equation will agree more closely with the experimental QLS results shown in Figure IV-11.

Gawrisch and coworkers reported that the each headgroup of DMPC in a fully hydrated bilayer occupies 0.6 nm^2 (Koenig et al., 1997). Roberts also showed that each short chain lecithin molecule has a surface area of 1.0 nm^2 in spherical micelles and 0.65 nm^2 in the bilayer plane based on small angle neutron scattering (SANS) measurements (Gabriel and Roberts, 1987). These results allow us to correct the deviation of the theoretical discoid model due to the assumption about polar end-groups. In addition of Vold's assumption that all phospholipid molecules, including both DMPC and DHPC, are assembled in bicelles, we further assume k=1.5 since a(sphere)/a(plane) = 1.0/0.65 $\approx$ 1.5. After apinserting k into Eq. IV-5, we can calculate the size of model disk at different value of q (Fig. IV-11).

The size dependence of the new corrected discoid model shows excellent agreement with the QLS experimental results in Fig. IV-11. It demonstrates that the deviation between Vold model and QLS experiments is mainly caused by a problematic assumption about the polar end-groups.

Chapter V Semi-solid NMR studies of sphingomyelin/cholesterol model membranes

A Introduction and Significance

Most biomembranes are formed from phospholipids. Among the more polar glycerophospholipids and sphingolipids, two choline-containing phospholipids, phosphatidylcholine (PC) and sphingomyelin (SM), are found in relatively large amounts (17 mol % each in human erythrocyte cell membranes (Yeagle, 1993). The typical molecular structures of PC and SM are shown in Fig. V-1. Numerous detailed studies of the structures of phosphatidylcholine membranes have been done with various techniques, for example X-ray scattering and NMR spectroscopy. However, investigations of sphingomyelin, especially synthetic sphingomyelin, are relatively rare because of its complicated phase characteristics and difficulties in synthesis and purification (Bruziket al., 1990).

Sphingomyelins (SM) are sphingolipids with a molecular structure related to other phospholipids, containing a phosphorylcholine-like headgroup and two phosphatidylcholine-like hydrocarbon chains, mainly C_{18}. They differ from phosphatidylcholine in their backbone structure and position of double bond in the hydrocarbon chain (Fig. V-1). Sphingomyelin is an important element in some plasma membranes, including human erythrocyte membrane where it appears in approximately

Fig. V-1: Molecular structures of PC (DMPC), sphingomyelin (SM), and cholesterol (CHL)

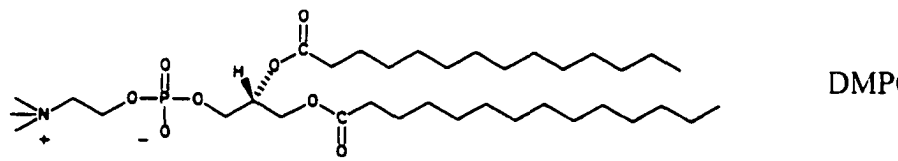

DMPC

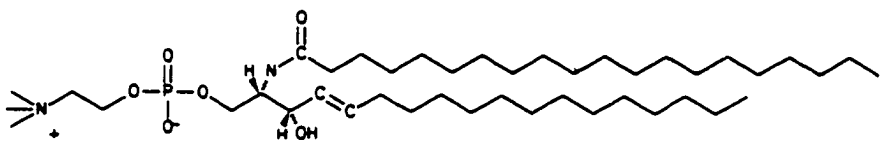

SM

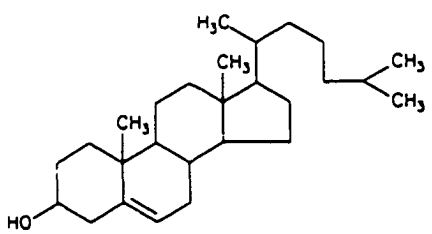

CHL

equal ratio to phosphatidylcholine (Yeagle, 1993). Prior ^{31}P NMR studies showed that sphingomyelin displayed quite different gel-liquid crystalline (L_α) phase transition behavior from that of phosphatidylcholine (Yeagle et al., 1978). For example, DMPC has its phase transition temperature at 25°C; SM with C16:0 hydrocarbon chains shows a simple reversible phase transition at ~41°C; SM with C18:0 hydrocarbon chains undergoes a main phase transition at 57°C and another small but metastable bilayer phase melting at 44°C; whereas SM with C24:0 hydrocarbon chains exhibits more complex thermotropic behavior (Yeagle, 1978; Maulik and Shipley, 1996).

Cholesterol (CHL) (Fig. V-1) is a steroid molecule. Although cholesterol is known as the main cause of atherosclerosis, it is clear that CHL also regulates the order and fluidity of lipid bilayer membranes. Differential scanning calorimetry (DSC) and X-ray diffraction experiments demonstrated that cholesterol molecules could insert readily in the sphingomyelin membrane structure. However, there is still controversy about many features of CHL-containing phospholipid membranes in aqueous dispersions, for example, the precise position of CHL in the SM membrane and the preferred locations of molecular interaction between SM and CHL.

The order parameters of the hydrocarbon chain segments supply valuable structural information on lipid bilayer assemblies, that is the orientational order of each C-^{2}H bond which is reflected in the quadrupole splitting of the ^{2}H NMR spectrum. The addition of cholesterol to phospholipid bilayer assemblies results in a condensation of

phospholipid area, reflected in a drastic increase in methylene chain order. The order information has been obtained using selectively labeled lipids and ^{2}H NMR (Yeagle, 1993). Although the order parameters can be obtained directly from the observed quadrupole splitting in a ^{2}H NMR spectrum, this approach is restricted in practice because the selective synthesis is often very difficult and costly. In order to overcome this problem, new 2D NMR techniques have been introduced (Urbina and Oldfield, 1998).

The presence of significant dipolar-dipolar interactions in semi-solid (liquid-crystalline) lipid bilayer samples results inevitably in sidebands in the ^{1}H NMR spectrum even though MAS is applied. The spinning sideband (SSB) intensities depend on the speed of spinning, and there is a qualitative relationship between the SSB intensity and the order of membrane systems. SSB intensities have been used to obtain order information for DMPC (Forbes and Oldfield, 1988; Huster et al., 1998) and egg PC (Li et al., 1993). A theoretical calculation reveals that the sideband intensity at low spinning speeds (2-3 kHz) has similar sensitivity to changes in chain order as the ^{2}H NMR order parameters (Gawrisch, K., unpublished).

There are several new 2D NMR techniques now available to study the order parameters of phospholipid membranes using solely natural abundance nuclei. One of these methods uses high-resolution ^{13}C cross-polarization and magic angle spinning (CPMAS) NMR combined with ^{1}H solid echo (SE) wideline spectroscopy (Urbina and

Oldfield, 1998). Since an accurate ^{1}H solid-echo wideline shape is transferred to each directly-coupled carbon through the variable amplitude cross polarization (VACP) technique (Peersen and Smith, 1993), the order parameters of the methylene chains and the effect of CHL on each chain order parameter can be evaluated based on the linewidths in the SEVACP spectrum (Chapter I, Section C-6).

The CPMAS ^{13}C NMR spectrum has advantages of particularly high resolution and a wide chemical shift range. It can be used to observe chemical shift changes of various ^{13}C peaks after CHL is mixed with the original phospholipid membrane, and to interpret these changes in terms of chain conformational changes (Forbes and Oldfield, 1988).

In this research project, the three NMR experiments described above were used to study the impact of CHL on SM membrane structure: ^{1}H sideband intensity as a function of spinning speed; order parameters of hydrocarbon chains by SEVACP; and ^{13}C chemical shift of methylene peaks as a function of mol % CHL. In order to compare the effect of CHL on different phospholipids, parallel NMR experiments were performed for commercial 1,2-Dimyristoyl-*sn*-glycero-3-phosphocholine (DMPC), bovine brain sphingomyelin (BSM), and synthetic–stearoyl (18:0) sphingomyelin (SSM) at comparable temperatures. Here DMPC was chosen because it was the most-well studied phospholipid, and commercial BSM was also used because a comparison between BSM and SSM could evaluate the impact of a well-defined SM structure.

B NMR experiments

B-1 Materials and sample preparation

Commercial 1,2-Dimyristoyl-*sn*-glycero-3-phosphocholine (DMPC) and bovine brain sphingomyelin (BSM) were purchased from Avanti Polar Lipids, Inc. (Alabaster, Alabama, USA). Cholesterol (CHL) was purchased from Aldrich (Milwaukee, WI, USA). Synthetic sphingomyelin (SSM) was supplied by Professor Robert Bittman's group, Queens College/CUNY. All compounds were used directly as received.

A certain weight of dry phospholipid powder (DMPC, BSM, or SSM) was dissolved in a mixture of $CHCl_3$ and CH_3OH (50:50 v/v) in a clean plastic cell. The solution was blown to a dry film using N_2 gas. Then the film was placed under vacuum at least overnight to evaporate residual organic solvents.

The required mass of D_2O was added into the plastic cell to dissolve the lipid film (~50-75% D_2O w/w). After the mixture was well mixed, the sample was equilibrated using four freeze-thaw cycles to make sure the mixture was homogeneous. Samples were stored in the freezer (-10°C).

To prepare a lipid/CHL sample, the required mass of CHL powder was added to the original pure lipid sample and the same procedure described above for pure lipid was followed.

B-2 Temperature calibration of NMR probes

Temperature is so important in evaluating sideband intensities, ^{13}C chemical shift movements, and linewidth of ^{1}H powder patterns that it would be impossible to compare experimental results if the temperature were not accurately set. Because of the distance between the probe heating coil and temperature sensor and the NMR rotor, there may be significant differences between the temperature displayed and the real temperature in the NMR rotor.

The temperature was calibrated using the method introduced by Neue (Neue and Dybowski, 1997). The method is based on the fact that, before and after melting of crystalline compounds, the lineshape of the ^{1}H NMR spectrum shows significant differences since the sample is changing from solid state to liquid state. A crystalline compound with known melting temperature is added to the NMR rotor and its ^{1}H MAS NMR spectrum is acquired at increasing temperatures until a characteristic ^{1}H solution spectrum is observed. The temperature calibration for the 5mm DOTY triple resonance probe is shown in Table V-1 and Figure V-2. Two other probes, a 7mm Varian probe

and an XC-5 DOTY probe, were also calibrated using the same method (data not shown).

Unless specified otherwise, the temperature cited in the following NMR experiments is the real temperature in the NMR rotor. Since the ^{1}H sideband intensities, ^{13}C chemical shifts, and methylene chain order parameters are sensitive to experimental temperature, the comparison between DMPC and sphingomyelin must be made at comparable temperatures. Here the same reduced temperature T_r (0.03) was used for DMPC, BSM, and SSM, as defined by Eq. V-1.

$$T_r = (T_{experiment} - T_m)/T_m \qquad \text{(Eq. V-1)}$$

Table V-1: Temperature calibration of DOTY 5mm NMR probe

Fig. V-2: Temperature calibration of 5mm DOTY NMR probe

Compound	T_m °C (literature)	T_m °C (displayed)
2-methyl-2-propanol	20-23	20
Phenol	40-42	53
Benzophenone	49-51	67
Phenylacetic acid	77-78.5	114

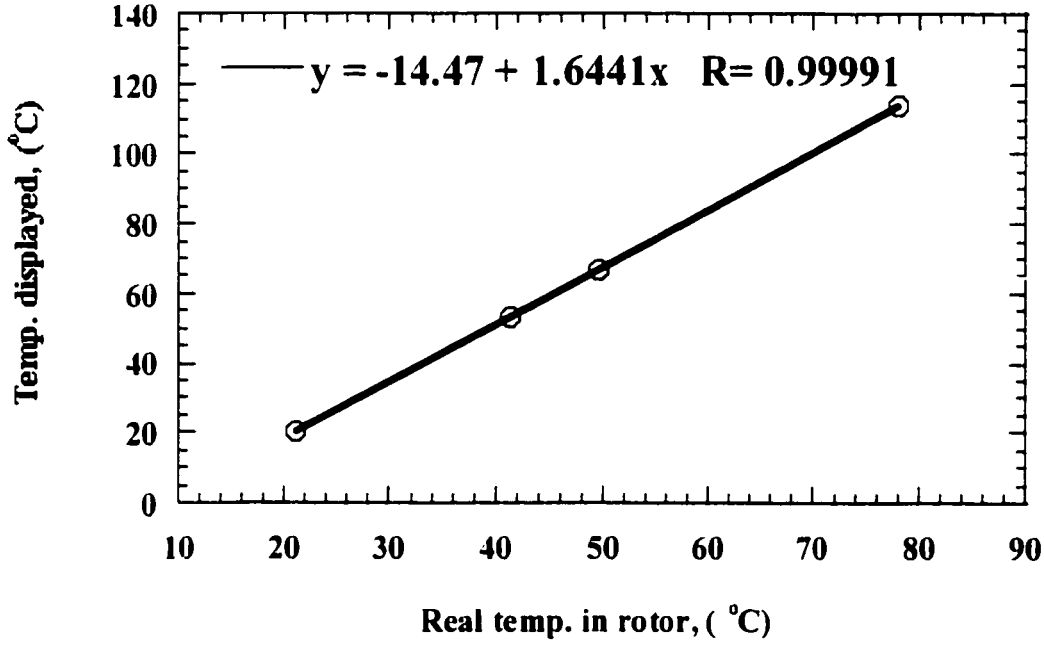

B-3 Evaluating lipid membrane order from the dependence of ^{1}H sideband intensity on spinning speed

A high-resolution ^{1}H NMR spectrum can be obtained for a liquid crystalline sample by using the MAS NMR technique. However, since there are residual intramolecular dipolar interactions in partially ordered semi-solid membranes, sharp spinning sidebands (SSB) appear alongside the high-resolution central spectrum in the ^{1}H MAS data. Analyzing sideband intensities of ^{1}H MAS spectra as a function of spinning speed is a simple method to evaluate chain order in membrane structures. Since cholesterol peaks will not appear in the lipid ^{1}H MAS spectrum after it is added to DMPC or SM, the dependence of the ^{1}H sideband intensities on spinning speed can clearly show the effect of CHL-induced chain ordering.

300 MHz ^{1}H MAS NMR experiments for DMPC, BSM, SSM, and their mixtures with CHL were performed at the same reduced temperatures, as described above. The typical 90° pulse length was ~12 μs. A typical ^{1}H MAS NMR spectrum for 100% bovine brain sphingomyelin (BSM) at 67°C (T_r=0.03) and 4000 Hz spinning speed is shown in Figure V-3. In this spectrum, the first and the second sidebands are clearly observed. A series of measurements were performed for DMPC, BSM, and SSM from ~1000 Hz to ~6000 Hz. The measurements at slower spinning speeds (<1000 Hz) are not useful for data analysis because of serious peak overlap. The intensities were found by peak integration, and the average of the same order sidebands was used in the

calculation of percent sideband intensity compared with the centerband. The curves of sideband intensity are plotted as a function of spinning speed in Figures V-4 (DMPC at 34°C), V-5 (BSM at 67°C), and V-6 (SSM at 67°C).

Fig. V-3: ^{1}H MAS NMR spectrum for bovine brain sphingomyelin at 67°C and 4000 Hz

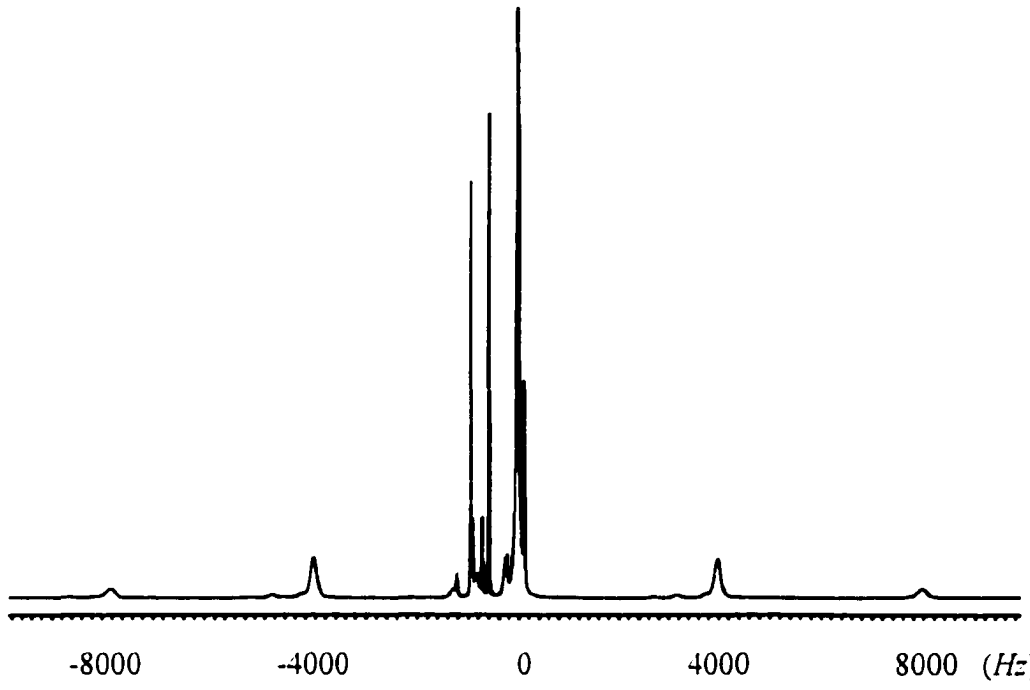

Fig. V-4: ^{1}H MAS sideband intensity % vs. spinning rate for 100% DMPC at 34°C

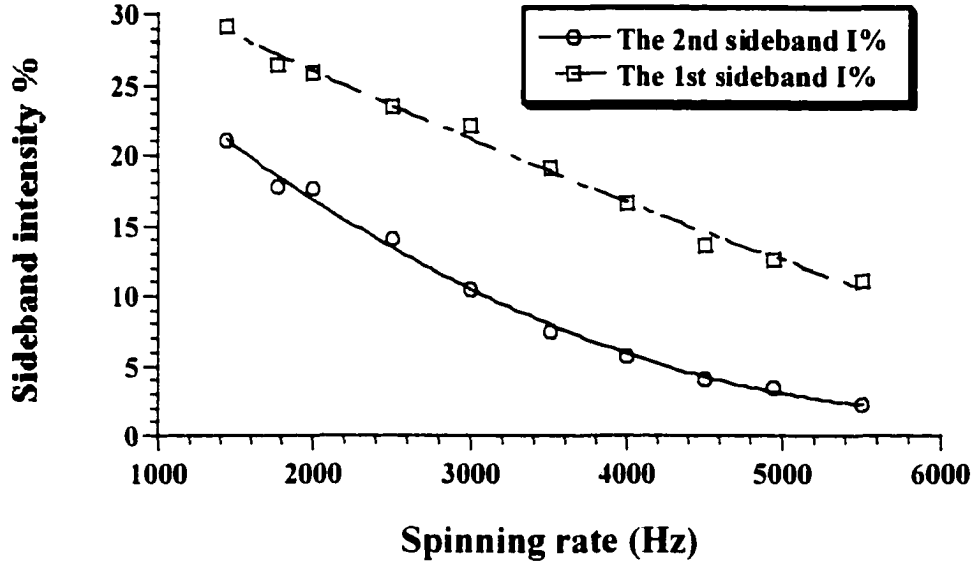

Fig. V-5: ^{1}H MAS sideband intensity vs. spinning speed for 100% BSM at 67°C

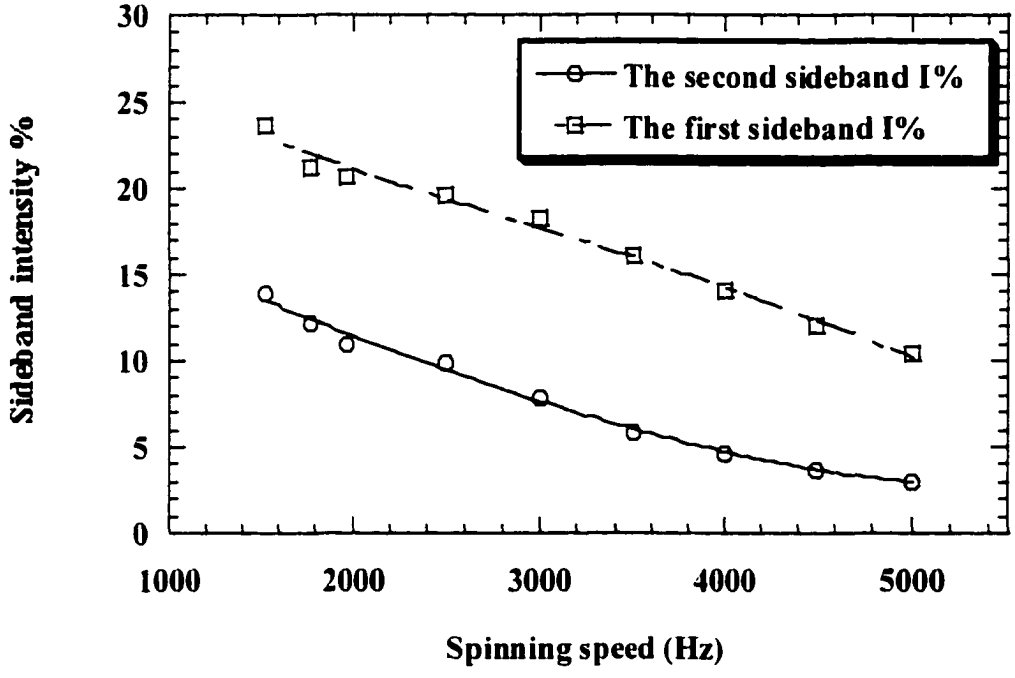

Fig. V-6: ^{1}H MAS sideband intensity vs. spinning rate for 100% SSM at 67°C

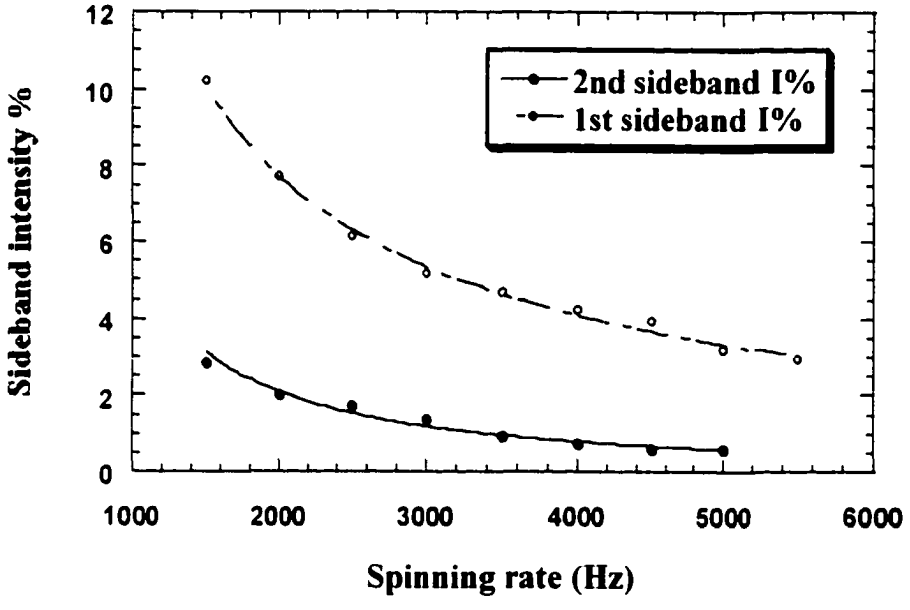

The addition of cholesterol to DMPC, BSM, and SSM results in the increase of ^{1}H MAS sideband intensity fraction, as expected. ^{1}H MAS sideband intensity % at different spinning speeds between 100% DMPC and 85%DMPC&15%CHL; and 100% BSM & BSM(75%)/CHL(25%) mixtures are shown in Figure V-7. DMPC is more sensitive to CHL induced changes in order than BSM. Detailed comparison among the lipid membrane samples appear in Section C-1.

Fig. V-7: ^{1}H 1^{st} sideband intensity % vs. spinning speed for DMPC/CHL and BSM/CHL mixtures

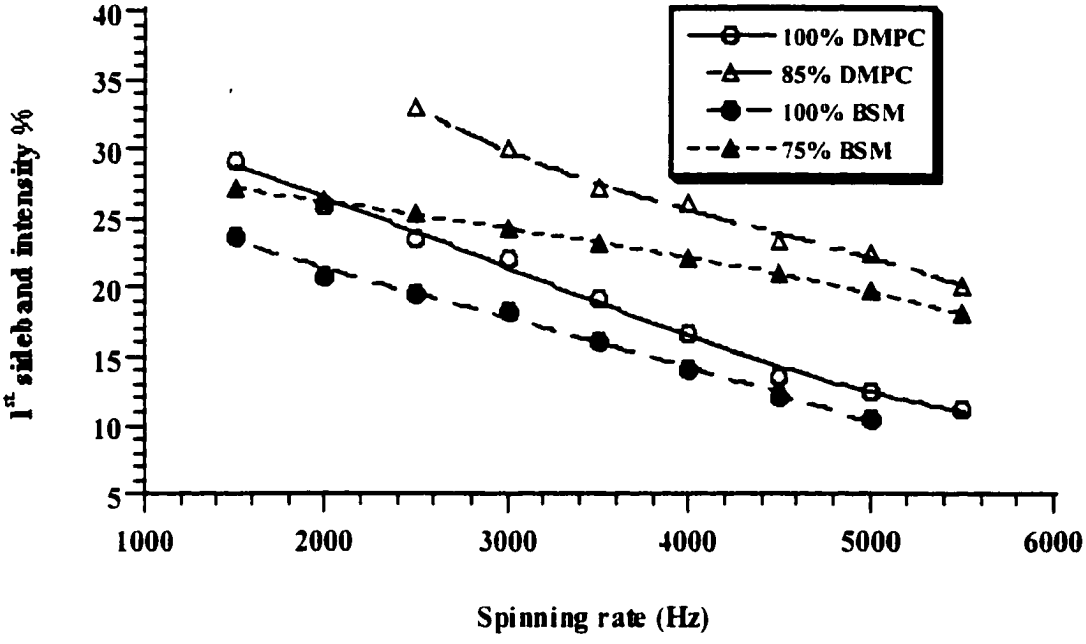

B-4 Cholesterol-induced ^{13}C chemical shift changes from VACP experiments

Because the chemical shift reflects the effect of electronic shielding, ^{13}C chemical shift changes can be used to monitor the change in molecular conformation after different amounts of CHL are mixed with phospholipid membranes. Oldfield first reported a ~1 ppm downfield movement of the ^{13}C bulk methylene peak after adding 50 mol % CHL to DPPC (Forbes and Oldfield, 1988), attributing it to a deshielding effect from more *trans*-conformation of the lipid acyl chains.

Due to the low natural abundance of the ^{13}C nucleus, solid-state ^{13}C NMR spectroscopy benefits from the use of cross polarization techniques to enhance the signal sensitivity. It is often difficult to choose a single CP matching condition for all carbon nuclei since in semi-solid lipid samples, molecular motion produces a sharply oscillatory Hartmann-Hahn condition (Peersen and Smith, 1993). New VACP (variable amplitude cross polarization) and RAMP (ramped amplitude cross polarization) techniques can be used to achieve a more even sampling all of the spins. In this work, VACP was used instead of traditional constant-amplitude CP.

75.443 MHz ^{13}C VACP MAS data were acquired for DMPC, BSM, SSM, and their mixtures with CHL. The typical 90° pulse length was 5.5-6 μs and the CP contact time was ~9000 μs. A downfield chemical shift trend was found in all DMPC, BSM, and SSM VACP spectra after a certain amount of CHL was added. Stacked plots of ^{13}C

MAS VACP spectra are shown in Figure V-8(a) for DMPC/CHL, Figure V-8(b) for BSM/CHL, and Figure V-8(c) for SSM/CHL, respectively. Detailed comparisons of the lipid membrane samples appear in Section C-2. Since there was no reference compound used, the comparison of ^{1}H chemical shift for the bulk methylene peaks used a common NMR transmitter frequency for experiments on all lipid/CHL samples and a reference chemical shift for pure DMPC from the published literature (Forbes and Oldfield, 1988) were conducted under the same conditions as pure lipid samples, the reference of chemical shift in each case can be considered identified.

B-5 SEVACP: order parameters for SM hydrocarbon chains in SM/CHL mixtures

As noted above, ^{2}H NMR methods have been used extensively to assess the acyl chain order in phospholipid multi-bilayer assemblies, but these studies require difficult and costly selective deuteration of the molecule of interest. Several new techniques have been developed in different NMR research groups to obtain order information directly from natural-abundance NMR nuclei. For instance, the Oldfield group reported a new 2D pulse sequence to determine inter-proton pair order parameters based on the linewidths of ^{1}H spectral patterns corresponding to chemical-shift identified feature in the high-resolution ^{13}C MAS NMR spectrum (Urbina and Oldfield, 1998). Here the inter-protons are defined as the protons at nearby carbons in the same molecule, differing from intra-protons that are the protons at the same carbon.

Fig. V-8(a): Stacked plot of ^{13}C MAS VACP spectra for DMPC/CHL mixtures at 34°C

Fig. V-8(b): Stacked plot of ^{13}C MAS VACP spectra for BSM/CHL mixtures at 67°C

Fig. V-8(c): Stacked plot of ^{13}C MAS VACP spectra for SSM/CHL mixtures at 67°C

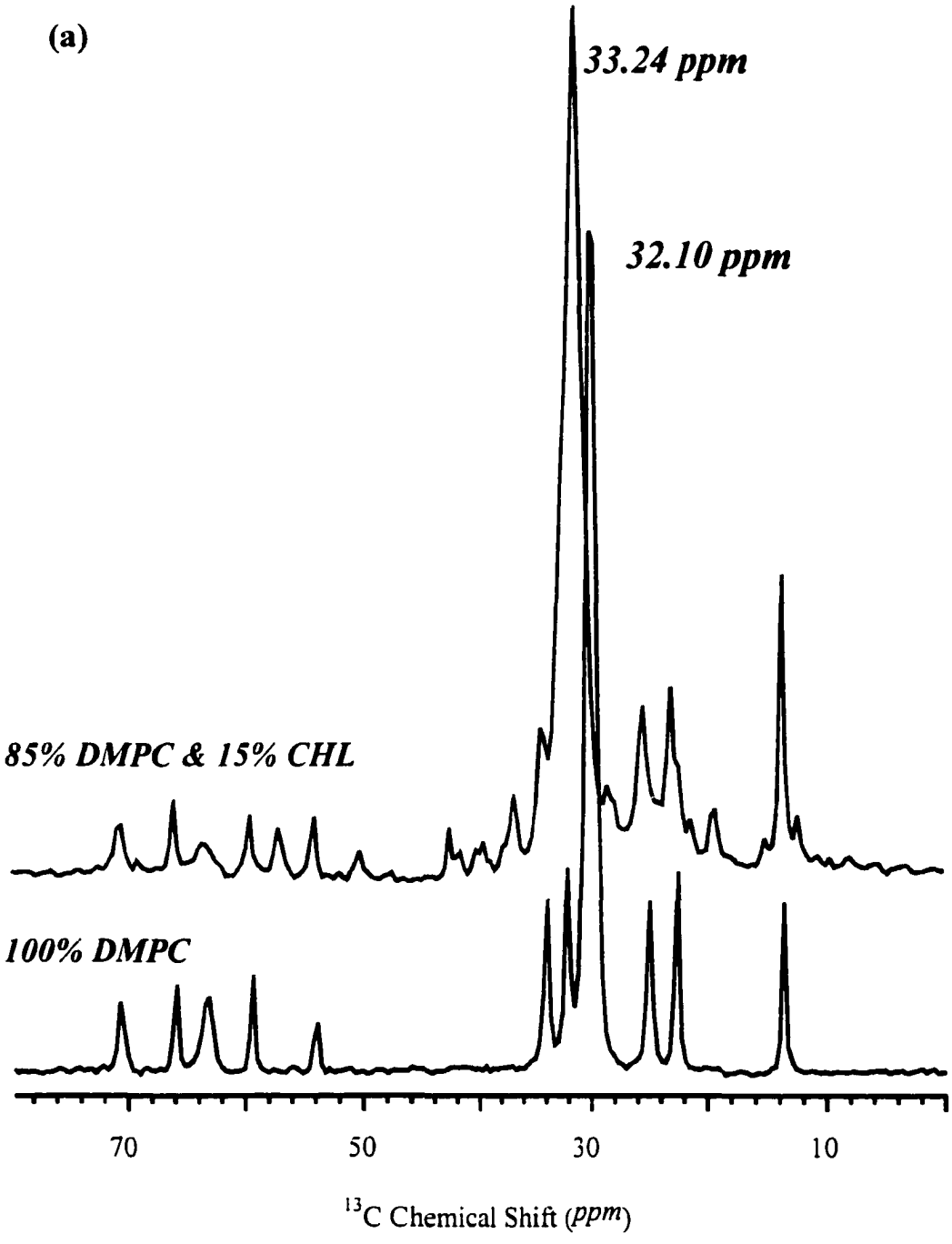

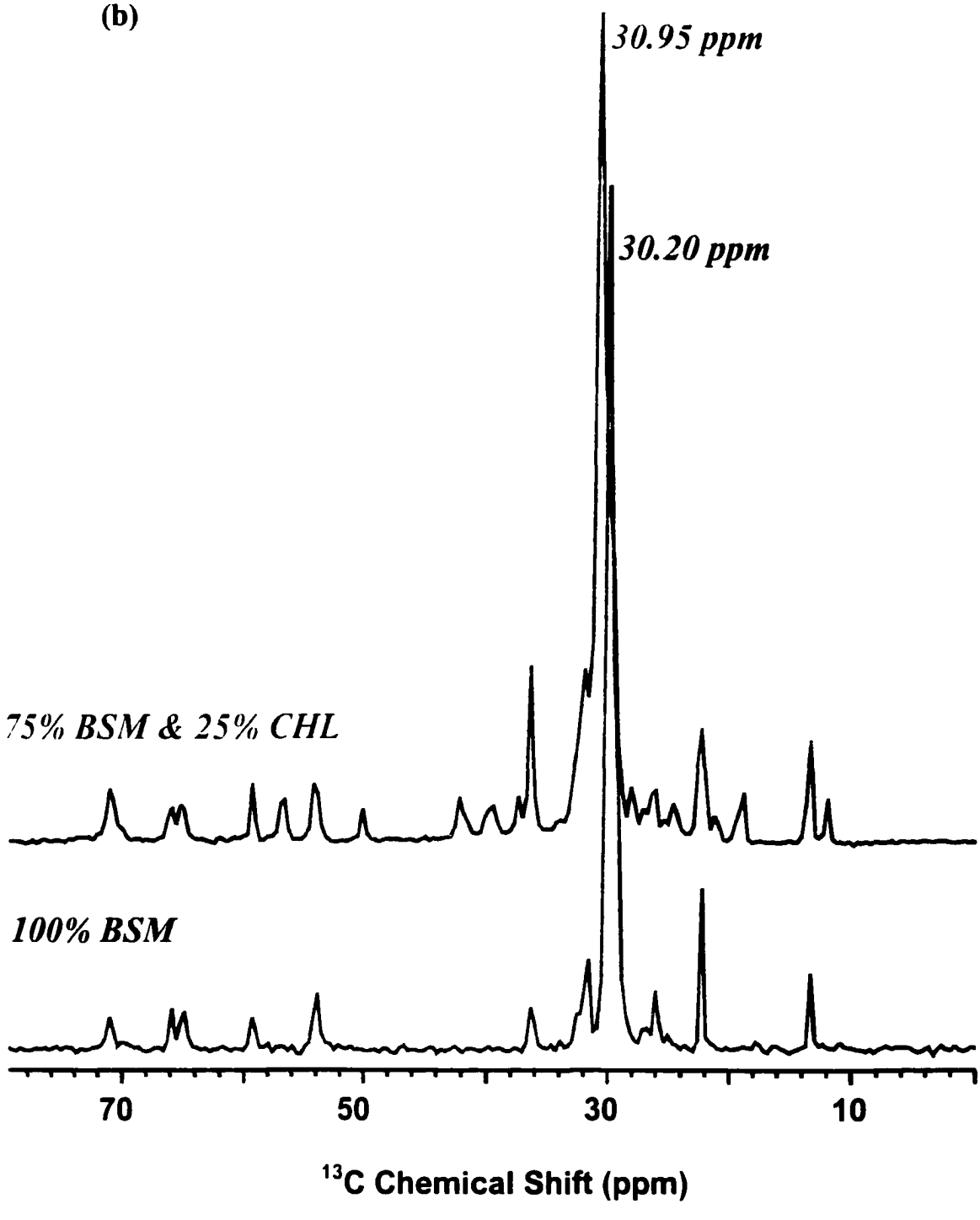

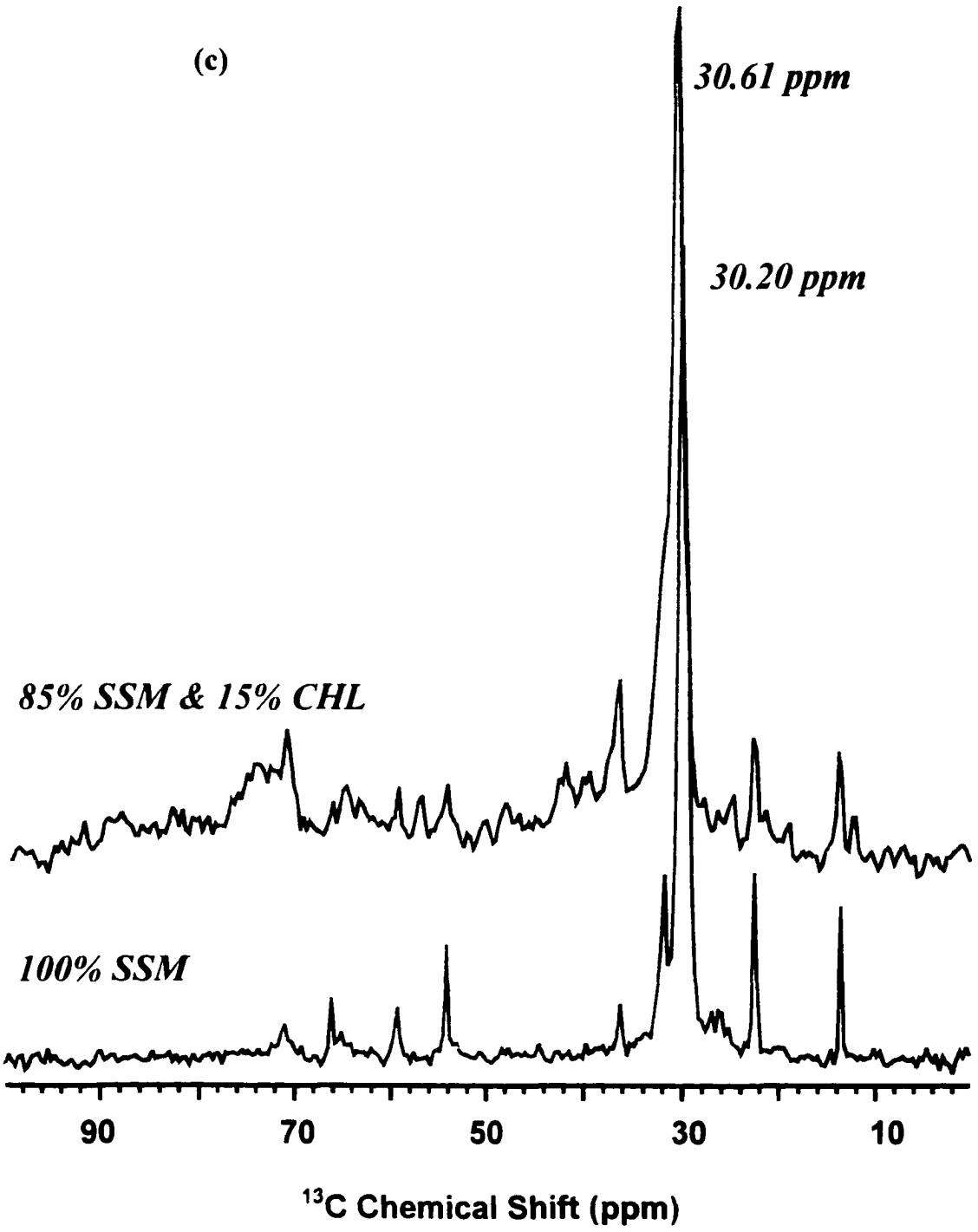

The pulse sequence was written by connecting the *Varian* solid echo and VACP sequences together, with phase cycling parameters supplied by Dr. Urbina. The pulse sequence is shown in Figure I-11 and the experiment is called SEVACP (Solid Echo & VACP). The 2D SEVACP experiments were performed for DMPC, BSM, SSM, and their mixtures with CHL, respectively. Typical 90° pulse lengths for P1 and P2 in the solid echo part were 5.5 μs; the CP contact time in VACP was 9000 μs. The time between the two 90° pulses ($t_1/2$) was 4 μs; 24 or 32 steps were used with 256 scans each. Due to the fact that Gaussian behavior of the decay breaks down at relatively long solid echo time, a wiggly line-shape was seen in ^1H wideline slices, as reported previously (Urbina and Oldfield, 1998). However, after using apodization to get rid of the problem of wiggly line-shape, the ^1H wideline traces displayed an excellent Gaussian line-shape. The SEVACP spectra are shown in Figure V-9(a) for 100% DMPC, Figure V-9(b) for 100% BSM, Figure V-9(c) for 100% SSM, and Figure V-9(d) for the 75% BSM/25% CHL mixture.

Fig. V-9(a): SEVACP spectrum of 100% DMPC at 34°C (T_r=0.03) and 4000 Hz

Fig. V-9(b): SEVACP spectrum of 100% BSM at 67°C (T_r=0.03) and 4000 Hz

Fig. V-9(c): SEVACP spectrum of 100% SSM at 67°C (T_r=0.03) and 4000 Hz

Fig. V-9(d): SEVACP spectrum of 75%BSM/25%CHL at 67°C (T_r=0.03) and 4000 Hz

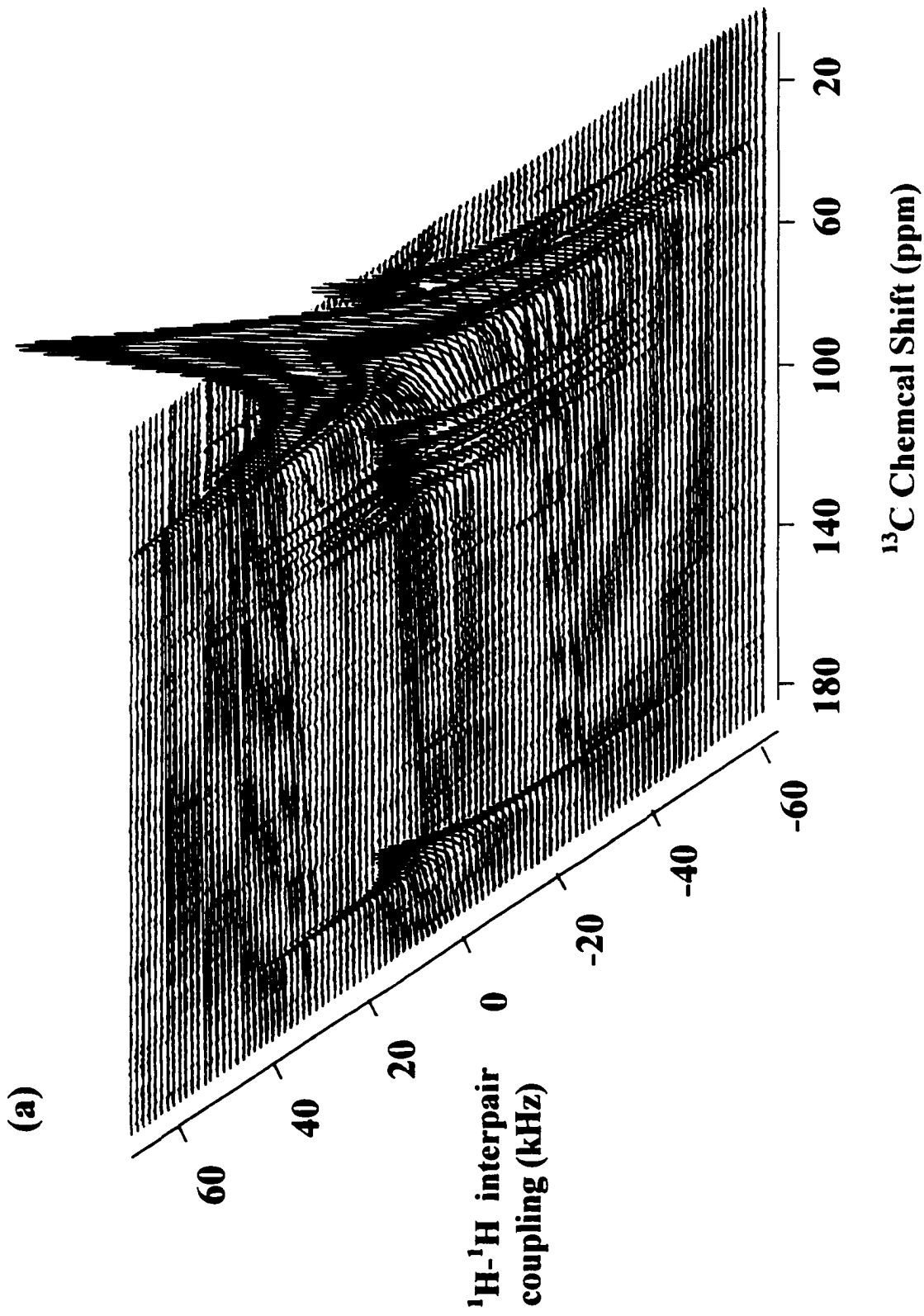

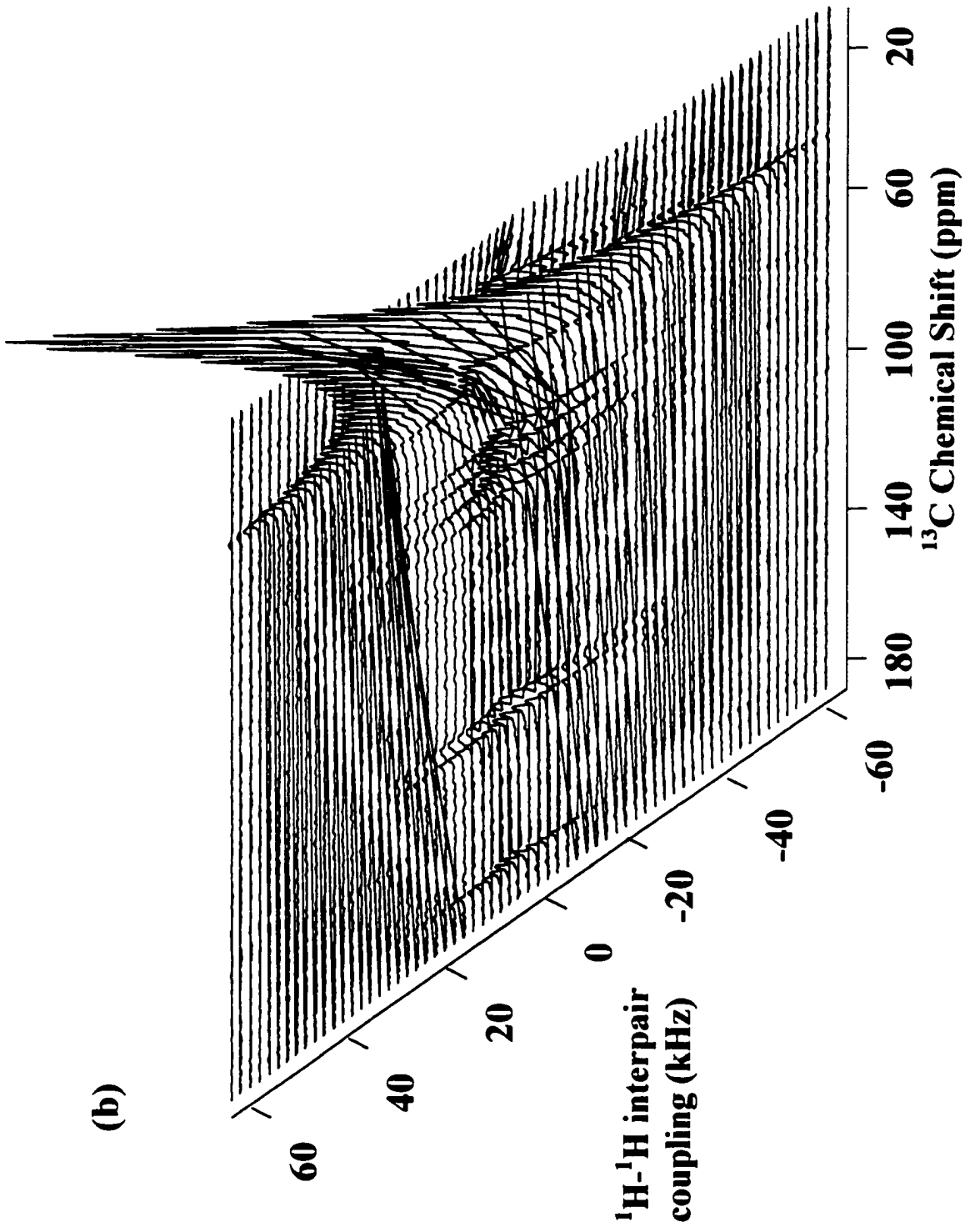

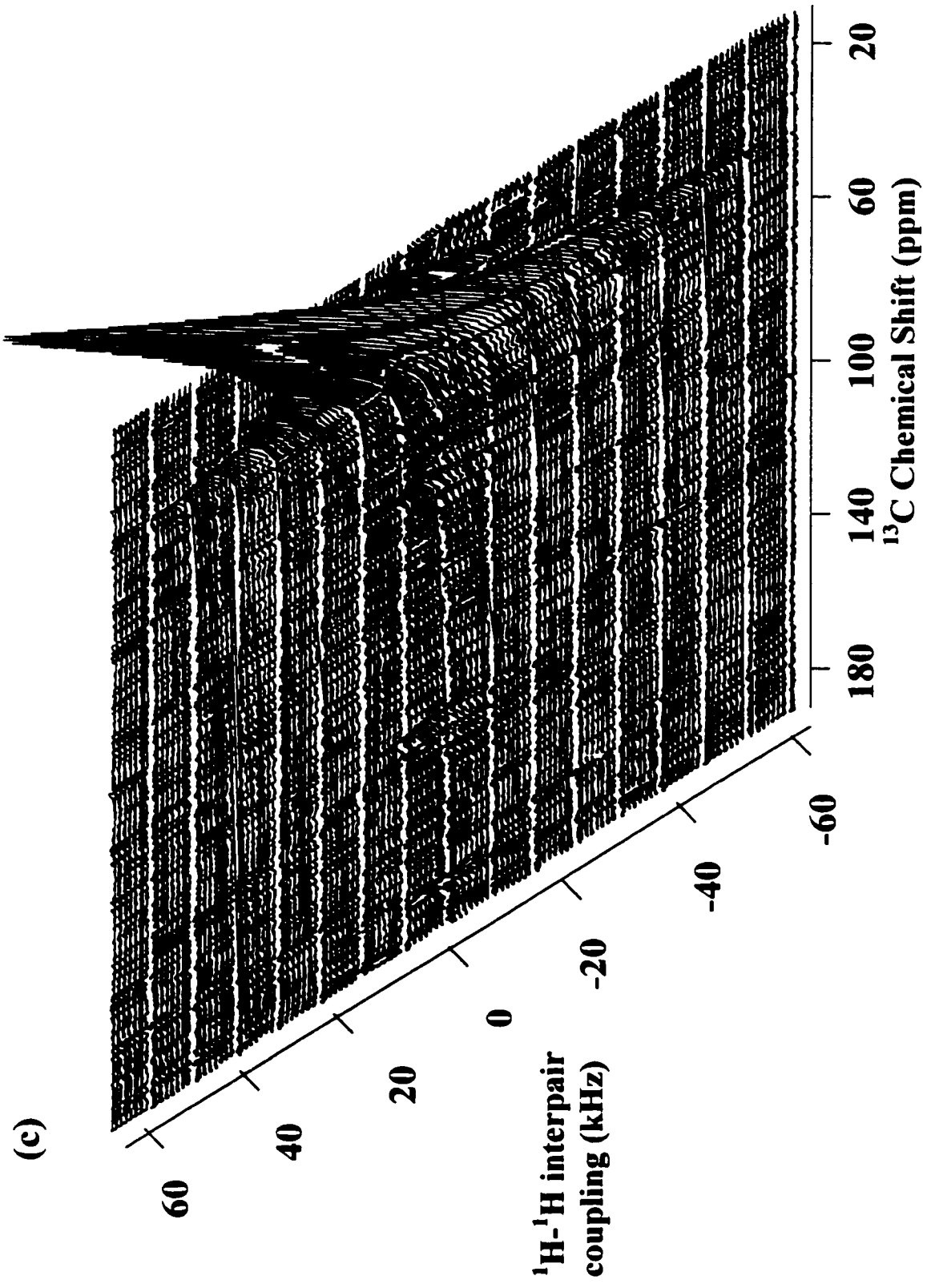

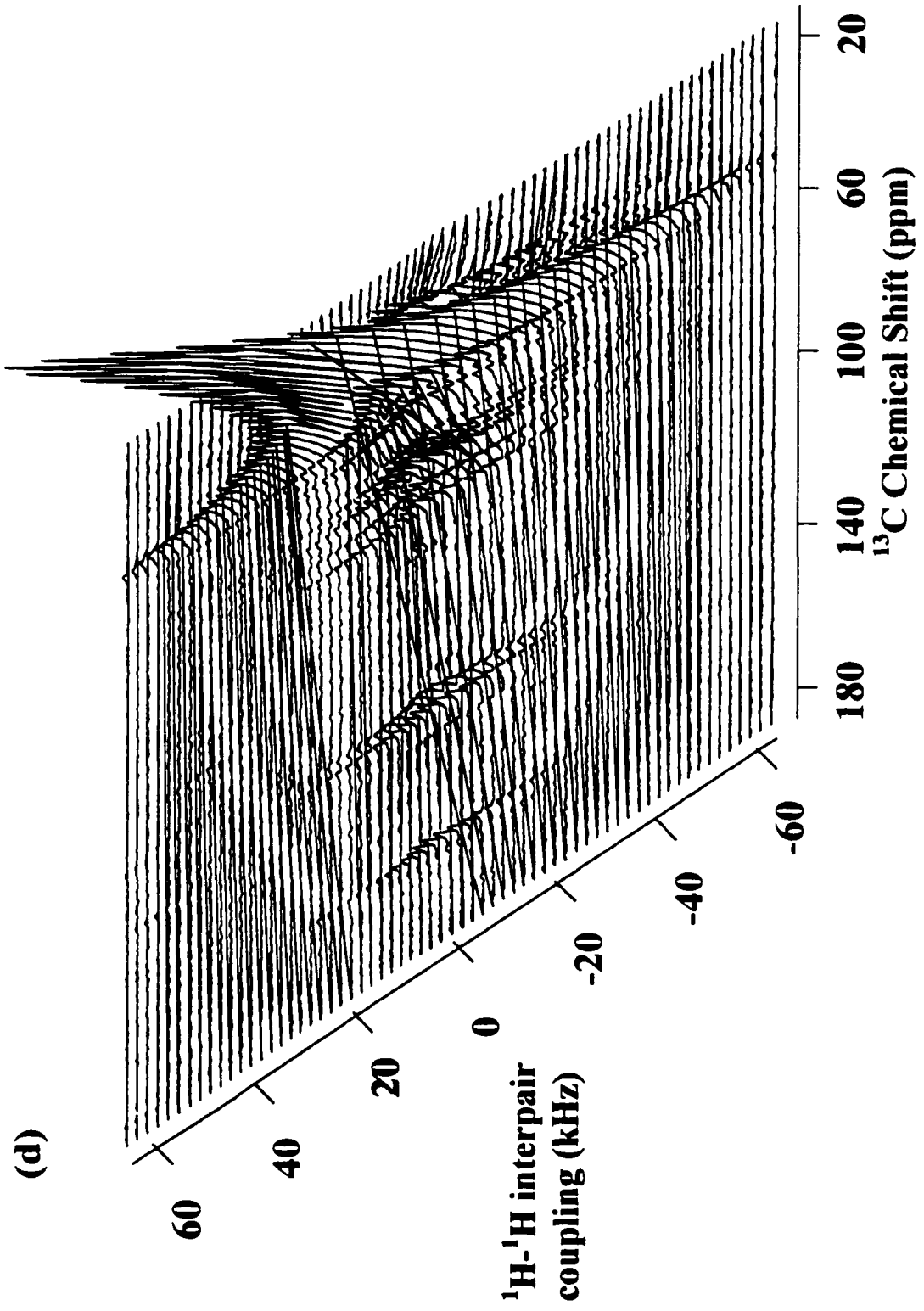

To extract the order parameters, the motionally averaged interpair second moments, $M_{2(inter,\ av)}$, are calculated from the ^{1}H linewidths at each ^{13}C chemical shift using Eq. V-2.

$$M_{2(inter,\ av)} = 2(\Delta\nu_{1/2})^2/\ln 2 \qquad \text{(Eq. V-2)}$$

where $\Delta\nu_{1/2}$ is the half-linewidth at half-height.

Further, the inter-pair order parameters $S_{ch(inter)}$ can be calculated from Eq. V-3 (Janes, 1990):

$$M_{2(inter,\ av)} = S^2_{ch(inter)} \times M_{2(inter)} \qquad \text{(Eq. V-3)}$$

where $M_{2(inter)}$ is the inter-pair second moment for a saturated, all-*trans* hydrocarbon chain and equals $5.5\times10^{9}\ s^{-2}$ (Bloom et al., 1978). The order parameters $S_{ch(inter)}$ of methylene chain segments obtained from SEVACP measurements and data analyses for all assigned carbons are shown in Fig. V-10(a) for DMPC and DMPC/CHL mixtures, Figure V-10(b) and (c) for BSM and BSM/CHL mixtures.

Fig. V=10(a): Inter-proton pair order parameters of DMPC methylene chain in DMPC/CHL mixtures as a function of segmental position at 34°C. The dashed line refers to methylene carbons with coincident chemical shifts.

Fig. V-10(b): Inter-proton pair order parameters of the saturated acyl chain in BSM/CHL mixtures as a function of segmental position at 67°C

Fig. V-10(c): Inter-proton pair order parameters of the unsaturated acyl chain in BSM/CHL mixtures as a function of segmental position at 67°C.

(a)

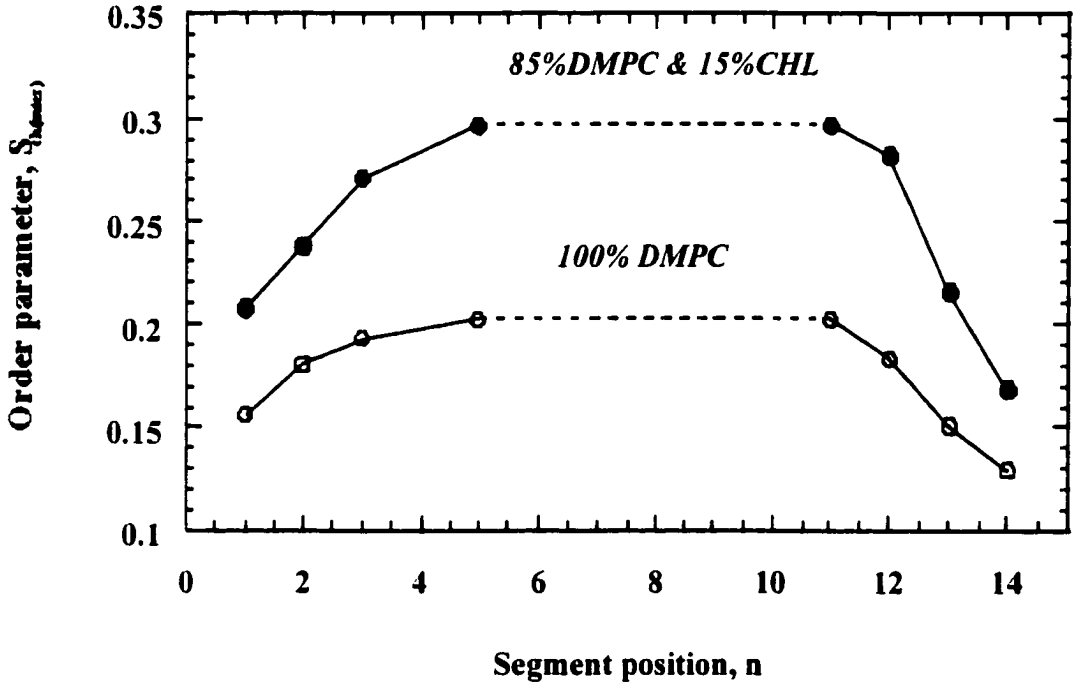

(b)

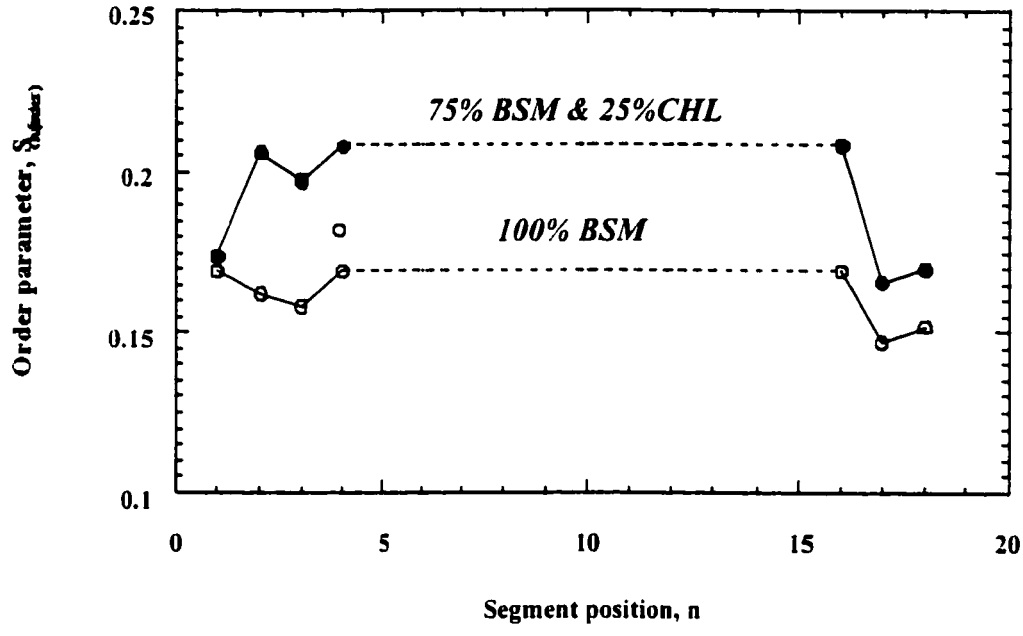

(c)

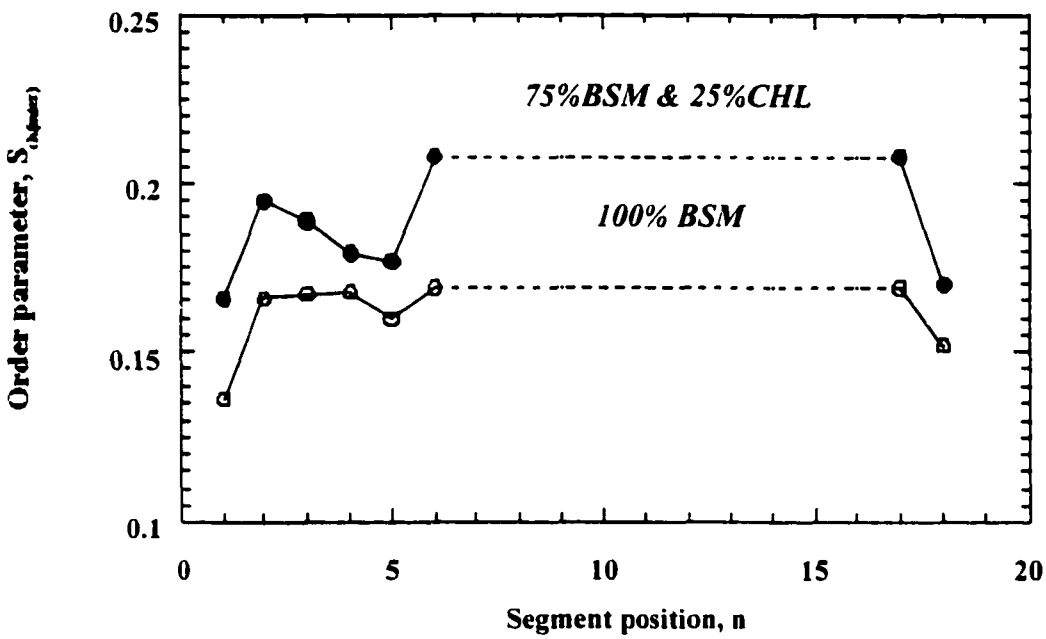

C Discussion

C-1 Comparison of order parameters for methylene chains of DMPC, BSM, and SSM

The curves of the % sideband intensity vs. spinning speed, shown in Figures 4-6, indicate that DMPC, BSM, and SSM membranes have the following ordering sequence: DMPC>BSM>SSM. After adding CHL, all DMPC, BSM, and SSM membranes become more ordered, as indicated by larger sideband intensities of phospholipid/CHL membranes than the corresponding phospholipid membranes. Furthermore, the effect of CHL is more significant in DMPC/CHL system than BSM/CHL system (Fig. V-7). The amount of peak intensity transferred from the central spectrum to the spinning sidebands is dependent on the angular restrictions of chain motion and probably on the rigidity of the chain, which reflects the order of membranes in a semiquantitative way.

The analyses of 2D SEVACP experiments supply more detailed order information because a quantitative description is available. Another important advantage is that the order property can be checked at each particular carbon position as long as its chemical shift is identified in the ^{13}C dimension. The curves of inter-proton pair parameters along methylene chains, shown in Fig. 10, confirm the sequence of ordering obtained from sideband intensities: DMPC>BSM>SSM. They also

demonstrate that the order of the DMPC membrane is more sensitive to CHL than the BSM membrane (Fig. V-7) (SSM data is not yet available).

Both ^{1}H MAS sideband intensity and SEVACP experiments illustrate that CHL increases chain order. The conclusion is consistent with prior studies (Huster et al., 1998) and can be explained by the attractive van der Waals interaction between lipid methylene chains and the steroid rings of CHL. However, the smaller sensitivity of BSM order to CHL addition is surprising in light of prior hypotheses regarding strong cholesterol-sphingomyelin interactions

The differences in order properties between BSM and SSM, which are evident in both sideband intensities and SEVACP results, may not provide a reliable indicator of their relative molecular order, because the phase transition temperature of SSM is not accurately known. Since synthetic C_{18} sphingomyelin (SSM) is a pure compound but commercial brain bovine sphingomyelin (BSM) is a mixture, pure SSM should show a somewhat higher phase transition temperature. Thus our measurements of spinning sideband intensity in SSM may have been done at lower T_r, where SSM should show greater order. In fact, Figures V-5 and V-6 reveal less acyl chain order in the SSM sample.

C-2 ^{13}C chemical shift and methylene chain conformation in membrane bilayers

The stacked plots of ^{13}C chemical shift spectra for DMPC/CHL (Fig. 8(a)), BSM/CHL (Fig. 8(b)), and SSM/CHL (Fig. 8(c)) show a consistent result: a down-field movement of ^{13}C signals of the bulk methylene peak induced by CHL. Because the *trans* conformation has less electronic shielding than the *gauche* conformation, it may be concluded that CHL causes a shift in conformation from the *gauche* state to the *trans* state along methylene chains in all three phospholipid membranes (Forbes and Oldfield, 1988). However, the extent of the chemical shift change is different. The CHL effect is much stronger for DMPC (15% of CHL causes 1.14 ppm down-field movement), but it is much weaker for BSM and SSM (25% CHL causes 0.74 ppm and 0.41 ppm down-field movement for BSM and SSM, respectively).

Since the *trans* conformation is much more ordered than the *gauche* conformation, the conformational trend should be also consistent with the increase in chain order described in Section C-1. In fact, the overall results obtained from three independent methods are in excellent agreement. Pure DMPC membranes are initially more ordered than pure BSM: it displays a higher % sideband intensity (Fig. V-7), and a greater order parameter (0.20 for DMPC and 0.17 for BSM), and it should have a greater propertion of *trans* conformations. Adding CHL positively affects the order of all three membranes; the greater sensitivity of DMPC than BSM is illustrated by greater increases in both sideband intensity % (Fig. V-7) and order parameter (Fig. V-10), as

well as a larger ^{13}C chemical shift change. (Experimental results are compared mainly between DMPC and BSM because of insufficient data for SSM and a possible deviation in phase transition temperature.)

C-3 Is there hydrogen-bonding in SM/CHL membranes?

A very interesting point can be seen the curves of chain order parameters for BSM/CHL mixtures (Figs. 10(b) and (c)). For both saturated and unsaturated chains, the order parameters increase at all carbon positions after CHL is added. However, carbons 1 and 2 of the saturated chain and carbons 3 and 4 of the unsaturated chain show irregular changes: carbon 1 of the saturated chain and carbons 3 and 4 of the unsaturated chain display abnormally small increases in order parameter; carbon 2 of the saturated chain also displays an unusually large jump. In order to understand the trend in detail, the molecular structure of BSM is shown in Figure V-11.

It is possible that intermolecular hydrogen bonding occurs between the carbonyl oxygen (carbon 1 of the saturated chain) and the double bond hydrogen (at carbon 4 of the unsaturated chain) in the pure BSM membrane. As the consequence of this hydrogen bond, the carbonyl carbon and the double bond segments have high order parameters in pure BSM preparations. Once CHL is added to the BSM membrane, the hydrogen bond system may be disrupted due to the approach of CHL. Here the CHL may mainly affect the carbonyl carbon because CHL is known to preferentially

approach saturated chains (Huster et al., 1998). After the hydrogen bonding system is disrupted, the carbonyl carbon becomes much more disordered and its order parameter is rendered lower than other nearby carbons.

The discussion for SSM is deferred because the signal/noise ratio in SEVACP of SSM/CHL mixtures was is too low to extract order parameter from ^{1}H spectral slices.

Fig. V-11: Molecular structure of bovine brain sphingiomyelin (BSM)

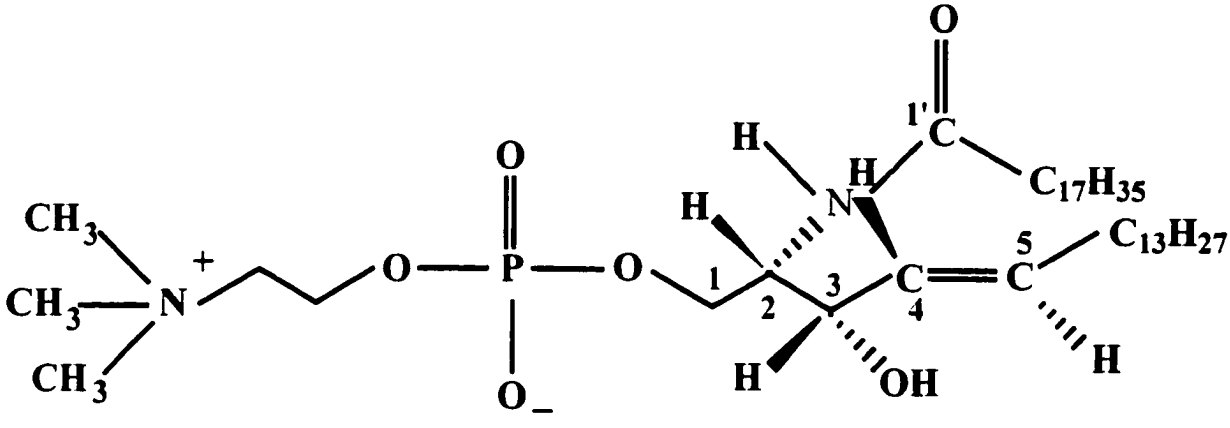

Chapter VI Conclusions

A Combining NMR and QLS methodologies to deduce organizational models for mixed aggregates

It is often a challenging task to deduce the detailed molecular arrangement and organization in mixed micellar mixtures. As described in the following related sections, however, these properties are very important because many problems in biology, nutrition, medicine, and colloid chemistry are associated with multi-component aggregation.

Our work on fat digestive model mixtures demonstrates the effectiveness of the combined NMR and QLS protocol in studying mixed lipid aggregates. High-resolution 2D NMR experiments (DQF-COSY, TOCSY, and HMQC) are sufficient for the assignment of all ^{1}H NMR peaks. Furthermore, the assignments make it possible to analyze NOESY cross peaks and to deduce the molecular orientation by ^{1}H linewidth broadening during Mn^{2+} titration. Since the NOE signal depends on tumbling time and thus aggregate size, it is common that some important NOE cross peaks may be absent from the NOESY spectrum, so that ROESY experiments have been conducted to make sure no valuable NOE peaks are lost. Also, a comparison between TOCSY and NOESY spectra helps to distinguish intermolecular and intramolecular NOE cross peaks. As shown in the fat transport study, the NMR spectral resolution is significantly diminished

as the size of mixed aggregates increases. When this happens, NMR experiments with magic-angle spinning must be used to overcome the problem.

The ability to deduce the shape of mixed aggregates by QLS depends on the feasibility of preparing QLS samples with a narrow monodisperse size distribution, because there are no data treatment methods available to handle wide or two-size distributions with sufficient accuracy for shape analyses.

B Significance of the rodlike fat digestive aggregates for late-stage fat digestion

It is widely accepted that fat hydrolysis occurs at the interface of mixed fat digestive aggregates, through the catalytic activity of water-soluble enzymes. The formation of small size aggregates will lead to a large interfacial area and greatly favor enzymatic attack. Our QLS measurements indicate that small aggregates (R_h: ~3-4 nm) are dominant in number in late-stage fat digestive model mixtures, so that fat digestion in this period is expected to be highly efficient.

Bile salts (TC) play a decisive role in mixed fat digestive aggregation, as well as in late-stage fat digestion. TC dimers (or tetramers) may be considered to form the skeleton of the rodlike aggregates, with fatty acids (FA) and monoglycerides (MG) filling in the gaps between TCs. Within the context of our model, small fluctuations in the amount of TC can be accommodated by varying size of rodlike aggregates.

However, larger changes in TC concentration will disrupt these rodlike aggregates. This is why an abnormal secretion of TC in the body can cause serious problems in food digestion and absorption.

C Low ratio DMPC/DHPC bicelles offer an isotropic membrane-mimetic medium for NMR studies

High ratio (q>2.5) DMPC/DHPC bicelles have been used successfully as media for protein NMR studies (Tjandra and Bax, 1997). However, these anisotropic liquid crystalline bicelles are not suitable for high-resolution NMR studies of membrane-associated macromolecules, because at higher concentration the slow overall motion of the bicelles prevents acquisition of high-resolution NMR spectra (Vold et al., 1997). Although low ratio (q=0.5) bicelles tumble isotropically and yield high-resolution NMR spectra of small peptides (Vold et al., 1997), the question of whether these bicelles maintain a discoid shape (Sanders and Schwonek, 1992; Vold et al., 1996) and bilayer arrangement had been unclear. The QLS work described in Chapter IV is the first successful independent determination supporting the hypothesis that low ratio bicelles maintain the bilayered discoid arrangement.

Such low ratio (q=0.5) bicelles may have significant potential in NMR studies of membrane-associated proteins, peptides, and nucleic acids. For example, Girvin reported the application of bicelles (q=0.5) in his NMR study of subunit c of the ATP

synthase catalytic complex (Girvin, 2000). It can be expected that more applications of low-q bicelles will be seen in future NMR studies, since many important biomolecules function uniquely in membrane environments.

D. Molecular order and hydrogen bonding in sphingomyelin/cholesterol multibilayers

Recently, new 2D NMR techniques have been developed as alternatives to the ^{2}H NMR method of studying the order parameter of lipid membranes. In this work, the relatively simple SEVACP experiment (Urbina and Oldfield, 1998) was applied to DMPC/CHL and SM/CHL mixtures. Since the solid echo yielded accurate wideline shapes in one dimension and these widelines were further separated by high-resolution ^{13}C chemical shifts in the second dimension, the order $S_{ch,inter}$ of the acyl chains of phospholipids could be calculated from the linewidth as long as their chemical shifts were identified. In addition to the 2D SEVACP experiment, two other standard NMR methods were used for extracting qualitative molecular order information: ^{1}H MAS sideband intensities as a function of spinning speed and ^{13}C chemical shift movement as a function of sample proportions. Because the same reduced temperature (T_r) was used, the results obtained from different phospholipids could be compared.

Although each method has a different basis, the overall results are very consistent. First, $S_{ch,inter}(DMPC) > S_{ch,inter}(BSM) > S_{ch,inter}(SSM)$; secondly, the addition

of CHL causes all membranes to become more rigid and ordered with a greater fraction of *trans* conformation; and thirdly, the sensitivity of CHL to each membrane follows the order: DMPC > BSM > SSM. The differences between BSM and SSM are surprising, but they may be attributed to the possibility that SSM experiments were run further from the (unknown) phase transition temperature.

The quantitative determinations of order parameters for acyl chains lead to another interesting conclusion. After addition of CHL, the DMPC membrane shows an almost uniform increase of order parameter at each acyl carbon; but the BSM membrane (Fig. V-10 (a)) displays some abnormal changes at certain carbons (Fig. V-10 (b) & (c)). In 100% BSM, the C1 (carbonyl carbon) of the saturated acyl chain and the C3 (with hydroxyl) and C4 (double bond) of the unsaturated acyl chain show high order parameters, but, they evidently decrease after CHL is added. The loss of high order parameters at these sites upon the addition of CHL suggest that hydrogen bonding interactions, which occurred between two acyl chains in pure BSM, have been disrupted. Between the two acyl chains of BSM, the increase of order parameters is more sensitive in the saturated acyl chain compared with the unsaturated acyl chain. This trend fits the conclusion that CHL favors an approach to the saturated chain rather than unsaturated chain.

Appendix A

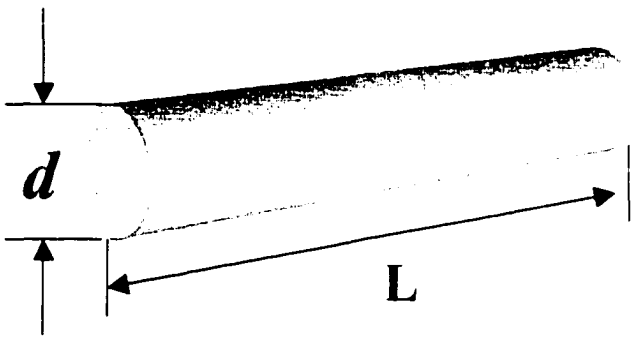

Cylinder-like rod model

L: Length of rod
d: Diameter of rod

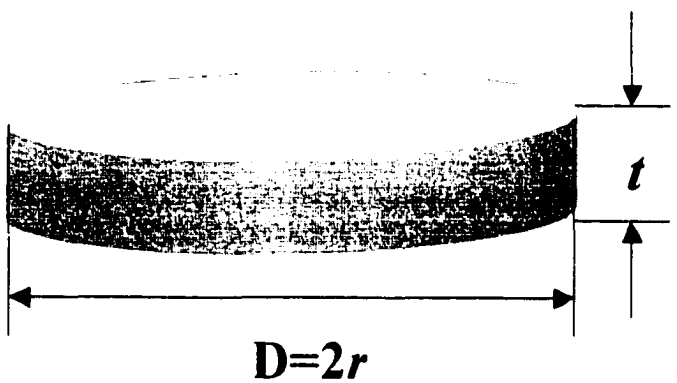

Disk model

r: Radius of disk plane
t: Thickness of disk

Equations for calculation of length of rod and radius od disk from hydrodynamic radius R_h of sphere (Mazer et al., 1980):

Rod: $$R_h = \frac{3}{4}d\{[1+(\frac{L}{d})^2]^{1/2} + \frac{d}{L}\ln[\frac{L}{d}+[1+(\frac{L}{d})^2]^{1/2}] - \frac{L}{d}\}^{-1}$$

Disk: $$R_h = \frac{3}{2}r\{[1+(\frac{t}{2r})^2]^{1/2} + \frac{2r}{t}\ln[\frac{t}{2r}+[1+(\frac{t}{2r})^2]^{1/2}] - \frac{t}{2r}\}^{-1}$$

Reference List

Aue, W.P., Bartholdi, E., & Ernst, R.R. (1976) *Journal of Chemical Physics 64*, 2229.

Barnes S.Geckle J.M. (1982) *J.Lipid Res. 23*, 161.

Bax A.et al.(a) (1985) *Journal of Magnetic Resonance 63*, 207.

Bax A.et al.(b) (1985) *Journal of Magnetic Resonance 65*, 355.

Bax A.et al. (1988) *Journal of Magentic Resonance 77*, 134.

Benn R. & Gunther H. (1983) *Angew.Chem.Int.Ed.Engl. 22*, 350.

Bian J. & Roberts M.F. (1990) *Biochemistry 29*, 7928.

Bloom M., Burnell E.E, & Mackay A.L. (1978) *Biochemistry 17*, 5750.

Blumich B. & Spiess H.W. (1988) *Angew.Chem.Int.Ed.Engl. 27*, 1655.

Braun, S., Kalinowski, H.O., & Ber, S. (1994) in *100 and More Basic NMR Experiments*, VCH, New York.

Brown J.C., Pussy P.N., & Dietz R. (1975) *Journal of Chemical Physics 62*, 1136.

Bruzik K.S.. Sobon B., & Salamonczyk G.M. (1990) *Biochemistry 29*, 4017.

Cantor C.R. & Schimmel P.R. (1980) in *Biophysical Chemistry II Techniques for the Study of Biological Structure and Function* (AnonymousW. H. Freeman, San Francisco.

Carey M.C., Small, D.M., & Bliss, C.M. (1983) *Ann.Rev.Physiol. 45*, 651.

Carey M.C. (1985) in *Sterols and Bile Acids* (Danielsson H. & Sjovall J., Eds.) pp 345-403, Elsever Science Publishers B. V., New York.

Chen Zhenjia. Solution, Semisolid, and Solid NMR Studies of Lipid Model Membranes. 1996. (GENERIC)
Ref Type: Thesis/Dissertation

Chu Benjamin (1991) in *Laser Light Scattering Basic Principles and Practice*, Academic Press, Inc., New York.

Cohen D.E., Fisch M.R., & Carey M.C. (1990) *Hepatology 31*, 113S.

Croasmun W.R. & Carlson R.M.K. (1994) in *Two-Dimensional NMR Spectroscopy Application for Chemists and Biochemists*, VCH, New York.

Davis J.H. & Thompson M.B. (1993) *J.Lipid Res. 34*, 651.

Debye P. & Anacker E.W. (1959) *Journal of Phys.Colloid Chem. 55*, 644.

Ernst, R.R. (1992) *Angew.Chem.Int.Ed.Engl. 31*, 805.

Eum K.M., Riedy G., Langley K.H., & Roberts M.F. (1989) *Biochemistry 28*, 8206.

Forbes J. & Oldfield E. (1988) *Journal of Chem.Soc., Faraday Trans.1, 84*, 3821.

Fyfe, C.A. (1983) in *Solid State NMR for Chemists*, C. F. C. Press, Ontario.

Gabriel N.E. & Roberts M.F. (1984) *Biochemistry 23*, 4011.

Gabriel N.E. & Roberts M.F. (1987) *Biochemistry 26*, 2432.

Girvin et al. (2000) in *NMR and Structural Biology: Preparing for the new millennium*, (UnPub)

Gunther H. (1995) in *NMR Spectroscopy Basic Principles, Concepts, and Applications in Chemistry*, John Wiley & Sons, New York.

Guo W. & Hamilton J.A. (1995) *Biochemistry 34*, 14174.

Halvorsen R.A., Ribeiro Jr., Blinder R., Water C., & Thompson W.M. (1989) *Invest.Radiology 24*, 903.

Hamosh M. (1990) in *Lingual and Gastric Lipases: Their Role in Fat Digestion*, CRC Press, Boca Raton.

Hiemenz P.C. & Rajagopalan R. (1997) in *Principles of Colloid and Surface Chemistry* (AnonymousMarcel Dekker, Inc., New York.

Homans S.W. (1999) in *A Dictionary of Concepts in NMR*, Oxford University Press, New York.

Huster D., Arnold K., & Gawrisch K. (1998) *Biochemistry 37*, 17299.

Hwang T.L. & Shaka A.J. (1992) *Journal of American Chem.Soc. 114*, 3157.

Janes N.Rubin , E.T.T.F. (1990) *Biochemistry 29*, 8385.

Kessler H., Griesinger C., Kerssebaum P., Wagner K., & Ernst R.R. (1987) *J.Am.Chem.Soc. 109*, 607.

King T.A. & Treadaway M.F. (1977) *Journal of Chemical Physics 73*, 1616.

Koenig B.W., Strey H.H., & Gawrisch K. (1997) *Biophysical Journal 73*, 1954.

Koppel D.E. (1972) *Journal of Chemical Physics 57*, 4814.

Li K.L., Tihal C.A., Guo M.M., & Stark R.E. (1993) *Biochemistry 32*, 9926.

Longo P.A. NMR Studies of Peptide Protein and Mixed Lipid Systems. 1992. (GENERIC)
Ref Type: Thesis/Dissertation

Mansfield, P. (1964) *Physical Review 137*, A961.

Mazer N.A., Benedek G.B., & Carey M.C. (1976) *Journal of Chemical Physics*

Mazer N.A., Carey M.C., Kwasnick R.K., & Benek G.B. (1979) *Biochemistry 18*, 3064.

Mazer N.A., Benedek G.B., & Carey M.C. (1980) *Biochemistry 19*, 601.

Mazer N.A. (1988) in *Dynamic Light Scattering* (Pecora Robert, Ed.) pp 305-346, Plenum Press,

McDonnell P.A. & Opella S.J. (1993) *Journal of Magnetic Resonance, Series B 102*, 120.

Metz G., Wu X., & Smoth S.O. (1994) *Journal of Magnetic Resonance, Series A 110*, 219.

Neue G. & Dybowski C. (1997) *Solid State Nuclear Magnetic Resonance 7*, 333.

Neuhaus D. & Williamson M.P. (1989) in *The Nuclear Overhauser Effect in Structural and Conformational Analysis*, VCH, New York.

Peersen O.B. & Smith S.O. (1993) *Journal of Magnetic Resonance, Series A 104*, 334.

Phillies G.D.J. (1990) *Analytic Chemistry 62*, 1049A.

Provencher, S.W. (1979) *Makromol.Chem. 180*, 201.

Sanders C.R. & Schwonek J.P. (1992) *Biochemistry 31*, 8898.

Sanders J.K.M. & Hunter B.K. (1993) in *Modern NMR Spectroscopy A Guide for Chemists*, Oxford University Press, New York.

Sarnes S. & Geckle J.M. (1982) *J.Lipid Res. 23*, 161.

Schmidt-Rohr K. & Spiess H.W. (1994) in *Multidimensional Solid-State NMR and Polymers*, Academic Press, San Diego.

Schmitz K.S. (1992) in *An Introduction to Dynamic Light Scattering by Macromolecules*, Academic Press, Boston.

Separovic F. & Gawrisch K. (1996) *Biophysical Journal 71*, 274.

Small D.M. (1986) in *The Physical Chemistry of Lipids: from Alkenes to Phospholipids*, Plenum Press, New York.

Smith, R.I. & Oldfield E. (1984) *Science 225*, 280.

Staggers J.E., Hernell O., Stafford R.J., & Carey M.C. (1990) *Biochemistry 29*, 2028.

Tjandra N. & Bax A. (1997) *Science 278*, 1111.

Urbina J.A. & Oldfield E. (1998) *Biophysical Journal 75*, 1372.

Vold R.R & Prosser R.S. (1996) *Journal of Magnetic Resonance, Series B 113*, 267.

Vold R.R, Prosser R.S., & Deese A.J. (1997) *Journal of Biomolecular NMR 9*, 329.

Wang D.et al.(a) (1992) *Journal of Physical Chemistry 96*, 8187.

Wang D.et al.(b) (1992) *J.Lipid Res. 32*, 431.

Westerman P.W. (1995) *J.Lipid Res. 36*, 2437.

Wuthrich K. (1997) *Proc.Natl.Acad.Sci.USA 94*, 12366.

Yeagle P.L., Hutton W.C., & Martin R.B. (1978) *Biochemistry 17*, 5745.

Yeagle P.L. (1993) in *The Membranes of Cell*, Academic Press, Inc., San Diego.

Young C.Y., Missel P.J., Mazer N.A., Benedek G.B., & Carey M.C. (1978) *Journal of Physical Chemistry 83*, 1375.

Zemb Th., Dubois M., & Gulik-Krzywicki Th. (1999) *Science 283*, 816.